

## ABSTRACT

Title of Dissertation: DEVELOPMENT OF AN INTEGRATED  
CAPSULE SYSTEM FOR  
GASTROINTESTINAL-TARGETED  
BIOSENSING

George Banis, Doctor of Philosophy, 2019

Dissertation Directed By: Professor Reza Ghodssi, Department of  
Electrical and Computer Engineering, Institute  
for Systems Research

Non-invasive microsystems are emerging as a means to address diagnostics challenges in healthcare due to the potential to retrieve information at the source and in a personalized approach. The gastrointestinal (GI) tract is a hub of information that alters in composition during both homeostatic and pathological conditions, and often manifests as varying biochemical concentrations in cell and tissue-sourced secretions. Thus, innovative strategies to sample molecular information from these secretions would be of significant benefit to physicians in establishing an appropriate prognosis. This dissertation describes the development of a film-based capacitive sensing strategy and subsequent integration into a capsule-based microsystem that is designed to travel through the GI tract upon ingestion until it passes through the stomach, where it is designed to measure model analytes in duodenal secretions. Subsequently, the measurements are processed into signals for wireless transmission, enabling external analysis for potential clinical utility.

To achieve a system that can be safely ingested by patients, design features must be implemented that follow previously established standards in device requirements such as geometry and biocompatibility. In this work, I aided in the design, integration, and characterization of a capsule-embedded sensing system using commercial off-the-shelf components that interface capacitive transducers (range: 0.8-220 pF; sensitivity:  $7.3 \times 10^{-3}$ ) with a smart phone via Bluetooth Low Energy (2.4 GHz). The transducers are designed to measure the change in dielectric constant of interfacing media, which transitions when specific environmental (pH) characteristics are met. The system, including the power supply, are manufactured on a printed circuit board and packaged within a 3D-printed capsule structure (13 mm x 35 mm) that maintains dimensions of other clinically utilized ingestible capsule devices. The system is cost effective, user-friendly, biocompatible, and can serve as a highly customizable platform for measuring a variety of desired targets.

Secretions from various GI organs can be distinguished by pH, as is demonstrated in the pharmaceutical industry via enteric coatings that dissolve in target pH ranges but maintain structural stability in others. I employed such coatings for protecting our system until targeting the pH, and therefore GI region, of interest for sampling. Once dissolved, microfluidic inlets allow access for the media to interface with the sensors. I studied coatings that respond to both acidic (<pH 3) and neutral conditions (>pH 6), as well as pH sequences via hierarchical coatings. Because the target analytes react with naturally occurring substrates, I investigated label-free sensing of model enzymes such as pancreatic trypsin (20-40  $\mu\text{M}$ ) and lipase (10  $\mu\text{M}$ -1 mM), as well as bile salts (0.07-7 % w/v) as a model emulsifier, using films composed

of biomaterials, including gelatin and stearin. To integrate these materials with the desired microsystem, I investigated various film deposition and modification strategies. Studies performed with our platform suggest the potential for the ability to sample the target fluid, as well as sense the analyte of interest in different concentrations by comparing the rate of capacitance change upon fluid entry compared to uncoated controls. Using this system, I characterized its potential for utility as a non-invasive platform for targeting multiple GI regions and detecting sensor-compatible biomarkers.

DEVELOPMENT OF AN INTEGRATED CAPSULE SYSTEM FOR  
GASTROINTESTINAL-TARGETED BIOSENSING

by

George Efstratios Banis

Dissertation submitted to the Faculty of the Graduate School of the  
University of Maryland, College Park, in partial fulfillment  
of the requirements for the degree of  
Doctor of Philosophy  
2019

Advisory Committee:

Professor Reza Ghodssi, Chair/Advisor  
Professor William Bentley  
Professor Ian White  
Professor Katharina Maisel  
Professor Peter Kofinas

© Copyright by  
George Efstratios Banis  
2019

## Dedication

To *my parents*,

whose boundless support enabled my success,

to *Christina Angela*,

my love and best friend,

and

to *Maraki, Ted, and Panagiotis Theodoros Adamos*.

## Acknowledgements

First and foremost, I would like to thank my advisor Professor Reza Ghodssi for his guidance and support during the course of this work. I would also like to thank the members of the Ph.D. dissertation committee, Professor William Bentley, Professor Ian White, Professor Katharina Maisel, and Professor Peter Kofinas, for their helpful discussions leading to the completion of this work.

There are several individuals with whom this work would not have been possible. I acknowledge Dr. Luke Beardslee for his engineering, scientific, and medical expertise and skills that both challenged me and led to the development of various technologies critical to this work. I am also grateful to other members of MEMS Sensors and Actuators Laboratory (MSAL), most notably Justin Stine and Rajendra Mayavan Sathyam, whose expertise significantly aided the progression of the system electronics. The success of this project developed further through extensive feedback and support from additional members of MSAL, including Dr. Sangwook Chu, Ryan Huiszoon, Ashley Chapin, Dr. Pradeep Rajasekaran, and Dr. Sanwei Liu.

My experience in MSAL was initially shaped by my excellent mentors and members of the MiND project, Professor Hadar Ben-Yoav, Sheryl Chocron, and Dr. Thomas Winkler, who introduced me to the lab culture and set the standards for how to enhance my research and writing skills. My gratitude extends further to other members of the MiND project, specifically Dr. Gregory Payne, Dr. Eunyoung Kim, Dr. Mijeong Kang, Dr. Deanna Kelly, Christopher Kitchen, and Stephanie Feldman. I also want to thank MSAL alumni Dr. Hyun Jung, Dr. Sowmya Subramanian, Dr. Faheng Zhang, and Dr. Konstantinos Gerasopoulos for their support, technical

feedback, and overall useful discussions. I would also like to give mention to the undergraduate students involved with my projects in MSAL, including Patricia Barton, Florence Stevenson, Sonia Arya, Tony Feric, Charles Perera, Aditya Nilacantan, and Prateek Sayyaparaju.

I would like to acknowledge the support and training I received in aspects of device fabrication, specifically staff members of the Maryland NanoCenter including those in the FabLab (Mr. John Abrahams, Mr. Thomas Loughran, Mr. Jonathan Hummel, and Mr. Mark Lecates), AIMLab (Dr. Wen-An Chiou, Dr. Sz-Chian Liou), and Terrapin Works. Moreover, I am grateful to the administrative staff in ISR and BioE, especially Vicci Barret, Regina King, Carla Scarbor, Dawn Wheeler, Dr. Tracy Chung, and Bill Churma, for their responsiveness and willingness to put up with my administrative concerns and request. Additionally, this work was only achieved through the funding from the National Science Foundation (NSF) under program manager Shubra Gangopadhyay.

Finally, I would like to thank my family and friends. My parents sacrificed more than they needed to for me to succeed, and are my primary source of unyielding encouragement and support along with my sister Maria and her husband Ted. I have been very fortunate to have the support of some of my closest friends here in the BIOE department, namely Leopoldo Torres, Imaly Nanayakkara, Anjana Jeyaram, and Kelsey Gray, without whom fun and emotional support would have been significantly more difficult to achieve. Lastly, I want to thank my partner Christina, for her constant love and being my foundation for what matters most to me in life.

# Table of Contents

Dedication.....	ii
Acknowledgements.....	iii
Table of Contents.....	v
List of Tables.....	viii
List of Figures.....	ix
List of Abbreviations.....	xiv
1. Chapter 1: Introduction.....	1
1.1 Background and Motivation.....	1
1.2 Summary of Accomplishments.....	3
1.2.1 Investigation of Biomaterial Film-Based Electrical Transduction Systems for Measuring Enzymatic Activity.....	4
1.2.2 Investigation of Embedded Packaging Materials for Gastrointestinal Targeting.....	5
1.2.3 Development of Ingestible Integrated System for Targeted Gastrointestinal Sampling and Enzyme Sensing.....	6
1.3 Literature Review.....	7
1.3.1 Electrical Biosensors.....	7
1.3.2 Exocrine Pancreatic Health and Diagnostics.....	13
1.3.3 Pancreatic Enzyme Activity and Other Gastrointestinal Fluid Contents...	17
1.3.4 Integrated <i>In situ</i> Capsule Technology.....	22
1.4 Structure of Dissertation.....	28
2. Chapter 2: Electrical Transduction of Pancreatic Trypsin Activity.....	29
2.1 Pancreatic Enzyme Sensing.....	29
2.2 System Design and Experimental Setup.....	33
2.2.1 IDE Sensor Fabrication and Film Deposition.....	33
2.2.2 Enzyme Solution Preparation.....	35
2.2.3 Impedance Sensing.....	35
2.2.4 QCM Sensing Methodology.....	37
2.2.5 Image/Data Analysis.....	37
2.3 Results and Discussion.....	38
2.3.1 Film Structure and Morphology.....	38
2.3.2 Impedance Sensing of Trypsin.....	41
2.3.3 Impedance Response with Enzyme Mixture.....	44
2.3.4 QCM Results.....	48
2.4 Film Reactions to Varying Enzyme Concentrations.....	50
2.5 System Modeling for Capacitive Sensing.....	53

2.5.1 Electrical Behavior of Biomaterial Films .....	53
2.5.3 Sensor Characterization with Varying Film Thickness .....	55
2.6 Conclusions.....	62
3. Chapter 3: Packaging and System Miniaturization for Gastrointestinal	
Navigation.....	64
3.1 Capsules and Gastrointestinal Sampling.....	64
3.2 System Description .....	70
3.2.1 Sensors and External System Electronics .....	70
3.2.2 Capsule Package Design and Materials .....	72
3.2.3 System Miniaturization and Assembly .....	74
3.2.4 Experimental Procedures for pH Sequences.....	76
3.3 Experimental Results .....	78
3.3.1 Sensor Responses.....	78
3.3.2 Coating Variety and Combinations.....	79
3.3.3 Assembled Capsule Coating and Sensor Responses.....	83
3.4 Mechanical Testing.....	85
4. Chapter 4: Biochemical Capacitive Sensing with Triglyceride Films and Module	
Integration into Capsule System .....	89
4.1 Capsule-Based System Integration .....	89
4.2 Pancreatic Lipase Sensing Strategies.....	90
4.3 System Setup.....	93
4.3.1 Film Deposition .....	93
4.3.2 Sensing Characterization .....	96
4.3.3 SEM Analysis for Film Morphology .....	97
4.3.4 pH-Dependent Sampling and Sensing .....	98
4.4 Results and Discussion .....	98
4.5 Conclusion .....	112
5. Chapter 5: Concluding Remarks.....	114
Highlights.....	114
5.1 Summary .....	115
5.2 Future Outlook .....	120
5.2.1 Gastrointestinal-Simulating Biochemical and Biomechanical Conditions	
.....	121
5.2.2 Anchoring Capsules .....	124
5.2.3 Feedback-Triggered Therapeutic Release.....	126
5.3 Conclusion .....	128
6. Appendices.....	130
6.1 Appendix A: Masks Used.....	130
A.1 Microfluidic Impedance Sensing .....	130
A.2 First Capsule Mask for Capacitive Sensing .....	131

A.3 Sensors used for SPA.....	132
6.2 Appendix B: COMSOL Simulation and Results .....	133
6.4 Appendix C: MATLAB Analysis Code and GUI.....	135
7. Bibliography .....	152

## List of Tables

Table 1-1 Major gastrointestinal enzymes, organized by source and excluding the salivary glands and large intestine, and some of their respective associated health conditions.....	20
Table 1-2 Integrated capsule systems. From left to right: PillCam COLON 2, GI gas sensor, and GI bleeding monitor.....	24
Table 2-1 Ratio of spin-coated film remaining after various enzyme conditions, analyzed with a contact profiler (n = 2). .....	39
Table 2-2 Parameters used for capacitance analysis of gelatin films. ....	59
Table 3-1 Various GI enzymes and their pH for optimal activity [16].....	68
Table 3-2 System Specifications.....	76
Table 5-1 Summary of system parameters for the capsule device with reference to their respective chapters for more detail. ....	117
Table 6-1 Parameters used for the COMSOL simulation. ....	133

## List of Figures

Figure 1-1 Variety of biosensing mechanisms [29].	8
Figure 1-2 Randles-Ershler equivalent circuit models for (a) Faradaic and (b) non-Faradaic EIS. (c) Nyquist spectra for Faradaic EIS for a: $Z_W$ – and $R_{et}$ – controlled system, b: $Z_W$ – controlled system, and c: $R_{et}$ – controlled system. Reproduced with permission from [39].	11
Figure 1-3 Scheme for impedance biosensors when using (a) a modified working electrode or (b) two interdigitated electrodes in plane. Reproduced with permission from [28].	13
Figure 1-4 Illustration of the pancreas with insets representative of its exocrine and endocrine cell types. (Image credits: Wikimedia commons).	13
Figure 1-5 Reduction of pancreatic trypsin and amylase output with various pathologies. Reproduced and modified with permission from [1], [2].	17
Figure 1-6 a) Trypsin and b) lipase cleaving mechanisms on peptides and triglycerides, respectively.	18
Figure 1-7 (a) Process for fabricating peptide-crosslinked hydrogels over gold IDE sensors, specifically for sensing MMP-9 with EIS, and (b) 10 Hz impedance response of resulting sensor to different MMP-9 concentrations. Reproduced with permission from [95].	21
Figure 1-8 Examples of integrated capsule systems. From left to right: PillCam COLON 2, GI gas sensor, and GI bleeding monitor. Reproduced with permission from [97]–[99].	23
Figure 2-1 Schematic of collagen denaturation into gelatin. Reproduced with permission from [127].	30
Figure 2-2 (a) Schematic of sensor fabrication. Step 1 entailed photolithography and E-beam deposition of Cr/Au for 20nm/200nm, then liftoff with acetone. After overlaying a 75 $\mu\text{m}$ thick PVC film, 5% gelatin in buffer was spin-coated at 400 rpm for 30 sec, cooled overnight, then crosslinked with 0.5% glutaraldehyde solution to improve thermal stability. After PVC removal, gelatin was measured using a contact profilometer at thicknesses of 300-700 nm. (b) Microscopic image of the resulting sensors.	34
Figure 2-3 (a) Fluidic reaction chamber for testing sensors with enzyme solutions. (b) Schematic of the film-coated sensor and experimental chamber (left). Photograph of Experimental setup (right).	36
Figure 2-4 Resulting interdigitated finger electrode (IDE) sensors, with (Left) and without (Right) gelatin films, (a) pre-exposure to solutions, and post-exposure to (b) buffer; (c) trypsin; or (d) all three enzymes in buffer. Scale bar = 1 mm.	39
Figure 2-5 Representative SEM images of drop-cast, crosslinked gelatin films. Edge views of film (a) without exposure to enzyme solutions and (b) after exposure to trypsin, and top views of film (c) after exposure to trypsin and (d) after exposure to all three enzymes in buffer.	40
Figure 2-6 Representative impedance responses at 10 kHz of sensors, either uncoated or coated with a gelatin film, to trypsin at 1 (both film and no film), 0.5 (film only) and 0 mg/mL in phosphate-buffered saline (Control). “Trypsin—No Film” represents	

the impedance of PBS over the sensor, and “Control—Film” represents the impedance of the film after equilibrating with the PBS. The error bars plot the temporal change in impedance at respective time points (temporal span = 3, n=3)... 42

Figure 2-7 Representative Bode and Nyquist plots for progressive exposure of (a-c) uncoated and (b-d) gelatin-coated sensors to 1 mg/mL trypsin in buffer. Continuous (-) and dotted (--) lines indicate  $|Z|$  and the phase, respectively. (n=3). ..... 43

Figure 2-8 Representative impedance responses at 10 kHz of sensors, either uncoated or coated with a gelatin film, to trypsin, amylase, or lipase, each at 1 mg/mL, or combinations of each enzyme with trypsin. The error bars plot the temporal change in impedance at respective time points (temporal span = 3, n=3). ..... 45

Figure 2-9 Representative Nyquist plots for gelatin-coated sensors to (a) 1 mg/mL lipase; (b) 1 mg/mL amylase; and (c) trypsin, amylase, and lipase, each at 1 mg/mL over time. (n=3). ..... 47

Figure 2-10 Representative QCM response of gelatin film to (a) trypsin at 1, 0.5 and 0 mg/mL in PBS, (b) trypsin, amylase, or lipase, each at 1 mg/mL, or (c) combinations of each enzyme with trypsin (each at 1 mg/mL). (n=3). ..... 49

Figure 2-11 Gelatin film responses to varying trypsin concentrations through analysis of resulting %change in in (a) mass and (b) thickness, with each sample removed from incubation at different time points. Error bars depict standard deviation (n=3). 51

Figure 2-12 Logarithmic rate of reactions of gelatin films in solutions with varying pancreatic trypsin concentrations, calculated using the slopes in percent change of film mass and thickness. Error bars depict standard deviation (n=3). ..... 52

Figure 2-13 (a) Equivalent circuit model and (b) schematic for thin films over impedance sensors. Reproduced with permission from [39]. ..... 54

Figure 2-14 (a) Resulting gelatin film thicknesses and different spin speeds, both pre- and post- rinsing with DIH<sub>2</sub>O. (b) Top-level view of example sensor outline, with each sensor label. (c) Resulting film thicknesses for each spin speed, broken down by sensor – using labels from (b) – and rinsing. Error bars depict standard deviation (n=3). ..... 56

Figure 2-15 (a) Series equivalent circuit mode of LCR meter. (b-c) Electrical (capacitive and resistive, respectively) analysis of sensors across varying electrode spacings and comparing between the presence and absence of a film. Error bars depict standard deviation (n=3). ..... 58

Figure 2-16 Regression analysis of different gelatin film thicknesses and their impacts on sensor (a) capacitance and (b) resistance across 25, 50, and 75  $\mu\text{m}$  electrode spacings. .... 60

Figure 3-1 Modules contained within endoscopy capsule: (1) Optical Dome, (2) LED, (3) Short-focus lens, (4) CMOS image sensor, (5) RF model, (6) MCU, and (7) Power model [176]. ..... 66

Figure 3-2 Human GI tract morphology with respective pH ranges. Reproduced with permission from [184]. ..... 68

Figure 3-3 Depiction of system outlook and application (Image credits: National Cancer Institute). Polymer coatings are intended to dissolve at either the stomach (pH 1.5-3) or the duodenum (pH 7-8.5). At the duodenum, gastric acid-neutralizing bicarbonate is secreted from the pancreas via the sphincter of Oddi. .... 70

Figure 3-4 System electronics overview. Circuit design includes a multiplexer (MUX) integrated circuit (IC), a capacitance-voltage-converter (CVC) IC, a 1.5 MHz step-up DC-DC converter, and a BLE system-in-package (SiP) micro-controller unit (MCU). ..... 72

Figure 3-5 (a) Circuit calibration with known capacitors across four multiplexed inputs. The resulting system senses capacitive changes in the 0.8-220 pF dynamic range with a sensitivity of  $3.2 \times 10^{-3}$  pF/mV and operated using a 3.3 V source. (b) Data comparison between Bluetooth versus serial (UART) communication in different experiments, where the capsule (open gratings) was measured in air, inserted into buffer, then removed. Error bars depict standard deviation (n=4). ..... 72

Figure 3-6 (a) CAD model of the capsule used with external circuit. (b) 3-D printed version with zoomed up view of gratings. Scale bar = 1 mm. .... 73

Figure 3-7 Cross-sectional optical images of the sampling gratings (a) uncoated and (b) with 1 coating of polymer, where yellow arrows indicate the grating locations and yellow boxes indicate the inlets. (c) Characterization of polymer coating thickness vs. number of dipping steps from both non-grating and grating regions over the 3-D-printed capsule surface. Error bars depict standard deviation (n=3). Scale bar = 1 mm. .... 74

Figure 3-8 (a) PCB rendering with sensor die fixated between designated pads using epoxy. Contact was made by curing conductive silver ink. (b) Schematic of the assembled capsule setup. (c) Calibration of BLE MCU at the PCB level using standard known capacitors. (d) Photograph of assembled capsule. Scale bar = 5 mm unless otherwise specified..... 76

Figure 3-9 Sensor responses (inserted into buffer at 5 min) of capsules with different numbers of S 100 coatings (0, 2, 3, and 4, respectively) with increasing pH using titers of 1 M NaOH. Error bars depict standard deviation (n=4). Chamber filling is characterized by a capacitance change of ~50 pF from the initial capacitance in air. For each formulation, it was determined that 3 coatings were optimal for the w/v% used. .... 79

Figure 3-10 Sensor responses inserted into capsules with different types of coatings (3 dip-coatings each) compared to uncoated controls: (a) L 100, (b) E PO, and (c) combined coatings, where E PO is outer-most and L 100 is between the 3-D-printed capsule and the E PO layers. Error bars depict standard deviation (n=4). (d) Capsule rendering for displaying coating conditions for each sequence. .... 82

Figure 3-11 Real-time representative trials of capacitance measurements obtained via BLE from the 3x coated capsule immersed in control (neutral, pH 7) (red) and specific target (blue) pH (acidic, pH 3). The rapid increase in capacitance represents buffer inflow and contact with the sensors, due to coating dissolution. (n=2). ..... 84

Figure 3-12 Progression of polymer coating throughout (a) control and (b) pH-based dissolution tests. Beginning, 30 minutes, and 1 hour immersion periods are from the left, middle, and right, respectively. Scale bar = 3 mm. .... 84

Figure 3-13 (a) Diagram illustrating the regions along each axis where pressure was applied along the load frame. The colors are used for reference in (b) the applied force profiles for each setting. The failure point for each is indicated with each black circle. (c-d) Representative photographs of the capsule package upon reaching failure more for “vertical” and “on side” setups, respectively. (n=1 for each condition). .... 86

Figure 4-1 (a) Lipase-induced hydrolytic digestion of stearin into glycerol and three stearic acid molecules. (b) Bile salt-induced emulsification of triglyceride globules into micelles. ....	94
Figure 4-2 Deposition strategies for obtaining TG films over sensors: (a) drop-casting and (b) dip-coating of molten TG solution while the substrates were either left at ambient or pre-heated to TG melting temperature for 5 minutes. (c) Dip-coating of assembled capsules into dyed pH-sensitive copolymer solutions to form GI-targeting coatings, repeated for sequential coatings. ....	95
Figure 4-3 Assembly process for platform. Steps 1-4 used for sensor characterization of TG-SPAs with connection of VDD and GND to external power supply, while Steps 5-8 are used for testing complete capsule. At Step 5, after connection to Lithium polymer battery. Deep Sleep mode is entered for a 3-hour time period via transmitted signal to allow for curing of adhesion and coating materials at respective steps. After Step 8, capsule electronics enter Active mode to enable capacitance measurements and signal transmission to mobile phone. ....	96
Figure 4-4 (a) Schematic depicting normal GI pH progression along with adjacent organs. (b) Experimental setup for complete capsule characterization. ....	98
Figure 4-5 Resulting thicknesses in films with each deposition strategy and initial SPA temperature. Error bars depict standard deviation (n=3). ....	102
Figure 4-6 Representative sensor response testing after insertion of TG-SPAs into buffer solution (0.1 M PBS) when TG film composed of either pure stearin or stearin:glycerol (S:G) ratios of 2:1, 1:1, or 1:2. Film most stable, i.e. least response over time, with the 2:1 S:G ratio compared to other compositions. (n=2). ....	103
Figure 4-7 Sensing in the presence of different biochemical species at varying concentrations. (a) PL, (b) BAs, and (c) pancreatic trypsin. ....	105
Figure 4-8 Representative SEM images for characterization of SG films after exposure to various solutions at 30- and 60-minute time intervals. (n=3). ....	108
Figure 4-9 (a) Combined pH sampling and enzyme sensing in integrated capsule. Measurements were initiated after immersion into acidic solution for 25 minutes (blue), after which the capsules were removed and immersed into a neutral solution (red), where a spike was observed around 19 minutes, indicated by the circle. Finally, the capsule was removed and immersed into a solution containing 1 mM lipase (black), where a distinct increase in capacitance is observed, indicated by the arrow. (b) Photographs taken of the capsule at the end of each respective sequence, designated by the label color: b-i: acid condition, b-ii: neutral condition, b-iii: lipase condition, and b-iv lipase condition after removal from the solution. (n=1). ....	110
Figure 5-1 Depiction of application. The capsule is protection in environmental pH reflecting that of the stomach until reaching the small intestine via pH-sensitive polymer coating. Upon dissolution, the fluid is sampled via embedded gratings, and pancreatic lipase reacts with triglyceride coatings to increase the capacitance of the sensors. This is transmitted to a phone wirelessly, and the data can be shared with medical practitioners. ....	117
Figure 5-2 (Left) Schematic and (right) optical images of sensors with deposited film. The optical images indicate distinct removal of film after trypsin response compared to buffer alone, where the film remains relatively intact. ....	118

Figure 5-3 (a) Top and (b) bottom views of sensor-connected PCB, and (c) photograph of assembled capsule. Scale bar=5 mm. ....	119
Figure 5-4 Peristalsis simulator, consisting mostly of 3D printed components. ....	124
Figure 5-5 SEM imaging of (a) porcine (reproduced with permission from [246]) and (b) 3D-printed villi with an EnvisionTEC Perfactory 4. (c) Implantation capsule robot (reproduced with permission from [249]). (d) 3D-printed anchoring concept for passive capsule implantation; left inset: head of Taenia Solium Scolex (reproduced with permission from [248]), right inset: close-up of microhook mimic. ....	126
Figure 5-6 Physiology of GI affected regions, reflecting potentially relevant information accessible by capsule devices. ....	127
Figure 6-1 IDE sensors used in chapter 2. Finger width: 2 $\mu\text{m}$ , finger spacing: 4 $\mu\text{m}$ , finger length: 1 mm, number of fingers per electrode: 65. ....	130
Figure 6-2 IDE sensor patterns used in chapter 3 to measure integrity of the packaging coatings. (a) Complete photomask with 10 die for each 4x1 sensor die, each with different finger geometries: 25, 50, and 75 $\mu\text{m}$ width and spacing and 44, 22, and 14 fingers per electrode, respectively. Finger length: 2 mm. ....	131
Figure 6-3 IDE sensor patterns used in chapters 3 and 4 for SPAs. Mask Design: 124 Sensor Output, 62 each of long (length=3 mm) /short (1.5 mm) versions. Number of fingers per electrodes = 40. ....	132
Figure 6-4 (a) Cross-section of simulation model (top to bottom: medium, film, sensor, wafer), (b) mean capacitance from experimental degradation of film over IDE sensor (left y-axis) and simulation (right y-axis) results. Between electrode fingers, electric field intensity increases significantly in the presence of gelatin. Electric field height decreases significantly, the magnitude remains the same, and lateral electric field distribution is altered. ....	135
Figure 6-5 MATLAB GUI. Up to four data sequences can be plotted, three of which can be plotted individually on the right while all are overlaid in the plot on the bottom left. Features that can be modified directly in the GUI are smoothing filters, axes limits, and legend labels. ....	151
Figure 6-6 Depiction of data format in .csv file. This format is currently programmed into the app, while the algorithms to process the capacitance data are embedded in the MATLAB code above. ....	151

## List of Abbreviations

AC: Alternating current

ADC: Analogy-digital converter

BA: Bile acids

BAEE: N $\alpha$ -Benzoyl-L-arginine ethyl ester

BLE: Bluetooth Low Energy

CA: Carbohydrate antigen

CCK: Cholecystokinin

CEA: Carcinoembryonic antigen

COTS: Commercial off the shelf

CT: Computed tomography

CTC: Circulating tumor cells

CVC: Capacitive-voltage converter

ctDNA: Circulating tumor deoxyribonucleic acid

DC: Direct current

DI: Deionized

DNA: Deoxyribonucleic acid

EGD: Esophagogastroduodenoscopy

EIS: Electrochemical impedance spectroscopy

ENPD: Endoscopic nasopancreatic drainage

EPI: Exocrine pancreatic insufficiency

ERCP: Endoscopic retrograde cholangiopancreatography

ERP: Endoscopic retrograde pancreatography

FC: Film-coated chip

FDA: Food and Drug Administration

FDM: Fused Deposition Modeling

FET: Field-Effect Transistor

FFA: Free fatty acids

FNA: Fine-needle aspiration

GI: Gastrointestinal

GL: Gastric lipase

GUI: Graphical user interface

IBD: Inflammatory bowel disease

IBS: Irritable bowel syndrome

IC: Integrated circuit

IDE: Interdigitated electrodes

MCU: Microcontroller unit

MEMS: Microelectromechanical systems

MMP: Matrix metalloproteinase

MRCP: Magnetic resonance cholangiopancreatography

MUX: Multiplexer

PA: Pancreatic adenocarcinoma

PBS: Phosphate buffered saline

PCB: Printed circuit board

PET: Positron emission tomography

PFT: Pancreas function testing

PL: Pancreatic lipase

PVC: Polyvinyl chloride

QCM: Quartz crystal microbalance

RF: Radiofrequency

RNA: Ribonucleic acid

RPM: Revolutions per minute

SAW: Surface acoustic wave

SEM: Scanning electron microscopy

SiP: System in package

SG-SPA: Stearin and glycerol coated sensor-printed circuit board assembly

SPA: Sensor-printed circuit board assembly

TAME: p-toluene-sulfonyl-L-arginine methyl ester

WSTK: Wireless starter kit

# 1. Chapter 1: Introduction

## 1.1 Background and Motivation

The gastrointestinal (GI) tract is a complex canal that, while composed of distinct organs with respective functions, hosts a wide range of biochemical and biomechanical interactions critical to homeostasis. To maintain various organ functions, there is a continuously evolving dependence on understanding the functional status at any given time through GI diagnostics in particular, which range broadly depending on the suspected condition, how it is known to manifest in physiological processes, and its severity.

One example of a physiological process that can require monitoring – and is a major focus of this dissertation – is exocrine pancreatic function, which is critical to maintaining one’s nutritional intake at the very least, but is often compromised in a variety of pancreatic pathologies, including pancreatitis, pancreatic adenocarcinoma (PA), and cystic fibrosis [1]–[3]. While various aspects of human physiology and the procedures involved are well understood by physicians and medical researchers, current diagnostic tools reliant on biomarkers – objective medical indicators of a physiological state – suffer from a combination of limited specificity or sensitivity, high cost and invasiveness, or only detect the condition severity at the point at which efficacy of traditional therapies has diminished [4], [5]. Though biomarkers vary with condition, enzymes, which are a class of proteins naturally synthesized in cells to catalyze (or accelerate) biochemical reactions, have been demonstrated as physiological indicators and remain a major category of biomarkers [6]. There are further subclasses of enzymes required for food digestion and nutrient absorption in the

GI tract: proteases (trypsin, chymotrypsin, and elastase), lipases (steapsin), and amylases ( $\alpha$ -amylase). These enzymes are secreted in either active forms or precursors (zymogens) by the pancreas in a bicarbonate solution, or buffer, that enters the gastrointestinal (GI) tract – into the duodenum – by way of the pancreatic duct [7]. Additional markers such as carcinoembryonic antigen (CEA), carbohydrate antigen (CA) 19-9, or specific microRNAs have been found present in these secretions that correlate with early stages of PA [8], [9].

Recently, there has been a surge in advanced microsystem development driving innovation for ingestible sensors capable of replacing or aiding invasive clinical methods [10]–[12]. Such devices are designed to reveal new information about physiological responses to various stimuli (discussed in detail in Section 1.3.4), depending on the sensor types and the materials used to modify them [13]. However, none have been used to measure enzyme activity, which can be invaluable to expanding their utility. Moreover, consistent with Moore’s law, microelectronics have advanced to point where circuit footprints can cost-effectively be fabricated in reduced sizes while increasing complexity [14]. The primary challenge remains how to leverage this for interfacing with biomaterials such that we can measure physiological processes in regions where smaller systems are at a great advantage for obtaining previously inaccessible data. This challenge is augmented by the chaotic nature of the GI tract, especially for integrating the microelectronics into the ingestible, autonomous devices that must navigate through it [15].

Distribution of specific tasks, such as safe navigation and specific sensing, to different modules is critical for embedding functionality in complex systems and

devices [16]. Modular integration can be difficult when each requires a different fabrication method, hence the growing utility of more custom tools such as the variety that fall under the category of 3D-printing, including stereolithography, photopolymer jetting, laser sintering, and fused deposition modeling (FDM), among others [17]. Furthermore, features such as biocompatibility and biodegradability have become common and almost essential themes in many bioelectronics devices for providing safe interfaces with other biologics and embedding sustainability, respectively [18]–[21]. This doctoral research aims to overcome these challenges and demonstrate the development of a wireless integrated capsule microsystem for navigating the GI tract, sampling pancreatic secretions, and monitoring enzyme activity *in situ* for indicating pathological conditions. I anticipate that this system will lay the foundation for hybrid fabrication and integration methods toward measuring a broader range of GI targets.

### 1.2 Summary of Accomplishments

In this work I leveraged biochemical properties of various materials as coatings individually designated for (1) packaging our system to sample fluid with a specific pH characteristic of a target GI region and (2) insulating our sensors until degrading in response to catalytic pancreatic enzymes. Specifically, I integrated these features into an ingestible capsule designed for ingestion and autonomously navigating through the GI tract via natural peristaltic forces for sampling pancreatic secretions, measuring pancreatic enzyme activity, and wirelessly transmitting the data via smartphone interface for external analysis. I envision using this platform as a system for not only targeting specific regions in the GI tract by utilizing a variety of coating materials, but for sensing different enzymes that might be in those regions. This broadens the

applicable conditions for which this device could be used, limited only by current understandings of how GI secretions vary with these conditions. Such a platform would minimize efforts and intermediaries between the physician and the source of a patient's pathology, with the potential for aiding in differential diagnostics. Toward enabling this research, three primary objectives were investigated: biomaterial-based electrical transduction systems for measuring duodenal enzyme activity, packaging materials for system protection and GI region targeting, and integrating these systems to function simultaneously into an independent device.

#### 1.2.1 Investigation of Biomaterial Film-Based Electrical Transduction Systems for Measuring Enzymatic Activity

This work begins with the investigation of thin films made from biomaterial substrates that respond preferentially to health-related enzymes of interest. In this part of the thesis, I developed a variety of deposition parameters for obtaining thin films of gelatin and their subsequent crosslinking over both wafer- and individual sensor-level substrates. The protocols developed here are the first time of not only depositing glutaraldehyde-crosslinked gelatin films over impedance sensors and the characterization of the impact of different spin-coating parameters on their resulting thicknesses, but determining and confirming the change in various impedance elements, including resistance and capacitance, with respect to these varying thicknesses. Furthermore, we established relationships between the rate at which these film thicknesses, and ultimately impedance, change in response to local concentrations of a pancreatic trypsin (1  $\mu\text{g/mL}$  – 1  $\text{mg/mL}$ ). The impact of these methods and characterizations is that they enable further work on integrating similar films, i.e. those

from either gelatin-based hydrogels or other biomaterials, with traditional MEMS technology and utilizing them for more advanced developments in enzyme detection through impedance sensing.

#### 1.2.2 Investigation of Embedded Packaging Materials for Gastrointestinal Targeting

Due to naturally occurring pH gradients in GI regions and their contents, polymer coatings commonly used in the pharmaceutical industry for dissolving in a specific pH, provides a mechanism for GI targeting [22]–[24]. This aim resulted in the development of a microelectronics sensing platform that leverages these polymers as coatings in combination with a biocompatible 3D-printed capsule structure as a hybrid package to protect internal system elements from nonspecific environmental stimuli. The platform was designed using off-the-shelf components to acquire changes in sensor capacitance for downstream utility in measuring changes in biomaterial film thickness from enzyme reactions as described in Aim 1. This capacitance measurement is then transmitted wirelessly using Bluetooth Low Energy (BLE) for real-time measurement control, realized through the use of a facile user interface via an Android app. Using similar methods used for coating therapeutic capsules in drug delivery applications, I adapted a dip-coating protocol for layering the pH-sensitivity polymers over our 3D-printed capsules, which allow a sensor-sample interface using microfluidic gratings that allow fluid inflow, while subsequently developing an assembly process that maintains functionality of the individual modules (i.e. sensors, power supply, electronics, etc.) required for autonomous operation of the device. These processes serve to promote the targeting capabilities of future ingestible devices while offering insight as to interfacing MEMS sensor signals with users such as patients or clinicians.

### 1.2.3 Development of Ingestible Integrated System for Targeted Gastrointestinal Sampling and Enzyme Sensing

The third accomplishment of this work is the development of triglyceride film-based deposition and sensing strategy for detecting biochemical species present in the duodenum and its subsequent integration into a GI-targeting capsule system that can sample simulated fluid in the duodenum. We leverage deposition methods such as dip-coating and drop-casting for triglyceride films over the sensor surfaces utilized in Aim 2, and determine their respective limitations in comparing process parameters such as film composition and substrate preparation. This is the first demonstration of utilizing a purely capacitance-sensing platform for measuring reactions between triglyceride films, specifically from stearin and glycerol, and duodenal analytes such as pancreatic lipase or bile acids. Furthermore, we are the first to reveal morphological changes of such films after undergoing hydrolytic and emulsification reactions to lipase and bile acids, respectively, compared to buffering fluid alone or with local trypsin as a nonspecific analyte. The assembly process used for integrating the capsule modules in Aim 2 is modified further to maintain reactive films over the sensor surfaces for subsequent testing in the pH-soluble polymer-coated capsules, establishing various required considerations and validating the feasibility of pH-targeted sampling and sensing. The successful development of this device will enable further advances in both novel hybrid fabrication strategies for integrated device development and exploratory endeavors for GI evaluation with ingestible microsystems.

### 1.3 Literature Review

This section provides the necessary background and literature review as applicable to the presented work. First, I will discuss previous work on electrical sensing systems for biological species and their requirements for successful operation. Next, I will present a review on the current state of traditional GI diagnostic tools with an emphasis on pancreatic health. I will then expand on pancreatic enzyme and substrate interactions while introducing similar species present through the GI tract. Finally, recent advances in ingestible systems for addressing challenges in GI health will be evaluated, introducing the rationale for various design choices made during this work.

#### 1.3.1 Electrical Biosensors

In general, biosensors are devices that convert the presence of biological molecules or activity into an observable signal [25]–[27]. Biosensors are often designated to measuring biomarkers, which, in a clinical setting, are indicators for normal or pathological function of physiological processes. Figure 1-1 illustrates the general mechanism for a biosensor. The most common signals processed in biosensors are electrical, optical, mechanical, and magnetic, though this dissertation will emphasize efforts for interfacing biomolecules on electrical biosensors. Their performance can be defined through the following criteria: sensitivity, working and linear concentration ranges, detection limits, selectivity, reliability, response time (steady-state or transient), sample throughput, reproducibility, stability, and lifetime [28].

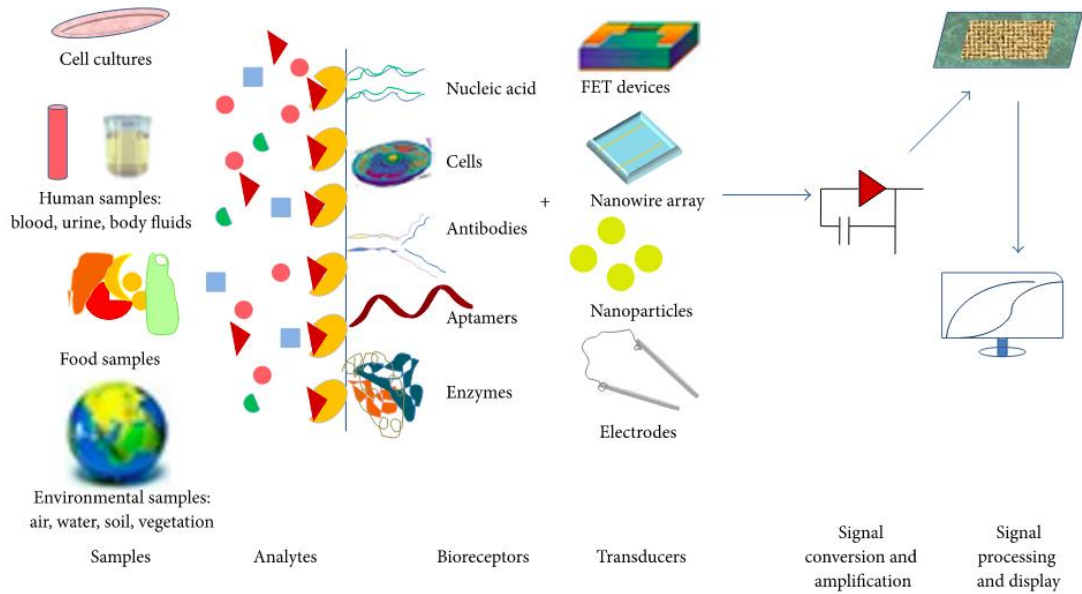


Figure 1-1 Variety of biosensing mechanisms [29].

Electrical or electrochemical biosensors rely on a biological system’s ability to directly alter an electrical signal, generally in the form of a simple applied voltage or current [30], [31]. These sensors are popular as they do not require intermediate transduction mechanisms, can be easily miniaturized for subsequent integration with most microelectronic systems, are low cost to produce and, depending on the structure can be fashioned to be mechanically robust. Additionally, while innovations in sensing generally aim to expand the detection limits and ranges, the concentrations of the targets of interest, discussed more in section 1.3.2, are relatively higher, allowing the use of simpler systems. The signals are frequently measured as either impedimetric or conductometric (interdigitated, metal electrodes), potentiometric (ion-selective, glass, gas, or metal electrodes), amperometric (metal, carbon, or chemically modified electrodes), or field-effect transistor (FET, ion or enzyme sensitive), and induce an increase or decrease in signal with respect to a change in surface characteristic from a bio-functionalized sensor material [28]. The medium of applied excitation is desired to

possess a certain threshold of conductivity that would enable electron transport from the source to receiver, hence the use of metals such as gold or platinum as the path of travel.

One primary challenge of these sensors is determining the appropriate method for interfacing the material of the transducer – typically an electrode – with the biological materials. The latter can include proteins, carbohydrates, lipids, nucleic acids, or even just ions released from a physiological function. One of the most ubiquitous clinical biosensors is the glucose sensor, which operates amperometrically by relating change in current to the amount of enzyme catalysis between glucose and glucose oxidase, the latter of which is the material bound to the sensor surface. The reaction, based on reduction-oxidation, results in electron generation, thereby increasing the current at the peak potential of an electrochemical cell. The peak potential is specific to the experimental condition, though the current can be approximated by the Nernst equation (1):

$$E = E^0 + \frac{RT}{nF} \ln \frac{(Ox)}{(Red)} \quad (1)$$

Here,  $E$  is the cell potential,  $E^0$  the standard potential of a species,  $R$  the universal gas constant (8.314 J/(mol·K)),  $n$  the number of electrons,  $T$  the temperature, and (Ox) and (Red) the relative activities of the oxidized and reduced analytes at equilibrium [32]. This is used to determine concentrations of electrochemical activity, and is popular among other electrical biosensing strategies due to its high sensitivity, compatibility with microfabrication processes, minimal power requirements, and economical cost, among others [25]. These systems require two or three electrodes. Both require (1) a

*working* electrode for responding to the target analyte and (2) a *counter* electrode to balance the reaction. Three-electrode systems possess an additional *reference* electrode to maintain a constant potential independent of the solution properties.

Direct electron transfer is the ideal scenario for electrochemical sensing systems as it results in simpler designs. However, this only occurs with species that already possess a charge, including ions. Some sensors require a secondary substrate; using the glucose sensor as an example, glucose oxidase is required to generate the electron via catalytic reaction. In other scenarios, mediators are implemented that react with the electrode, such as ferrocyanide or ferrocene derivatives, that avoid interfering with other reactants in the solution and possess lower potential requirements [33]. Both options lead to new design requirements in the system, i.e. methods to ensure the secondary substrate or mediator is constantly within range or access of the electrode surface. While this is not a problem with most benchtop setups, integrated systems that rely on isolated sensing chambers must adapt methods for ensuring their containment. One purpose of mediators is their ability to amplify reactions as a means of embedding specificity to the sensor. Another method toward this end is the utilization of membranes that filter interfering species access to the sensor surface or provide an additional layer for substrate immobilization. For example, nitrocellulose filters are fabricated with pores that can reach 0.22  $\mu\text{m}$ , which is permeable to fluid flow to underlying sensors while maintaining protein-retaining properties [34]. Further, lipid bilayer membranes have been utilized for mimicking physiological conditions [35]. In addition to adding further fabrication and design steps, however, such membranes are

often at risk of fouling or pore saturation, thereby requiring solutions for mitigation such as treatments that increase hydrophobicity [36].

In contexts where no redox species are involved and changes in electrical signals at different frequencies, i.e. AC systems, adds value to understanding a mechanism of reaction, electrochemical impedance spectroscopy (EIS) is another viable sensing technique. EIS, which can be categorized into Faradaic and non-Faradaic subgroups based on their respective requirement and absence of a reference electrode, offers information on changes in the chemical interface of modified electrodes, modeled specifically using the Randles and Ershler equivalent circuit, as well as reaction rates through sequential spectra [37], [38]. The model for Faradaic EIS is displayed in Figure 1-2, while the resulting equation is as follows:

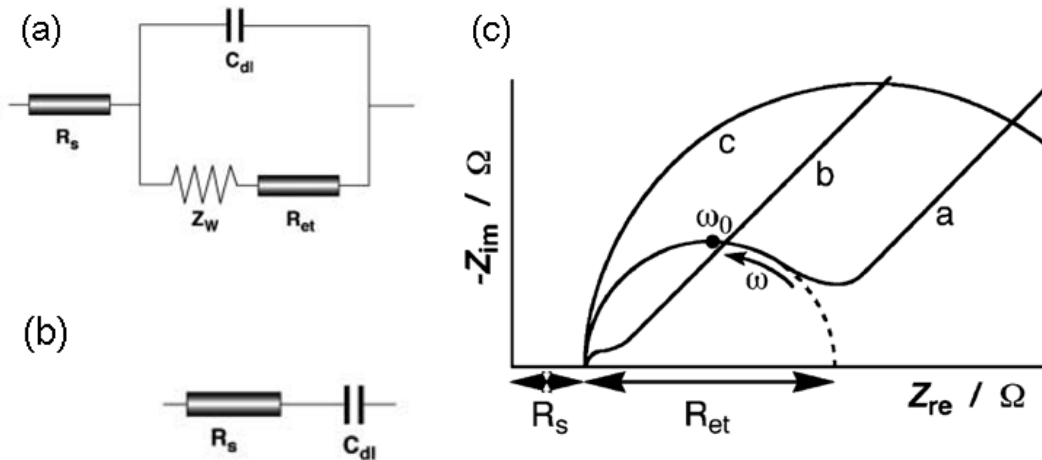


Figure 1-2 Randles-Ershler equivalent circuit models for (a) Faradaic and (b) non-Faradaic EIS. (c) Nyquist spectra for Faradaic EIS for a:  $Z_w$  – and  $R_{et}$  – controlled system, b:  $Z_w$  – controlled system, and c:  $R_{et}$  – controlled system. Reproduced with permission from [39].

$$Z(\omega) = R_s + \frac{R_{ct}}{1 + \omega^2 R_{ct}^2 C_d^2} - \frac{j\omega R_{ct}^2 C_d}{1 + \omega^2 R_{ct}^2 C_d^2} = Z' + jZ'' \quad (2)$$

Here,  $Z$  is the total impedance,  $R_s$  and  $R_{ct}$  (shown in Figure 1-2 as  $R_{et}$ ) are the solution and charge transfer resistance, respectively,  $C_d$  is the double-layer capacitance and  $\omega$  is

the frequency.  $Z_w$  in the figure represents the Warburg impedance, which is the result of ion diffusion from the solution to the electrode surface. The equation identifies the total impedance as two distinct parts:  $Z'$  and  $Z''$ , which are the real and imaginary impedance, respectively. These are often analyzed by plotting against one another to form Nyquist plots, which produce spectra that offer information on the individual circuit elements [39], [40]. This can provide insights as to biochemical events occurring at the electrode surface, depending on which circuit element is affected. This topic will be further discussed in relation to this work in chapter 2.

As discussed earlier in this section, electrical and electrochemical-based measurement systems are well suited for integration with microelectronics systems, which makes them applicable for point-of-care and, as demonstrated throughout this thesis, capsule-based systems. There are many that are already used for measuring a variety of biomarkers, including pathogens and toxins, in the clinical setting, though a major limitation of EIS is generally the lack of labelling processes involved, which reduce sensitivity and performance in complex media such as blood. However, they continue to increase in popularity and efforts remain to improve surface and binding strategies of targets. A general schematic of how the sensors are arranged is depicted below, while more information on specific impedance-based biosensors and their respective performances can be reviewed in other works [41], [42].

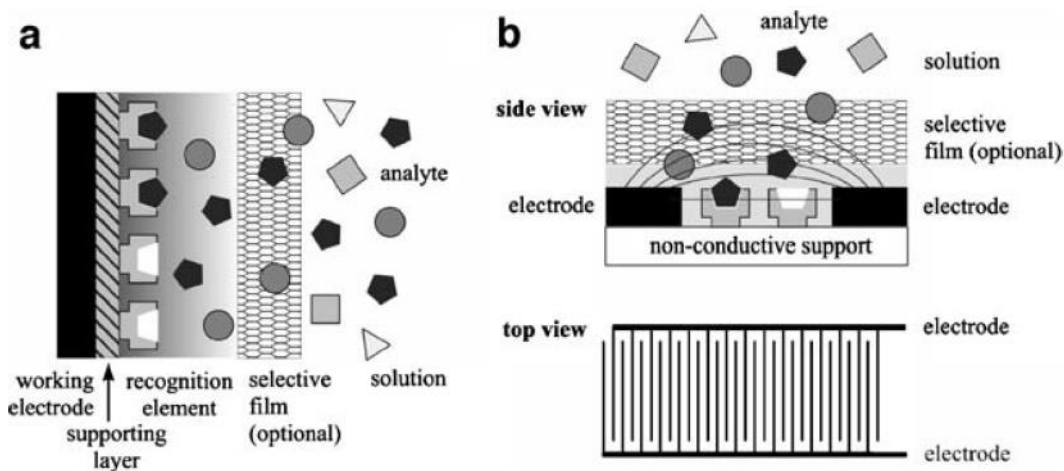


Figure 1-3 Scheme for impedance biosensors when using (a) a modified working electrode or (b) two interdigitated electrodes in plane. Reproduced with permission from [28]

### 1.3.2 Exocrine Pancreatic Health and Diagnostics

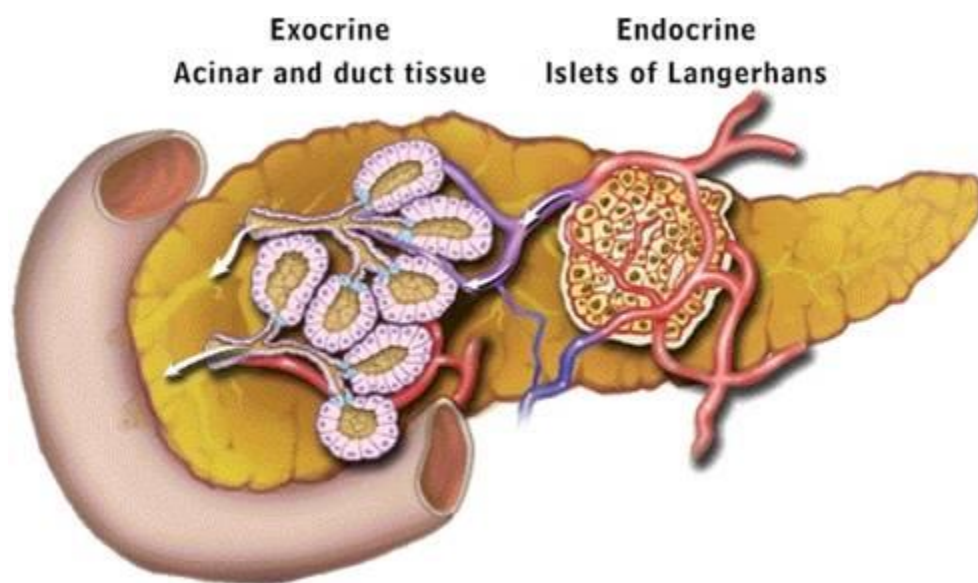


Figure 1-4 Illustration of the pancreas with insets representative of its exocrine and endocrine cell types. (Image credits: Wikimedia commons).

This section will describe the clinical topic of interest in designing our biosensors. The human pancreas, illustrated in Figure 1-4, is a focus in this dissertation due to its relationship to the GI tract and the general difficulty associated with its various diagnostics. It is a gland comprised of an endocrine and exocrine system, the

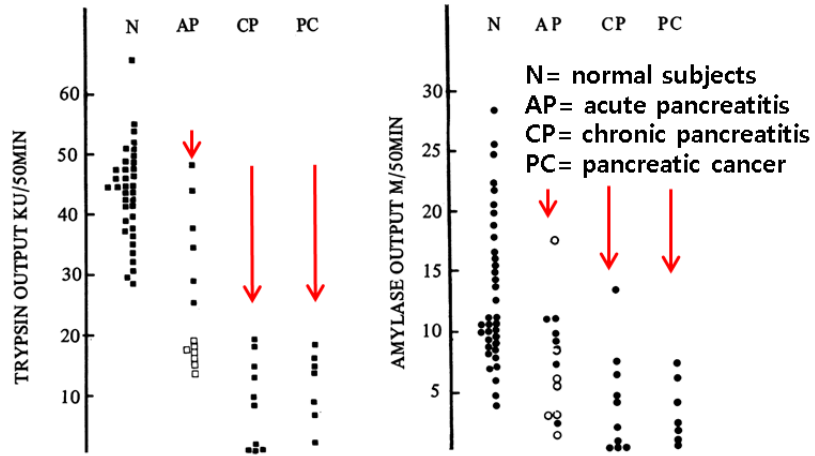
latter of which is primarily responsible for secretion of digestive enzymes and sodium bicarbonate into the duodenum, via the sphincter of Oddi, for macromolecular fragmentation and gastric acid neutralization, respectively. The most common pathologies that affect these secretions are pancreatitis (acute and chronic) and various forms of pancreatic cancer. A lack of digestive enzymes, however, is more generally referred to as exocrine pancreatic insufficiency (EPI), and is often present in cystic fibrosis, a primarily endocrine affected pathology [3], [43]. Before diagnosis of these conditions however, a patient must present various symptoms as part of the screening process as part of the differential for identifying the exact condition. For example, both pancreatitis and pancreatic cancer can cause upper abdominal pain, jaundice, fever, and/or unexplained weight loss, but further tests are required to verify both the underlying issue as well as the severity of the condition [44], [45].

Current diagnostic strategies for evaluating the pancreas can range from direct analysis of the tissue itself or indirect analysis via its secretion products. Direct analysis is generally the most specific, consisting of imaging techniques for physical abnormalities and blood testing or tissue biopsy for molecular and genetic testing. Imaging tools are gold standards for verifying the presence of a tumor or neoplasm (tumor precursor), or even enlargement or inflammation [4], [46], [47]. Specific strategies include abdominal computed tomography (CT), endoscopic ultrasound (EUS), magnetic resonance cholangiopancreatography (MRCP), magnetic resonance imaging (MRI), endoscopic retrograde cholangiopancreatography (ERCP), or positron emission tomography (PET) [47]–[49]. The primary challenge with these strategies for cancer, unfortunately, is their lack of efficacy in early-stage detection, considering the

images are analyzed and diagnosed by physician ability. EUS is often used to guide biopsy through fine-needle aspiration (EUS-FNA), thereby offering further molecular information but still suffering from high invasiveness. ERCP, while useful for collecting samples for cytological analysis, can occasionally induce pancreatitis, bleeding, and cholangitis [50]. Computer-aided approaches with EUS are also being developed to improve diagnosis rates, and while they have increased performance rates there remains room for improvement [51]. Pancreatitis, alternatively, requires significantly less effort to diagnose. Digestive enzymes such as amylase, lipase, and/or trypsin, for example, can be significantly elevated in serum, while the fecal elastase test is the gold standard when diagnosing severe chronic pancreatitis [4]. The primary blood marker that is a gold standard for identifying the presence of cancer is carbohydrate antigen 19-9 (CA 19-9), though it is not specific to pancreatic cancer and has limited sensitivity for smaller tumors [47], [49], [52], [53]. Other markers include circulating tumor DNA (ctDNA) and cells (CTC) analyzed for KRAS mutations, which can often be used to determine the progression of treatment as well. Unfortunately, these are very difficult to isolate and identify, which only becomes more challenging in the early stages [54].

Pancreatic juices have been investigated as a source of diagnostic information [8], [47], [49], [55]–[57]. Duodenal aspirates have been analyzed for comparing various pancreatic pathologies for differentiation as they have been least physiologically processed and therefore less likely to be contaminated or the contents degraded from spontaneous autolysis, especially for DNA or RNA markers [58]–[60]. The region of secretion in the duodenum is targeted using esophagogastroduodenoscopy (EGD),

endoscopic retrograde pancreatography (ERP), or endoscopic nasopancreatic drainage (ENPD) [57], [61]. Further, genetic and protein analysis has yielded markers such as K-Ras, Smad4, KL-6, PKD, telomerase activity, DNA methylation, CA 19-9, or microRNA's in the juice for cancer, some of which allow for concrete differentiation from pancreatitis [8], [53], [57], [62]. Various analyses have shown differences in digestive enzyme activity from the secretions [1], [63]–[65]. Figure 1-5 illustrates qualitative trends in enzyme output, impacted by various pathologies, as this will be emphasized more throughout this work. Overall, however, sample extraction and analysis can be cumbersome while ultimately losing molecular integrity, thereby driving the need for *in situ* measurements for a combination of several biomarkers discussed above that can be achieved with tools that require less human intervention such as ingestible capsule technology. With tools that can achieve measurements *in situ*, there is greater potential to detect biomarkers at an earlier pathological stage to prevent transit-related sample degradation, while allowing a higher throughput of non-invasive and likely less costly-procedures with less involvement from clinical and laboratory personnel. Furthermore, *in situ* sensing offers the ability for real-time analysis upon data acquisition, enabling a more rapid response for informed decision making. This will be elaborated more in chapters 3-5.



Test meal	Control group		Pancreatic disease	
	Healthy volunteers: Mean ± SE		Chronic pancreatitis: Mean ± SE	Carcinoma of pancreas: Mean ± SE
Trypsin				
Concentration, μg./ml.	163 ± 21	28 ± 11	50 ± 27	
Output, μg./kg.BW	316 ± 52	44 ± 18	112 ± 60	
Amylase				
Concentration, units/ml.	983 ± 152	257 ± 86	419 ± 146	
Output, units/kg.BW	2037 ± 340	294 ± 100	844 ± 439	

Figure 1-5 Reduction of pancreatic trypsin and amylase output with various pathologies. Reproduced and modified with permission from [1], [2].

### 1.3.3 Pancreatic Enzyme Activity and Other Gastrointestinal Fluid Contents

Detecting the presence of multiple molecular markers in pancreatic secretions has the potential to improve the differential diagnosis for pancreatitis or screening for pancreatic adenocarcinoma. Depending on the sensing strategy utilized, accuracy and precision can be optimized to compete with the previously mentioned strategies, limited only by recent advances in technology.

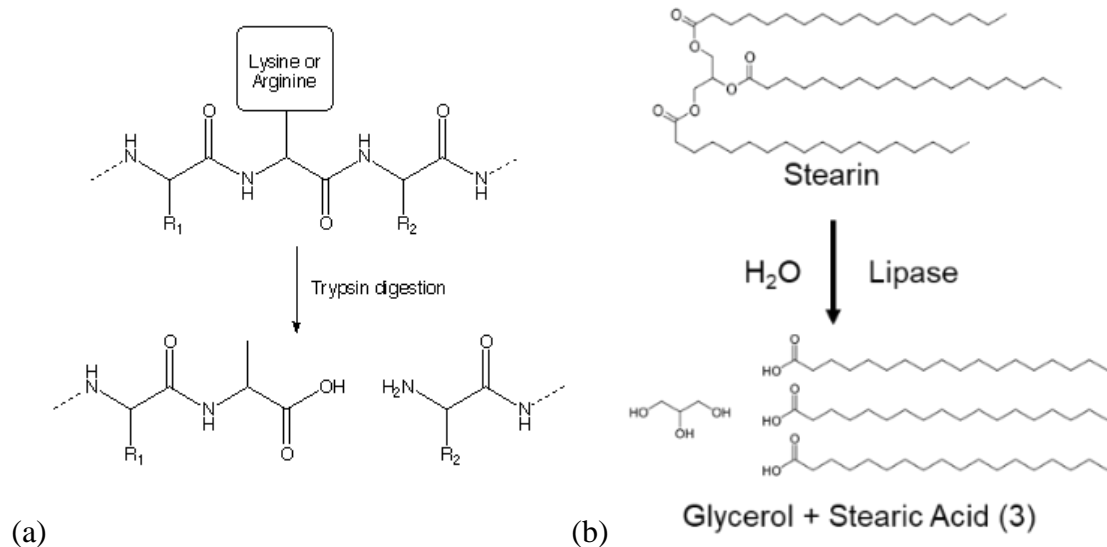


Figure 1-6 a) Trypsin and b) lipase cleaving mechanisms on peptides and triglycerides, respectively.

Many pancreatic enzyme activity biosensors are under investigation that use substrates responsible for hydrolysis with the target enzyme. Trypsin, for example, cleaves peptide chains on the carboxyl ends of amino acid residues lysine and arginine unless proline is present [66], [67]. The mechanism is illustrated in Figure 1-6. Substrates used in standardized or reported assays are  $N_{\alpha}$ -Benzoyl-L-arginine ethyl ester (BAEE) [68] and p-toluene-sulfonyl-L-arginine methyl ester (TAME) [69]. Alternatively, sensors have used poly-l-lysine, cytochrome c, or gelatin [70]–[73]. Pancreatic lipase, however, cleaves triglycerides at ester bonds to form glycerol and three fatty acids. This occurs specifically when the enzyme undergoes interfacial activation, which consists of the enzyme active site becoming uncovered at a lipid-water interface [74]. Substrates used in assays or sensors include olive oil, composed 4-30% of triolein which can also be used as a substrate, while an amperometric sensor has been reported that uses glycerol dehydro-genase/NADH oxidase. Pancreatic  $\alpha$ -amylase cleaves at alpha-bonds of large polysaccharide chains to produce mono- and disaccharides glucose and maltose, respectively [7]. Therefore, glycogen or starch in

various forms such as amylose or amylopectin are used as substrates in assays or in biosensors for determining amylase activity, which can potentially enable the detection of amylase using pre-existing redox sensors using such materials [75], [76].

The resulting hydrolytic events induce structural changes that can be sensed with a variety of transduction methods, such as electrochemical, piezoelectric, optical, thermoelectrical, or photosensitive, among others [77]. Several studies use a quartz crystal microbalance (QCM) to sense changes in crystal resonant frequency as the substrate is degraded in response to varying concentrations of the enzymes mentioned above [72], [76], [78]. These studies consisted of depositing films of the biomaterials on the sensor surface, and in some instances, would be embedded with nanoparticles or chemical cross-links to enhance sensitivity or decrease non-specific binding, respectively. In other sensors, these films can act as insulators, coating surfaces and changing their electronic characteristics, such as conductivity or dielectric permittivity, depending on the material. For example, a pH sensor exists that uses a hydrogel copolymer film deposited over interdigitated electrodes (IDEs), and the film's water content changes depending on the presence of acids or bases, resulting in a pH-dependent level of hydrogel swelling and ultimately measured by the change in electrode surface conductivity [79]. By exploiting these material properties, it is possible to design sensors with signal outputs that change proportionally to the environment and specifically to a target of interest [80]. On that note, biomaterials-based films can act as enzyme-specific degradable substrates, which I leveraged when deposited over our system's capacitive sensors [72], [73], [76], [78]. Because the GI

tract is a host to numerous hydrolytic enzymes, many of which are summarized in Table 1-1, monitoring them *in situ* would likely offer pathologically relevant information.

Table 1-1 Major gastrointestinal enzymes, organized by source and excluding the salivary glands and large intestine, and some of their respective associated health conditions.

Source	Enzyme	Substrate	Conditions
Stomach	Pepsin	Proteins	Carcinoma, pernicious anemia, post-operative peptic and duodenal ulcers [81]
	Lipase	Triglycerides	Pancreatic dysfunction, cystic fibrosis [81]
Pancreas	Amylase	Starch	Pancreatitis (Acute/Chronic), Adenocarcinoma, Pancreatic insufficiency [1], [2], [65], [82]
	Lipase	Triglycerides	
	Proteases (Trypsin, Chymotrypsin)	Peptides	
	Elastase	Elastin	
	Nucleases	Nucleic Acids	
	Phospholipase	Phospholipids	Adenocarcinoma [83]–[85]
	Carboxypeptidase	Protein terminal amino acid	
Small Intestine	Enterokinase	Trypsinogen, Chymotrypsinogen	Mucosal villous atrophy, Hypoproteinemia, Pancreatic Insufficiency, Carcinoma [86], [87]
	Maltase	Maltose	Mucosal villous atrophy, Coeliac's Disease [87], [88], Lactose Intolerance, Intestinal hypermotility, Diarrhea, Inflammatory bowel disease [89], [90], Sprue [91]
	Lactase	Lactose	
	Sucrase	Sucrose	

The above enzymes, it is worth noting, are those present in higher concentrations in the GI environment and critical to homeostatic physiological function. As mentioned in the previous section, other enzymes have been isolated from pancreatic secretions that become present in pathological conditions such as pancreatic cancer. One example is matrix metalloproteinase (MMP), or matrixin, which is a type of protease that can be subdivided into more than 20 different forms [92]. Specifically, MMP-9, or gelatinase B, has been present in both serum and pancreatic juices, and aids

in differentiating patients with pancreatic ductal adenocarcinoma, the most common form of pancreatic cancer, from those with chronic pancreatitis [56], [93]. MMP-9 explicitly hydrolyzes peptide sequences with Pro-X-X-Hy-(Ser/Thr) motifs at P<sub>3</sub> through P<sub>2</sub> positions, so it is possible to design hydrolytic substrates that would react similarly to the aforementioned materials [93]. One example has been demonstrated by Biela et al., where the peptide has been used to crosslink Dextran films, and the degradation was monitored via EIS [94]. Their hydrogel fabrication process, which could be utilized for other peptide-hydrogel-crosslinking mechanisms, is illustrated in Figure 1-7 below. While the process for forming peptide-crosslinked hydrogels has been previously demonstrated, the above work showcases a use-case with a clinical target. Using EIS or other electronics sensing methods like those discussed in Section 1.3.1, such film-based platforms have the potential for integration with microelectronics that be implemented in capsule devices for measuring these targets in the GI tract.

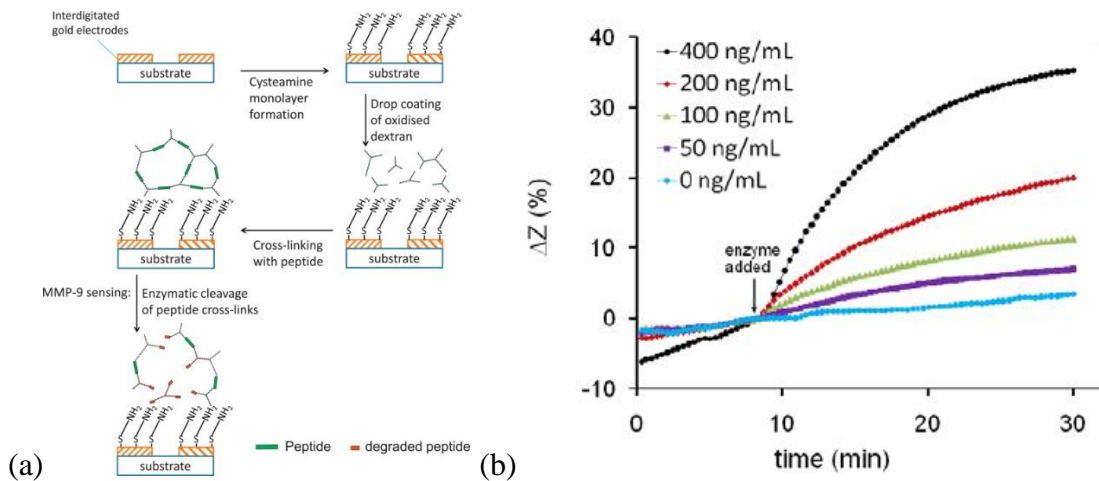


Figure 1-7 (a) Process for fabricating peptide-crosslinked hydrogels over gold IDE sensors, specifically for sensing MMP-9 with EIS, and (b) 10 Hz impedance response of resulting sensor to different MMP-9 concentrations. Reproduced with permission from [95].

#### 1.3.4 Integrated *In situ* Capsule Technology

This section introduces the system-based solution that is pursued in this dissertation. Integrated systems embedded with automated micro- and nanotechnologies are gaining momentum as revolutionary methods in biomedical applications for replacing cumbersome or complex processes. Many of these systems, like most automated technology, require a combination of sensors or various electronic components, as well as some form of interface with human physiology to achieve a designated purpose.

Several such devices, depicted in Figure 1-8, are continuously under development for vastly different applications, and are ubiquitous both in industrial and academic settings. One of the most successful commercially available examples is the capsule endoscope, such as the PillCam by Medtronic, introduced as an alternative to endoscopic procedures in the GI tract such as a colonoscopy or EGD [10]. Capsule endoscopes are essentially pill-shaped devices containing a camera that, upon ingestion, allows for tetherless video streaming and recording of the GI tract to locate abnormalities such as ulcers, sources of bleeding, polyps, or tumors. While there is also an associated non-trivial risk of bowel obstruction, the primary benefit is that it is able not only to reach areas that exceed the range of other procedures, but it also does not require anesthesia or as much physician involvement [96].

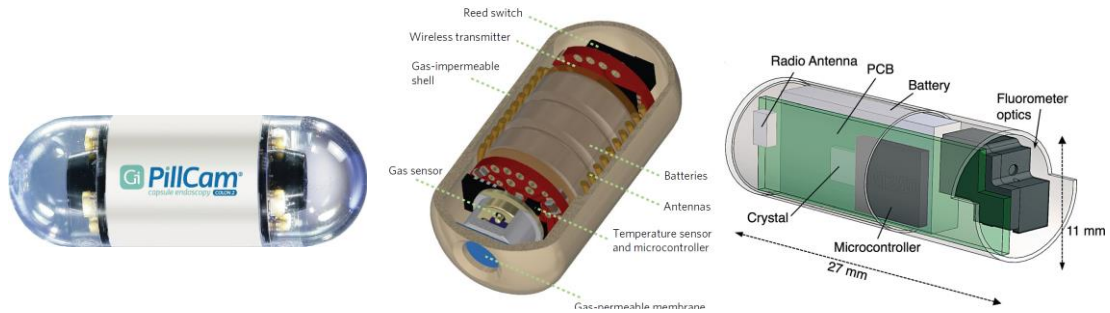


Figure 1-8 Examples of integrated capsule systems. From left to right: PillCam COLON 2, GI gas sensor, and GI bleeding monitor. Reproduced with permission from [97]–[99].

Additional examples in academia use specific sensing mechanisms when the target becomes more complex. One device exists for measuring gas concentrations in the gut [100]. Here,  $\text{CO}_2$ ,  $\text{H}_2$ , and  $\text{CH}_4$  are measured with electrochemical sensors at various sampling sites through the stomach, small intestine, cecum, and colon, and are measured in response to controlled diets based on fiber content. Though electrochemical gas sensors have been around since the 19th century, the novelty lies primarily with the integration of this sensor into an ingestible system [101]. This becomes compounded by evidence suggesting gas composition throughout the GI tract changes in various pathological conditions, thereby offering potential for clinical evaluation. Another device uses fluorescence imaging to determine the occurrence of GI bleeding [99]. By injecting fluorescein into the bloodstream, the marker naturally makes its way into the GI tract, where a capsule housing a fluorimeter detects and wirelessly transmits data to an external monitoring unit. This device serves to enhance traditional endoscope procedures for real-time monitoring, and is also more specific than using capsule endoscopy as discussed above.

Though there are additional similar devices that warrant discussion, a prevalent theme is the integration of multiple modules. The modules included often consist of a

sensor, microcontroller, signal transceiver, power supply and management electronics, and a capsule-like package, enabling the development of devices capable of targeted, real-time sensing with wireless signal transmission. A brief list of recent state-of-the-art capsule devices are presented in Table 1-2.

Table 1-2 Integrated capsule systems. From left to right: PillCam COLON 2, GI gas sensor, and GI bleeding monitor.

Product/ Application	Transducer/Target	Communication	Power	Manufacturer/ Reference
Gas Sensing	Electrochemical/ CO <sub>2</sub> , O <sub>2</sub> , H <sub>2</sub> , CH <sub>4</sub>	433 MHz	Silver Oxide	[12], [13], [100]
PillCam/ MiroCam/ Endocapsule	Optical	434 MHz/ 430 MHz/ 434 MHz	Lithium Ion	Medtronic/ IntroMedic Co./ Olympus
GI Bleeding	Photodetectors/ Fluorescein	2.4 GHz (Zigbee)	Lithium polymer	[99]
GI Bleeding	Photodetectors/ Bacterial light	433 MHz	Lithium Manganese	[102]
GI Electrochemical Signatures	Electrochemical	433 MHz	Lithium Manganese Dioxide	[103]
pH/ Temperature/ Pressure	Capacitive/ Resistive	434 MHz	Silver Oxide	[104]

The above devices are but a short list of the emerging technologies in the ingestible capsule domain, and are representative of the open-ended nature of integrated capsule system development. Though the most consistent feature is the ISM band of radiofrequency (RF) communication for wireless signal transmission (433-434 MHz), the transducers and applications vary significantly and each require their own signal-conversion circuit to be compatible with the microcontroller capable of tasks such as (a) generating an input signal at programmable intervals, (b) signal processing, and (c) enabling feedback control for modulating power or signal characteristics,

among others. One aspect of note with Table 1-2 is that the optical capsules are the only ones listed with manufacturers. Though there are additional capsules on the market for sensing features such as temperature or pressure, those used for capsule endoscopy remain the most mature and popular for commercial development and therefore medical diagnostics.

In terms of power supply, or battery, each capsule must identify the most appropriate option to ensure the on-system electronics can maintain individual modular functions. First and foremost, batteries must operate over the time intervals required, which is often throughout the entirety of the GI tract and can average at 34 hours with a range of 8-57 hours [105]. This is generally easier for systems designated to operate for shorter time durations, i.e. when localized to specific organs or organ transitions. However, this is critically dependent on the electronics of the system for achieving its respective function. Each option in Table 1-2 is adequate for the devices presented, while there is likely room for optimization through considerations such as data compression (of the transmitted signal) or power-saving algorithms that alter the power modes of each module; for example, some IC components can operate between modes such as “Active” or “Deep Sleep” (specifically for the MCU discussed in Chapter 3), which correspond to current consumption when wireless functions are triggered or delayed, respectively. In capsule endoscopy, for example, power consumption of the signal transmitters has evolved with each iteration, ranging between 2-7 mW, and is detailed further in other works and for other types of ingestible devices [106]–[108].

One of the most important features of these devices is the packaging, which upon observation appears relatively consistent and is the only barrier between the

internal system and the external environment. The primary metric the design packaging must achieve is safety for both the GI environment, i.e. the tissue, fluids, etc., and for the internal components. The former is dictated by the shape, dimension, materials, and sealing capability of the device shell. The shape is almost always a capsule, where the length in one axis is longer than the length of the other, or the width, and the ends of the shell on the longer axis are rounded [109]. Work from Baek et al. investigated the effect of structural features such as geometry, length, and diameter on capsule friction, producing downstream expectations on how it would impact GI transit [110]. Though capsules have long been a standard for ingestible technology in the area of pharmaceuticals, their findings yielded adequate rationale to appreciate the impact of this seemingly trivial feature. Furthermore, the ability to control transit time poses significant utility for additional applications. For example, in the event that a device would be required to remain in a specific GI region for a longer time scale, one could use geometric innovation such as a greater surface area at the micro- and nanoscale to increase frictional forces. While such strategies may augment additional complications such as biofouling or potential trauma to GI mucosa if large enough to create perforations, it adds further consideration to ingestible capsule design [110]–[114].

In terms of materials, the most common requirement is biocompatibility. Though biocompatibility can still entail a wide range of properties, the most popular use in this context is for the material to be tested as a “surface device that contacts breached or compromised surfaces for prolonged contact”, according to the Food and Drug Administration (FDA)-modified ISO-10993 [115]. This would entail testing such as cytotoxicity, sensitization, irritation or intracutaneous reactivity, acute systemic

toxicity, material-mediated pyrogenicity, subacute/subchronic toxicity, and implantation, as outlined in Table A.1: Biocompatibility Evaluation Endpoints [115]. The effects prove challenging to enable efficient control due to the heterogeneity of GI fluids, even without considerations for variation in diet. For example, the pH of the GI tract can range from  $<1$  (highly acidic) to  $>7$  (neutral, slightly basic), imbuing a requirement with a significant impact because (1) this comprises approximately half the pH range in our general chemical understanding and (2) this limits the number of materials that would not react with such pH levels. This is compounded by numerous other species in GI fluids likely to induce any number of physicochemical interactions with the capsule package, such as proteins (enzymes, glycoproteins, etc.), hormones, ions, etc. [116].

The materials must also withstand mechanical forces occurring during peristalsis, which can vary depending on the region of the GI tract. In the small intestine, the primary forces acting on devices in transit are traction force, contact force, and peristaltic waves [117], [118]. Forces are slightly different in the stomach, where tonic contractions and peristaltic waves dominate the mechanical impact on materials to induce movement toward the pyloric sphincter; these forces were also investigated using pills with embedded pressure sensor arrays [119], [120]. For the above capsules, cladding and sealing materials vary where mentioned. Arefin et al. only discusses having used corning sealant while using a 3D printed cladding to surround their system [121]. The work by Mimee et al. uses PDMS as their sealing material without any cladding material [102], and the capsule for GI bleeding uses a machined cylinder made of acetal resin, specifically Delrin (DuPont, DE). The optical capsules generally use a

variety of biocompatible plastics such as polycarbonate, polyurethane, or nylon due to their resistance to gastric acids [122], [123]. Chapter 3 will revisit the concept of capsule packaging, including the materials I utilized for enhanced utility for both protecting our system and targeting our GI region of interest.

#### 1.4 Structure of Dissertation

Chapter 1 introduced the reader to the motivation and background required to appreciate the impact of this dissertation, ranging from the rationale of our sensor and system design to the requirements for the downstream development of a platform adaptable to a variety of healthcare diagnostics. Chapter 2 delves into the intricacies of impedance sensing and its utility for garnering detailed information on surface-interacting hydrolytic reaction mechanisms. Chapter 3 presents our packaging-focused approach in hybridizing 3D-printing and pharmaceutical polymer coatings into a cohesive manufacturing strategy. Chapter 4 discusses the challenges associated with assembling, testing, and validating our system, while demonstrating its versatility for sensing multiple duodenal biomarkers. Finally, Chapter 5 summarizes the contributions of the work while introducing various directions for expanding device utility.

## 2. Chapter 2: Electrical Transduction of Pancreatic Trypsin Activity

### 2.1 Pancreatic Enzyme Sensing

As discussed in Table 1-1, GI enzymes can be categorized by their region of origin, substrate, and associated pathologies. Their quantification is traditionally performed through assays, including various forms of enzyme-linked immunosorbent assays (ELISA), with a range of methodologies including colorimetric, radioimmuno, and immunochemiluminometric. What remains consistent among each of them is the requirement of transducers to convert the biological signal, i.e. the enzyme concentration or activity, to a measurable signal for analysis in electronic systems. As discussed in Section 1.3.1, electrical biosensing techniques leverage direct changes in electrical properties of the substrate and biomarker-substrate interface, while achieving inherently more simplicity than those discussed above [124]. Such direct measurements can be useful not only for detecting the biomarker of interest, but determining qualitative or mechanistic details on how the sensor materials behave in response to their activity; this can aid further in improving sensor designs or optimizing materials. Here, I describe efforts to observe changes in electrical characteristics of substrate films after exposure to hydrolytic enzymes.

Pancreatic enzymes, including trypsin, lipase, and amylase, are excellent model biomarkers to assess GI health and proper pancreatic function. Pancreatic trypsin, in particular, is a protease essential to a functional digestive system, allowing for the breakdown of various proteins to enable nutritional absorption in the small intestine. It is secreted as the proenzyme trypsinogen by acinar cells, where it travels through the

pancreatic duct into the duodenum and becomes activated upon hydrolysis by enterokinase on the lumen surface [7]. Lipase and  $\alpha$ -amylase are among the other major enzymes that are activated in the duodenum. These enzymes enter the duodenum in a basic solution with the intent to neutralize the gastric acid entering from the stomach. In various types of pancreatic pathologies, such as chronic pancreatitis or pancreatic adenocarcinoma, trypsin activity has been shown to decrease, indicating the acinus or duct has been compromised in some way [1], [125], [126].

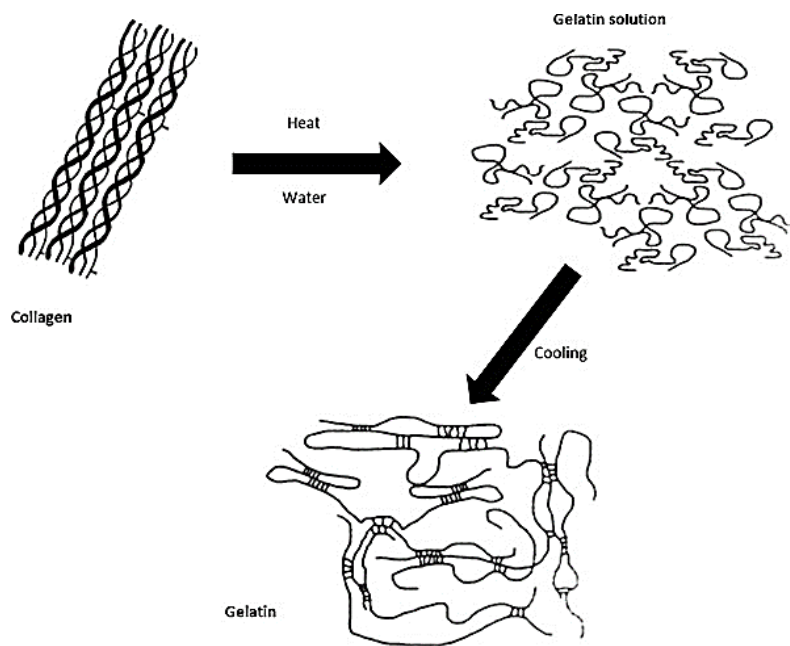


Figure 2-1 Schematic of collagen denaturation into gelatin. Reproduced with permission from [127].

Recent techniques for sensing trypsin involve analyzing substrate degradation in response to enzymolysis, described in Section 1.3.3. Trypsin hydrolyzes specific peptide bonds present on substrates with amino acids lysine and arginine. The substrates include cytochrome c, gelatin, albumin or poly-L-lysine, while transduction methods are equally variable, using either optical, fluorescence, ionic conductance, or resistance [71], [73], [128]–[130]. Because of its versatility for processing and

modification, including over other electrode systems, gelatin was investigated as a model substrate for this work [131], [132]. Gelatin is a hydrolytic product of collagen, and the 10%–20% of most final gelatin forms consist of the amino acids mentioned above [133]. Gelatin is also biocompatible, and therefore an attractive substrate material for trypsin. As a hydrogel that begins as a low viscosity liquid when heated, it can be formed to a variety of structures that are limited only by the tools used until it cools and transitions from sol to gel state, the process for which is depicted in Figure 2-1.

One such structure is a thin film, compatible for various impedimetric or amperometric sensors made from standard monolithic fabrication. Thin film structures have been achieved through deposition of hydrogel, while in the sol state, using strategies such as spin-coating, drop-casting, dip-coating, etc. [134]. Furthermore, crosslinking is utilized often to enhance the stability of the material, and is limited by the reactive functional groups in the structure's chemistry [135]. Glutaraldehyde, for example, has been used to allow for gelatin films to maintain structural integrity at higher temperatures – i.e. the physiological temperatures present throughout the GI tract (37-39°C) – to ensure the film remains stable, though high concentrations can induce toxic effects on cells [136], [137].

It is important here to introduce several distinctions between the sensors intended for the system in this thesis, i.e. *in vivo* in the GI tract, and how most biochemical sensors for biomedical applications operate. Firstly, *in vitro* systems are often not concerned with toxicity as they are often utilized *in vitro*, where the samples are either in buffer or fluids that have been removed from the cellular contact. This

does not apply to the few sensing strategies that are designed to operate *in vivo*, as there are significant risks associated when implementing foreign objects in the physiological environment due to the potential for an immune response with the complex biochemical heterogeneity [138]. This introduces another distinction, which is that *in vivo* sensing has limited capabilities regarding sample pretreatment without additional system modules, and thus the sensor is subject to interact with each molecule – including those that are not of interest and therefore nonspecific – present in the fluid. Therefore, when targeting trypsin, which, as discussed above, originates near the duodenum, it is critical to test the sensor with fluids exhibiting similar heterogeneity to thus reduce unprecedented signals resulting from these nonspecific interactions.

Through our use of gelatin, there are various potential nonspecific interactions at risk. For example, though none of the species are likely to react with the substrate via hydrolysis – except for chymotrypsin, as discussed in Section 1.3.3 – other interactions may occur such as ionic or molecular diffusion into the film or aggregation at the film surface. Diffusion often occurs for species with sizes smaller than the hydrogel film mesh, which can be mitigated through tighter crosslinking through techniques discussed above. Aggregation, on the other hand, can occur when the species are larger than the mesh or are immobilized via nonspecific binding at the film surface [139]. Both can yield distinct sensor responses, depending on the transducer used, though I focused in this work on testing several species that fit into the latter category.

In this chapter, I discuss our efforts for developing a sensing strategy for measuring trypsin activity in solutions containing several types of interfering enzymes

characteristic of duodenal fluid. Crosslinked gelatin films were formed over interdigitated finger electrode (IDE) sensors, which were fabricated similarly to those described previously [140]–[142]. These sensors were inserted into fluidic chambers and exposed to various pancreatic enzymes while changes in the mass and impedance responses were recorded. Ultimately, it was possible to differentiate the presence of trypsin and provide insight as to its role in producing complex impedimetric signals, offering potential for utilizing this method for *in situ* sampling.

Dr. Luke Beardslee contributed to fluidic setup design and sensor process development. Dr. Young Wook Kim contributed to initial sensor design in Appendix A.1. Dr. Sowmya Subramanian and Dr. Thomas Winkler contributed respectively to initial data extraction (Appendix C of [143]) and analysis of impedance results. This work was published in contribution to [144].

## 2.2 System Design and Experimental Setup

### 2.2.1 IDE Sensor Fabrication and Film Deposition

A simplified schematic of the sensor fabrication process is depicted in Figure 2-2a. A pair of sensor electrodes per device (Appendix A.1), one sensor with substrate polymer coating and one for negative control (footprint 3 cm × 1 cm), was obtained using a standard photolithography process for NR9-1500PY photoresist (Futurrex, Inc., Franklin, NJ) over 100 mm pyrex wafers. This involved a 5-minute dehydration period, spin-coating at 3000 RPM for 30 seconds, a 150°C soft bake for 1 minute, exposure to 365 nm UV 190 mJ/cm<sup>2</sup>, a 100°C hard bake for 1 minute, development in RD6 for 10–12 seconds, then rinsing in DI water. Cr/Au (20 nm/200 nm) was deposited via E-beam

evaporation(Angstrom Engineering, Ontario, Canada), followed by liftoff with acetone for 5 minutes. The resulting IDE fingers, a total of 146, were 2  $\mu\text{m}$  wide with 4  $\mu\text{m}$  spacing and 960  $\mu\text{m}$  in length, as shown in Figure 2-2b.

Next, a 75  $\mu\text{m}$  thick polyvinyl chloride (PVC) film (Semiconductor Equipment Corp, Moorpark, CA, USA) was applied to the wafer surface, and patterns were manually cut over one sensor per device as a mask for the gelatin film. Gelatin type B solution (from bovine skin, Sigma Aldrich, St. Louis, MO, USA) was added to 50  $^{\circ}\text{C}$  deionized (DI) water while stirring until complete dissolution to a final 5 %w/v. 200  $\mu\text{L}$  gelatin solution was spin-coated at 400 rpm for 30 s over the sensors, then cooled overnight into a gel state over the test sensor. All gelatin films were crosslinked after overnight cooling with 0.5% glutaraldehyde solution in DI water at room temperature for at least 4 hours to improve thermal stability. After PVC removal from the IDE patterned wafer, gelatin film thicknesses were characterized, or profiled, with a contact profilometer (Veeco, Dektak-8 stylus, Plainview, NY, USA) which were found ranging between 400–700 nm. IDE devices were then diced using a standard dicing saw (Microautomation, Centreville, VA, USA), rinsed with DI water, and dried overnight.

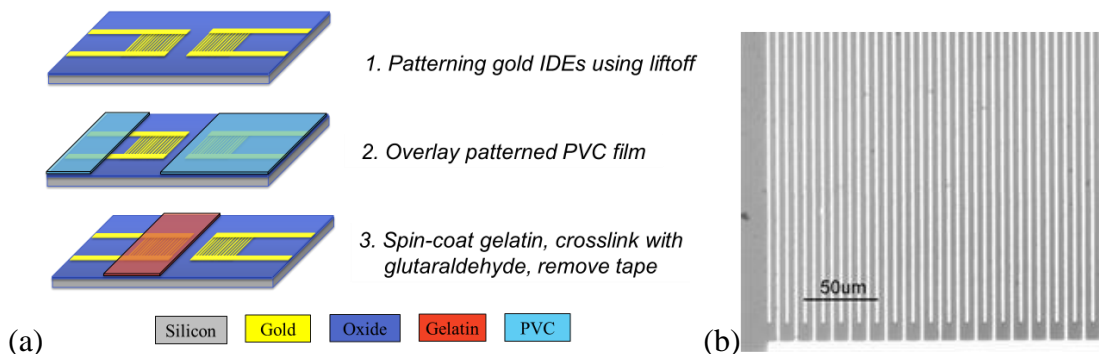


Figure 2-2 (a) Schematic of sensor fabrication. Step 1 entailed photolithography and E-beam deposition of Cr/Au for 20nm/200nm, then liftoff with acetone. After overlaying a 75  $\mu\text{m}$  thick PVC film, 5% gelatin in buffer was spin-coated at 400 rpm for 30 sec, cooled overnight, then crosslinked with 0.5% glutaraldehyde solution to improve thermal stability. After PVC removal, gelatin was measured using a contact profilometer at thicknesses of 300-700 nm. (b) Microscopic image of the resulting sensors.

### 2.2.2 Enzyme Solution Preparation

Trypsin from bovine pancreas ( $\geq 7500$  benzoyl-L-arginine ethyl ester units/mg solid, 23.8 kDa),  $\alpha$ -Amylase ( $\geq 10$  units/mg solid, 51–54 kDa) and lipase (Type II, 100–500 units/mg protein, 48 kDa) from porcine pancreas, as well as phosphate-buffered saline (PBS) capsules were obtained from Sigma Aldrich. 0.1 M PBS (pH 7.4) was used in each experiment. Enzymes were mixed and incubated in PBS for at least 15 min at 37 °C before use. Trypsin solutions of either 1 or 0.5 mg/mL were used, while lipase and  $\alpha$ -amylase were prepared at 1 mg/mL each. Heterogeneous solutions consisted of 1 mg/mL of each enzyme.

### 2.2.3 Impedance Sensing

To test the sensors with continuous enzymes, a fluidic chamber was designed, depicted in Figure 2-3, that enabled electrical connections with the sensor contact pads. Diced IDE sensors were inserted into a custom two-piece 3D printed chambers containing an inlet and outlet for respective solution entry and removal from the chamber via continuous flow. The parts were designed in SolidWorks (Dassault Systemes, Vélizy-Villacoublay, France) and 3D printed from MED610 with an Objet30 Pro (Stratasys, Eden Prairie, MN, USA). Fluid was injected with syringe pumps at 20  $\mu\text{L}/\text{min}$  through 0.4/2.24 mm inner/outer diameter tygon tubing (Cole-Parmer, Vernon Hills, IL, USA) into the chamber inlet, then exited through the outlet into a waste beaker. Sensor response was recorded with each medium until the signal saturated at a constant magnitude, beginning with air, PBS (negative control), then PBS with enzymes, described in Section 2.2.2. The chamber was incubated at  $\sim 37$  °C for each experiment to simulate physiological temperature. IDE contact pads were connected to

a CHI 660D Electrochemical workstation (CH Instruments, Bee Cave, TX, USA), one pad connected to the working terminal and the other pad to shorted reference and counter terminals. The frequency was swept from 10 Hz—1 MHz at an AC voltage amplitude of 50 mV for two minutes per sensor. Sensor substrates were weighed with a Sartorius ME-5 microbalance (Sartorius, Goettingen, Germany) and profiled, through the process described in Section 2.2.1, at three separate time-points: (1) before deposition, (2) once the films were dehydrated, and (3) following experimentation to correspond absolute change of film mass and thickness with the resulting changes in impedance.

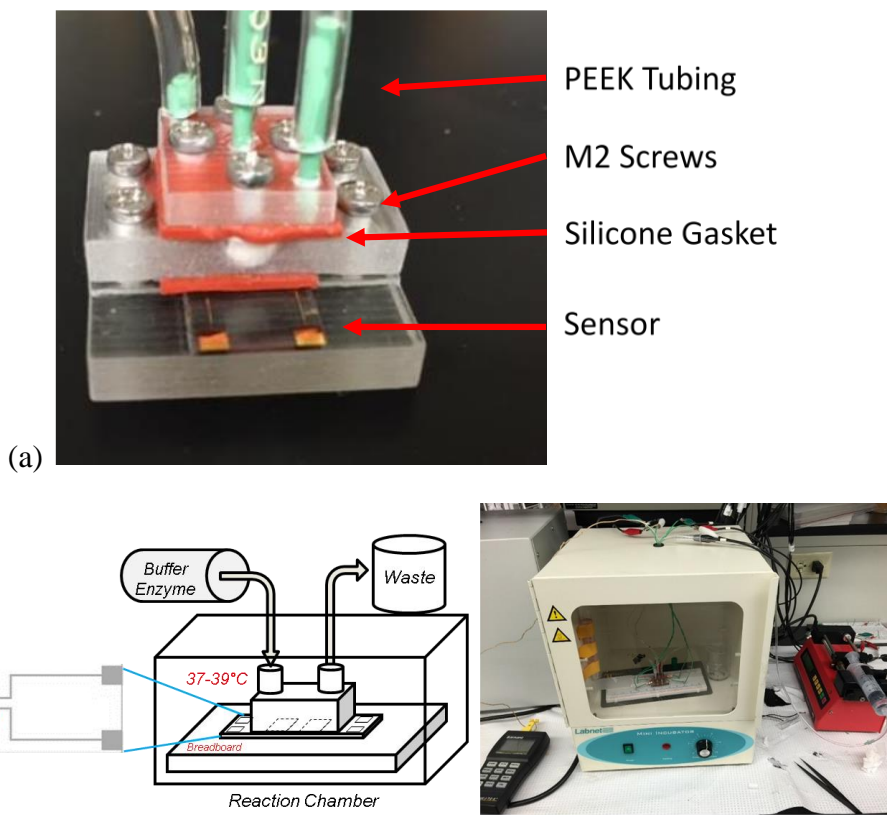


Figure 2-3 (a) Fluidic reaction chamber for testing sensors with enzyme solutions. (b) Schematic of the film-coated sensor and experimental chamber (left). Photograph of Experimental setup (right).

#### 2.2.4 QCM Sensing Methodology

As a means of measuring activity in real time between the enzymes discussed above and the gelatin films, I investigated mass sensing using quartz crystal microbalance (QCM) (Inficon, East Syracuse, NY, USA). Fluid was injected with syringe pumps at 20  $\mu\text{L}/\text{min}$  through tygon tubing (Cole-Parmer) into the QCM Teflon® 100  $\mu\text{L}$  chamber inlet, then exited through the outlet into a waste beaker. Sensor response was recorded with each medium until signal saturation, beginning with air, PBS (negative control), then PBS with enzymes, described in Section 2.2.2. The chamber was incubated at  $\sim 37^\circ\text{C}$  for every experiment to simulate physiological temperature. QCM substrates were cleaned before deposition and after experimentation with 3:1 Piranha solution. They were also weighed with a microbalance and profiled as described in Section 2.2.1.

#### 2.2.5 Image/Data Analysis

Drop-cast deposited and crosslinked over each dye, with one of the two sensors consistently covered with PVC. This process was done carefully to cover only one of the sensors on the device as to maintain the presence of a control sensor. The resulting films possessed thicknesses ranging from 60–90  $\mu\text{m}$  (Veeco). Films were observed and analyzed using an INM100 Microscope (Leica, Wetzlar, Germany) and an S-3400 Variable Pressure Scanning Electron Microscope (SEM) (Hitachi, Tokyo, Japan). Impedance data were exported from CHI software as .txt files, and imported, along with film thickness profiles, into MATLAB (MathWorks, Natick, MA, USA) for analysis. Nyquist and Bode spectra were observed, and impedance at various frequencies were plotted over time for each condition.

## 2.3 Results and Discussion

### 2.3.1 Film Structure and Morphology

Microscopic images of resulting IDE sensors, with and without spin-coated gelatin films before exposure to enzyme solutions, are displayed in Figure 2-4a. The gelatin films, depicted over the sensors on the left side of the image, were slightly frayed at the edges after removal of the PVC tape; however, this was not found to directly affect sensor response as the edges were further than a finger width distance from the IDEs. Figure 2-4b–d represent the dried sensor after exposure to either PBS (b), trypsin (c), or a combination of trypsin, lipase, and amylase (d) in PBS. After surface profiling, it was evident that trypsin alone removes the most gelatin from the sensor surface, visualized in Figure 2-4c, while each other condition leaves a residue of film over the test sensor and more non-specific adhesion of other enzymes to the control surface, such as the mixture-treated sensors depicted in Figure 2-4d. Table 2-1 describes the mean proportion of remaining film thickness after exposure to each solution condition, calculated using equation (3), where  $t$  is the thickness at each measurement point explained above:

$$\text{Film Thickness Remaining} = \left( \frac{t_{pre} - t_{post}}{t_{pre}} \right) \quad (3)$$

A value of 1 indicated zero film loss, and each thickness was achieved after signal saturation and complete drying of the sample in an ambient environment.

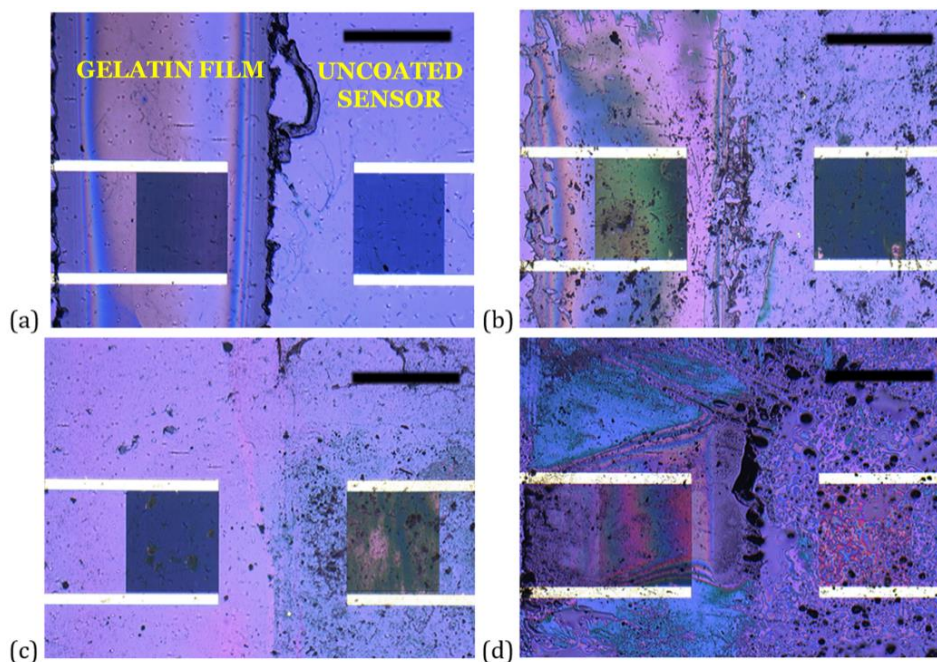


Figure 2-4 Resulting interdigitated finger electrode (IDE) sensors, with (Left) and without (Right) gelatin films, (a) pre-exposure to solutions, and post-exposure to (b) buffer; (c) trypsin; or (d) all three enzymes in buffer. Scale bar = 1 mm.

Table 2-1 Ratio of spin-coated film remaining after various enzyme conditions, analyzed with a contact profiler (n = 2).

Condition	Film Thickness Remaining (%)
PBS (Phosphate Buffered Saline)	78.6 ± 0.05
Amylase (1 mg/mL)	24.3 ± 0.08
Lipase (1 mg/mL)	52.4 ± 0.30
Trypsin (1 mg/mL)	11.1 ± 0.03
Trypsin (0.5 mg/mL)	21.7 ± 0.10

Scanning electron microscope (SEM) images of the drop-cast films in various conditions can be viewed in Figure 2-5, where (a-b) are side-view and (c-d) are top-down. In Figure 2-5a, the dry, cross-linked films resulted in an edge thickness of ~60  $\mu\text{m}$ . After exposure to trypsin for several hours, at which the absolute impedance had saturated, the sensor was rinsed with DIH<sub>2</sub>O and completely dried. The resulting edge thickness, depicted in Figure 2-5b, was then measured at ~9  $\mu\text{m}$ , reflecting the removal of film as a result of hydrolysis from trypsin. The ratio of remaining to original film

thickness was slightly less than 0.15, which is relatively consistent with the ratio of film remaining with the spin-coated film from Table 2-1 (0.11). Furthermore, the film is much smoother, and can be observed again from the top view in Figure 2-5c.

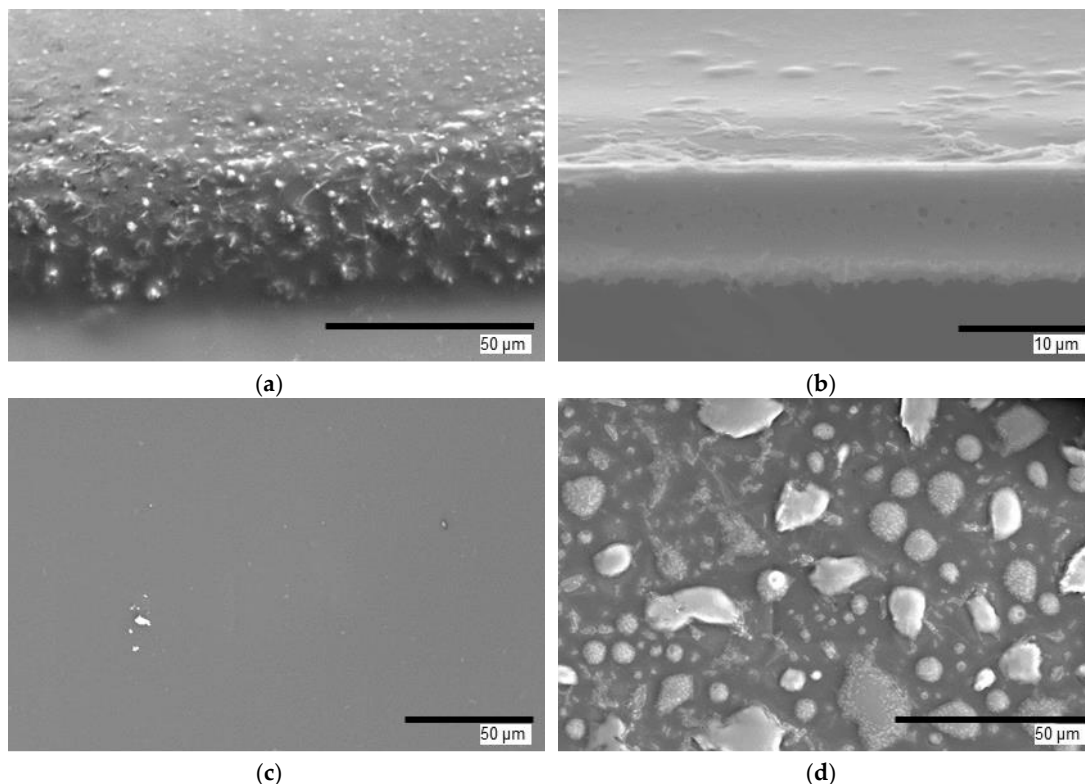


Figure 2-5 Representative SEM images of drop-cast, crosslinked gelatin films. Edge views of film (a) without exposure to enzyme solutions and (b) after exposure to trypsin, and top views of film (c) after exposure to trypsin and (d) after exposure to all three enzymes in buffer.

After the drop-cast film was exposed to a combination of all three enzymes, the thickness reduced to only  $\sim 0.68$  of the original film after the impedance signal had saturated. This indicates saturation occurred before even half of the film had been degraded. Further, as depicted in Figure 2-5d, globules form in the film, some of which can exceed  $15 \mu\text{m}$  in diameter. This is likely due to the entrapment of non-specific enzymes in the gelatin matrix, potentially responsible for attenuating the trypsin activity [145]–[147]. Further, the immobilization of the non-specific enzymes in the gelatin may induce tighter bonds (i.e., aldimine with the amylase) to form, possibly

explaining the decrease in thickness[148]. However, based on the results in Table 2-1, there is still less degradation with all three enzymes than what occurs with only amylase or lipase, suggesting enzymatic cross-interference in the solution prior to interactions occurring with the gelatin surface. Due to the prevalence of arginine and lysine in the amino acid compositions of both amylase and lipase, trypsin may be performing additional proteolysis on the nonspecific enzymes in the solution as a result, hence the necessity for further experimentation in the future [149], [150].

### 2.3.2 Impedance Sensing of Trypsin

I characterized the impedance response of gelatin film degradation over IDE sensors in response to various stimuli in a fabricated impedance testing setup made from 3D-printed components, PEEK tubing, and a potentiostat, discussed in Section 2.2.3. Impedance spectra were recorded after film stabilization under PBS flow with the 3D-printed setup in Figure 2-3. The absolute impedance recorded at 10 kHz (indicated later in this chapter in Figure 2-7b) revealed the highest sensitivity to the presence of trypsin during flow due to the largest changes that occurred relative to the initial signal saturation. Figure 2-6 presents impedance spectra comparing the effect of different concentrations of trypsin, which show that 0.5 mg/mL trypsin reduced the film  $\Delta Z$  rate to 0.114 k $\Omega$ /min, a significant drop compared to the 2.88 k $\Omega$ /min rate of the 1 mg/mL concentration. This indicates that the  $\Delta Z$  rate can potentially be used a sensing parameter. The curve for “Trypsin—No Film” essentially represents the impedance of PBS over the sensor since trypsin is not significantly polar and thus does not alter the dielectric properties of the buffer, while “Control—Film” represents the impedance of the film after equilibrating with the PBS.

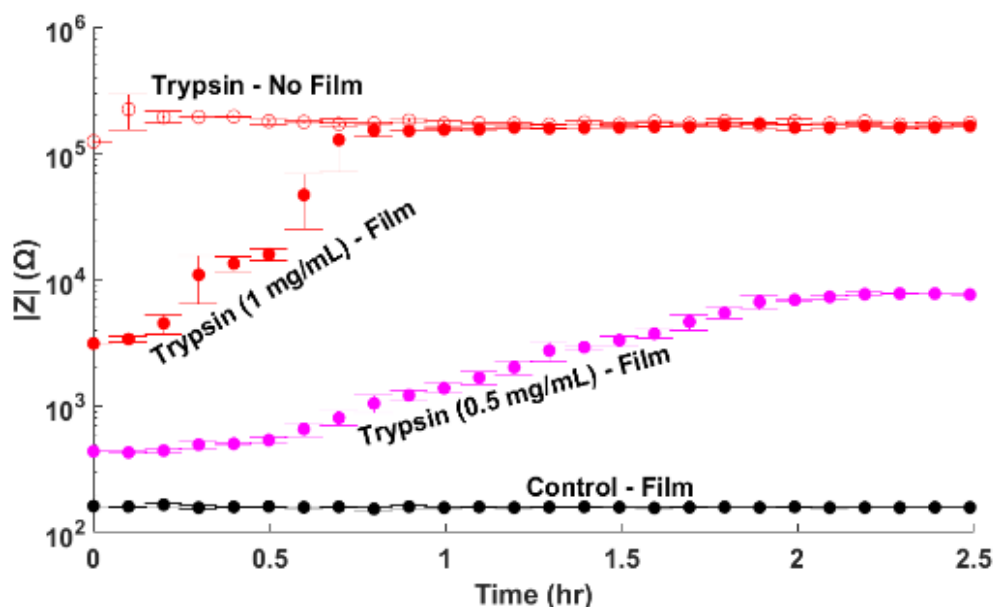


Figure 2-6 Representative impedance responses at 10 kHz of sensors, either uncoated or coated with a gelatin film, to trypsin at 1 (both film and no film), 0.5 (film only) and 0 mg/mL in phosphate-buffered saline (Control). “Trypsin—No Film” represents the impedance of PBS over the sensor, and “Control—Film” represents the impedance of the film after equilibrating with the PBS. The error bars plot the temporal change in impedance at respective time points (temporal span = 3, n=3).

Interestingly, the impedance of the film alone is expected to be higher than that of PBS due to the gelatin’s relatively neutral isoelectric point [151]. It is likely, however, that equilibration with the PBS flow allowed salt ions to accumulate compared to the non-PBS exposed films (data not shown), thereby increasing the ion concentration in the gelatin matrix over the sensor via diffusion.

In Figure 2-7, I report a representative sequence of Bode plots at different exposure times that convey changes in impedance with respect to the equivalent electrical circuit model of the film, such as the double-layer capacitance and solution resistance.

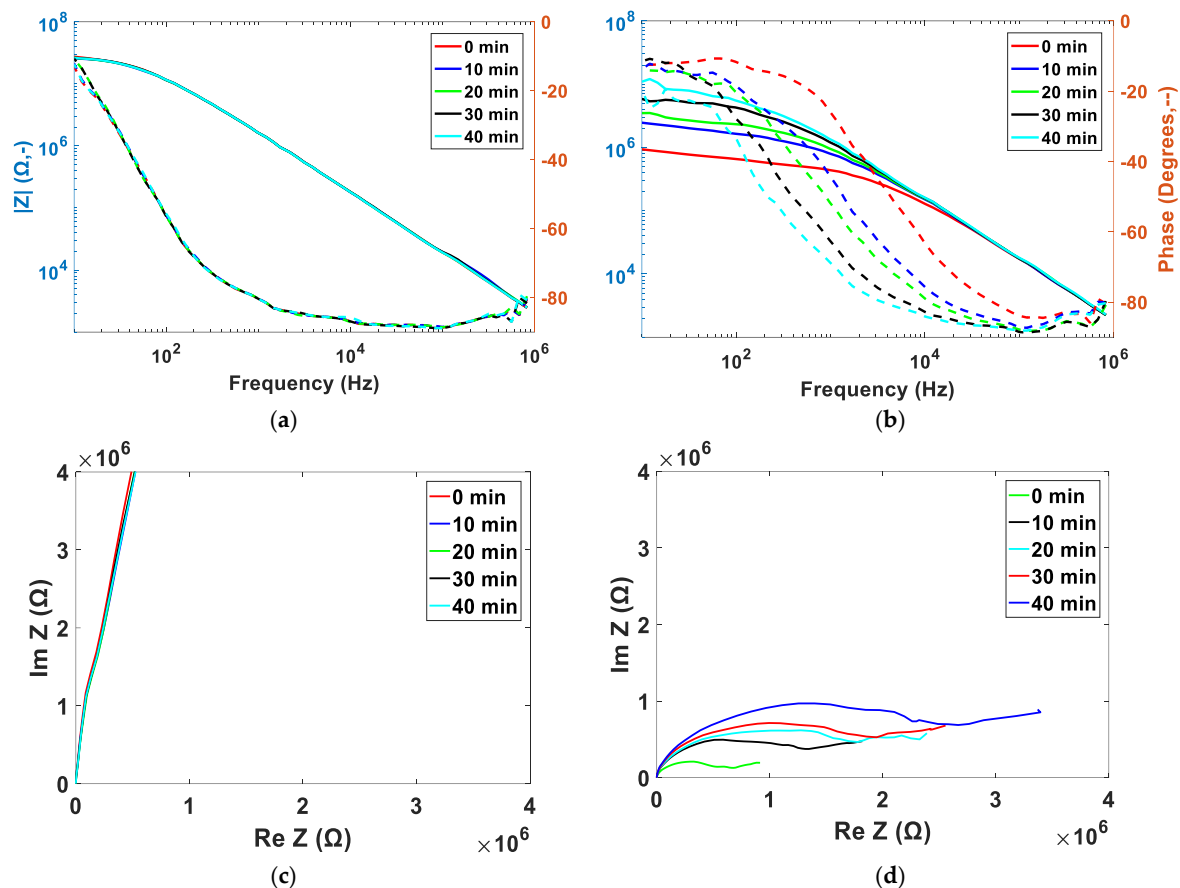


Figure 2-7 Representative Bode and Nyquist plots for progressive exposure of (a-c) uncoated and (b-d) gelatin-coated sensors to 1 mg/mL trypsin in buffer. Continuous (-) and dotted (--) lines indicate  $|Z|$  and the phase, respectively. (n=3).

Here, I observed over time, both the phase and impedance spectra of the coated sensor approaching those of the uncoated sensor, indicating a decrease in film (though it cannot be objectively determined as a decrease in coverage or thickness based on this data) that reflects trypsin degradation of the film due to increased exposure of the sensors to the buffer. I also observed in Figure 2-7b that with increasing frequency the phase approached  $90^\circ$ , further evidence that resistive elements become more negligible compared to capacitive elements in the circuit. Additionally, there is an increase in the solution resistance ( $R_s$ ) in the Nyquist plot, illustrated by the increase in diameter of the semicircles (Figure 2-7d) as trypsin continues to remove film from the sensor surface. This is different compared to what is observed in uncoated sensors (Figure

2-7c), which further supports the likelihood of ion accumulation in the film. Our observations indicate that each of these circuit elements, i.e. resistance and capacitance, can be monitored to determine film degradation, which suggested that I could simplify our electrochemical sensing strategy to measure a specific signal, therefore reducing signal and power requirements to adapt to a smaller electronics system. This first requires investigation as to potential non-specific interactions to determine if they affect either parameter, as well as determine which would be ideal for enhanced sensitivity to the film reactions.

### 2.3.3 Impedance Response with Enzyme Mixture

After characterizing the impact of trypsin on the impedance of the film-coated sensors, I then observed the impact of introducing non-specific enzymes to the solution. In Figure 2-8, I observed that the addition of both amylase and lipase (1 mg/mL each) to trypsin caused a significant decrease in rate of  $\Delta Z$ , measured at  $6.77 \times 10^{-4}$  k $\Omega$ /min compared to 2.88 k $\Omega$ /min for the trypsin only. Further, when amylase or lipase are alone in buffer without trypsin, I observed a decreasing impedance, opposite of the result found with buffers including trypsin. The origin of the increase in impedance during the first hour of the sensors exposed to lipase, as well as within two hours for the amylase, still require investigation, but only seem temporary as the long-term impact of the enzymes yields a decrease in impedance.

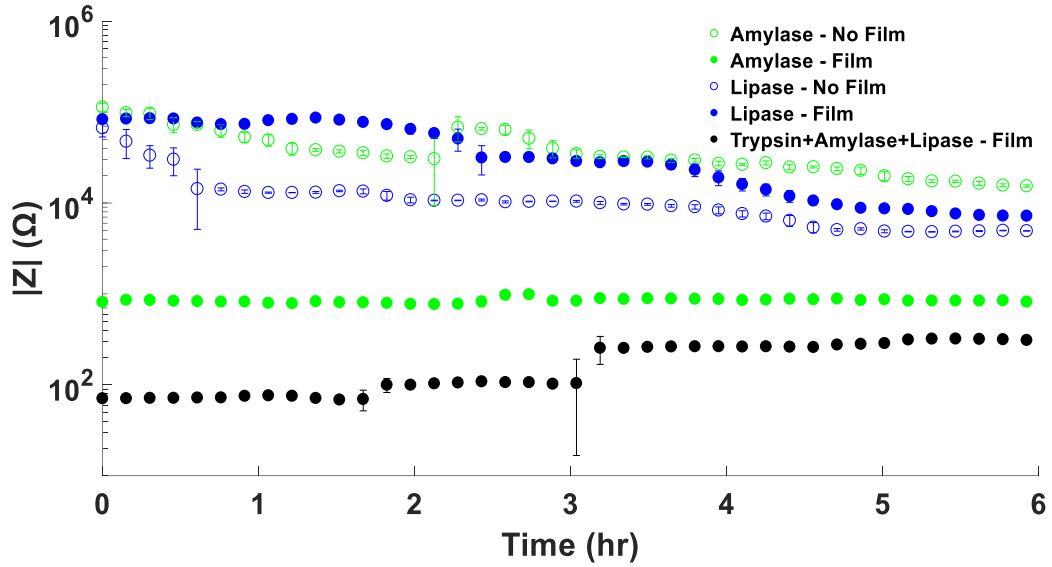


Figure 2-8 Representative impedance responses at 10 kHz of sensors, either uncoated or coated with a gelatin film, to trypsin, amylase, or lipase, each at 1 mg/mL, or combinations of each enzyme with trypsin. The error bars plot the temporal change in impedance at respective time points (temporal span = 3, n=3).

Upon analyzing the Nyquist plots of non-specific enzyme impact in Figure 2-9, I observed additional trends, again different to those from trypsin, induced by the addition of amylase and lipase. These trends include a decrease in the radius of the semicircular region (representative of the  $R_s$ ), the latter of which can be represented by equation (4):

$$R_s = \rho \frac{l}{A} \quad (4)$$

where  $\rho$  is the solution resistivity,  $l$  electrode length,  $A$  is the electrode area [152]. This effect on the  $R_s$  can be a result of the lack of film degradation, or even increase in film thickness [153]. The semi-circular region in the film responding to amylase or lipase is much more defined, indicating a larger double-layer capacitance of the active material i.e. the film and its constituents. This characteristic of the film is also maintained while there is buffer alone, suggesting the non-specific enzymes do not significantly affect the structure of the film in the absence of trypsin (indicated from Figure 2-5d).

Alternatively, in the case of most nonspecific enzymes, residual glutaraldehyde remaining in the film may have allowed for accumulation of additional  $\alpha$ -amylase or lipase, likely observed in Section 2.3.1 [145]–[147]. Upon measuring the film after exposure to all three enzymes, I see the similar trend of increasing impedance as when trypsin is alone, though at a much slower pace. I again observed the phenomena of decreasing  $R_S$  in the Nyquist plot, similarly to what occurred with the amylase and lipase alone. The reduction in degradation rate discussed above may be alleviated by modifying the film to prevent non-specific binding, such as with the use alternative crosslinkers (microbial transglutaminase has shown to be effective), inhibitors (orlistat or tendamistat for lipase and amylase, respectively) or with more specific film materials to trypsin (i.e., poly-l-lysine) [154]–[156]. Overall, however, the experiments conducted above allowed us to observe the impacts of these enzymes on the impedance of gelatin films, and it appeared that the presence of trypsin, rather than the non-specific enzymes, is responsible for inducing increments in impedance over the gelatin-coated sensors.

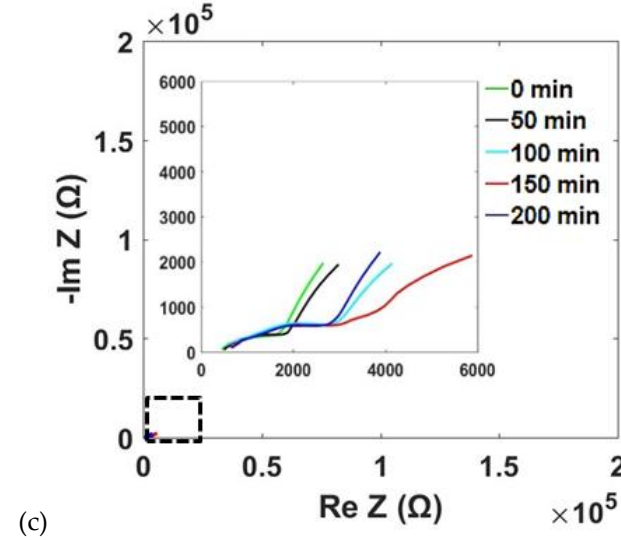
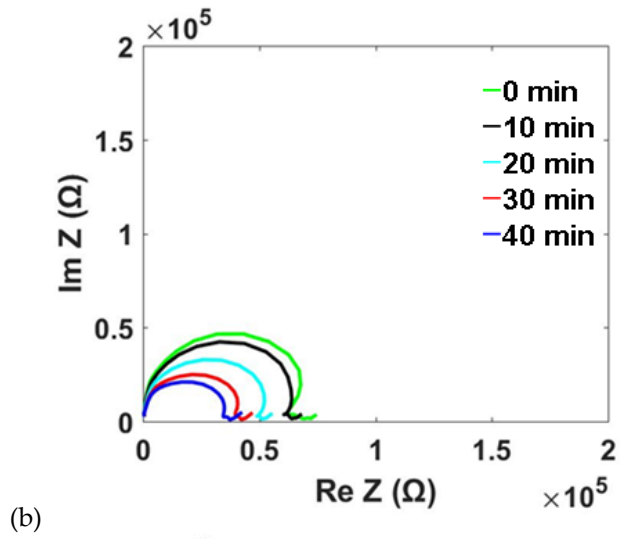
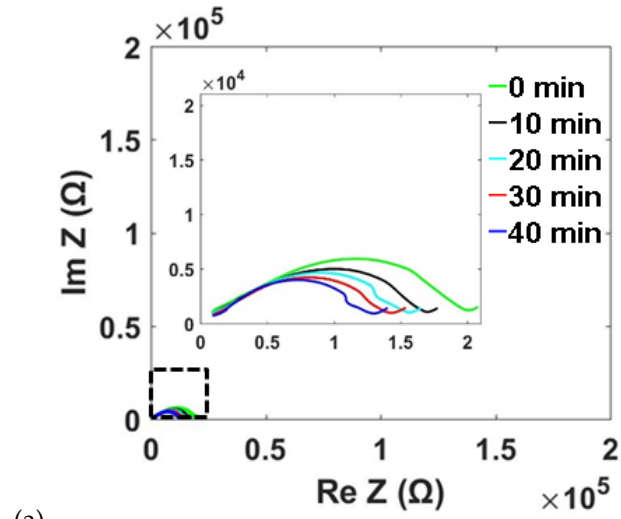


Figure 2-9 Representative Nyquist plots for gelatin-coated sensors to (a) 1 mg/mL lipase; (b) 1 mg/mL amylase; and (c) trypsin, amylase, and lipase, each at 1 mg/mL over time. (n=3).

#### 2.3.4 QCM Results

Figure 2-10 displays the QCM response of gelatin films when exposed to different solutions; PBS, different trypsin concentrations (0.5 and 1 mg/mL concentrations), amylase or lipase at 1 mg/mL concentration, or combinations (each at 1 mg/mL) of trypsin, amylase, and lipase. First, the mass response equilibrated under air for approximately 20 min (not displayed), and further equilibrated under the initial flow of PBS solution without enzymes for approximately two hours. Figure 2-10a compares the response to different concentrations of trypsin in buffer. The average gelatin degradation rates, calculated using the region with the largest slope magnitude, that occurred for 1 mg/mL and 0.5 mg/mL trypsin concentrations were 0.52 and 0.16 mg/min, respectively, while there was no significant degradation that occurred for lipase, amylase, or PBS alone, as indicated in Figure 2-10b. For the single enzyme mixtures in Figure 2-10c, gelatin degradation rates were quantified at a maximum of 0.09 and 0.12 mg/min for mixtures with lipase and amylase, respectively. For all three enzymes (each 1 mg/mL), the average rate decreased further to 0.04 mg/min. Since not every film possessed the same initial mass, the total change in mass is presented, with most of the film having been removed from the substrate by the 1 mg/mL trypsin. Additionally, values were recorded until the signal saturated, as saturation time varied depending on the amount of film removed from the substrate for each trypsin experiment. Though the slope for all three enzymes in Figure 2-10c combined appears steeper than those for just trypsin and either amylase or lipase individually, the time scale gives an indication that the rate of film removal from the substrate decreased significantly as the signal approached saturation. This indicates amylase and lipase

interfere with the gelatin removal from the substrate, though it is unknown as to whether they affect trypsin activity or the availability of peptide bonds in the gelatin.

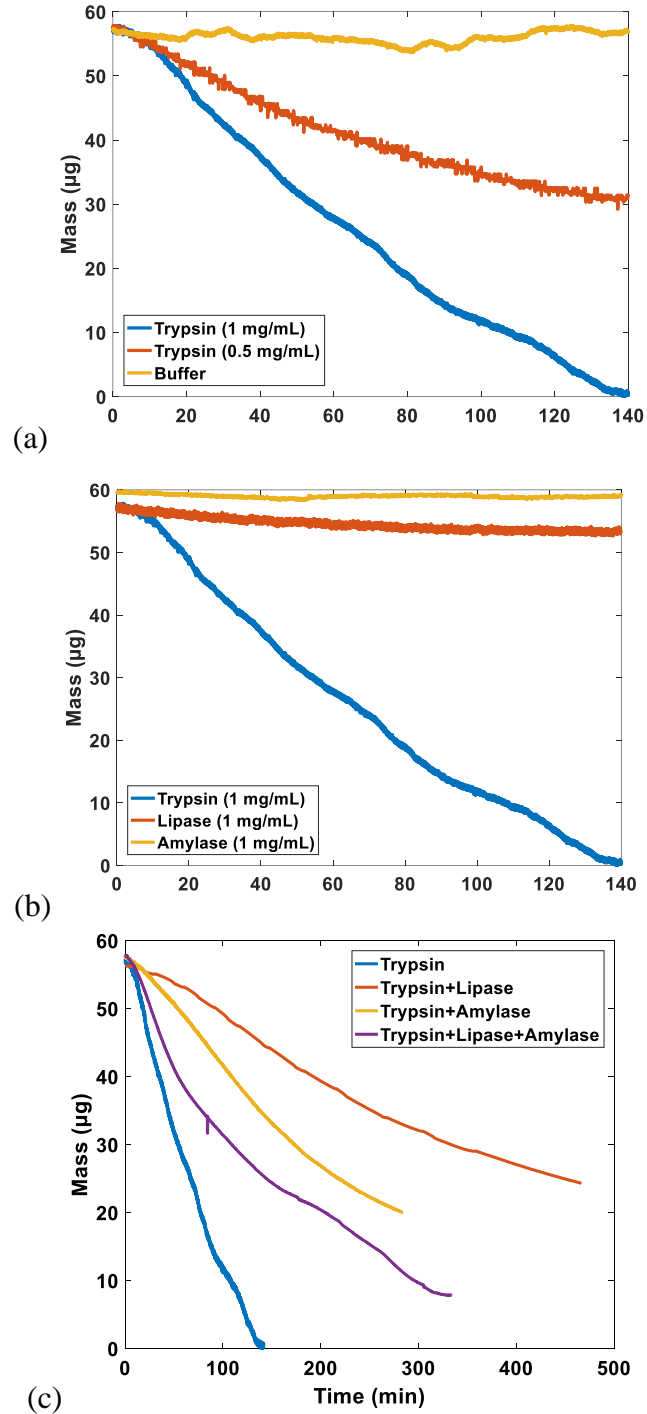


Figure 2-10 Representative QCM response of gelatin film to (a) trypsin at 1, 0.5 and 0 mg/mL in PBS, (b) trypsin, amylase, or lipase, each at 1 mg/mL, or (c) combinations of each enzyme with trypsin (each at 1 mg/mL). (n=3).

This section provided empirical evidence as to the feasibility of using gelatin films for measuring pancreatic trypsin through electrical impedance spectroscopy. I measured various electrical properties of the films such as overall impedance, which is then decomposed using Nyquist analysis and QCM to compare isolated trypsin versus nonspecific enzyme results.

#### 2.4 Film Reactions to Varying Enzyme Concentrations

Because I observed real-time changes in electrical properties of the gelatin films in response to pancreatic enzymes and a potential dependence on physical properties such as thickness, I wanted to further evaluate limitations of how these films react. In this section, I exposed the films developed in the previous section to a wider concentration range of pancreatic trypsin and observe potential time-scale dependencies in the film thickness and mass response.

Gelatin films were deposited via drop-casting of 500  $\mu\text{L}$  of 1 % w/v gelatin in  $\text{DIH}_2\text{O}$  over pre-weighed 10mm x 10mm Pyrex chips, then refrigerated overnight and crosslinked similar to the process described in Section 2.2.1. The mass and surface profiles were then obtained for each film-coated chip (FC).

FCs were immersed in glass petri dishes containing solutions, under 200 RPM stir via magnetic stir bar and 37-39°C, consisting of 0.1 M PBS only or PBS with varying concentrations of trypsin (1 mg/mL, 100  $\mu\text{g}/\text{mL}$ , 10  $\mu\text{g}/\text{mL}$ , and 1  $\mu\text{g}/\text{mL}$ ). FCs were then removed at 30 minutes, 1 hour, 2 hour, and 4 hour time points. After removing 3 samples at each time point, FCs were then rinsed with  $\text{DIH}_2\text{O}$ , blow-dried with  $\text{N}_2$ , then set aside to dry in ambient for 24 hours. FCs were then re-weighed and re-profiled.

Figure 2-11 illustrates the trends produced for both % change in mass and thickness, using equation (3) and its converted form when considering the change in mass. Initial film masses and thicknesses were calculated at  $0.572 \pm 0.01$  mg and  $6.80 \pm 0.44$   $\mu\text{m}$  thick, respectively. The thickness for the drop-cast films are likely lower than those from Section 2.2.1 due to the volume used and the available surface area and how they impacted potential spreading effects. I observed distinct changes in the rate of mass and thickness decrease with increasing trypsin concentration. The time points chosen only yielded saturation levels for the 100  $\mu\text{g}/\text{mL}$  and 1  $\text{mg}/\text{mL}$  concentrations, which appear to be evident at 2 hours of incubation, though it is clear the higher concentration induced faster degradation of the film.

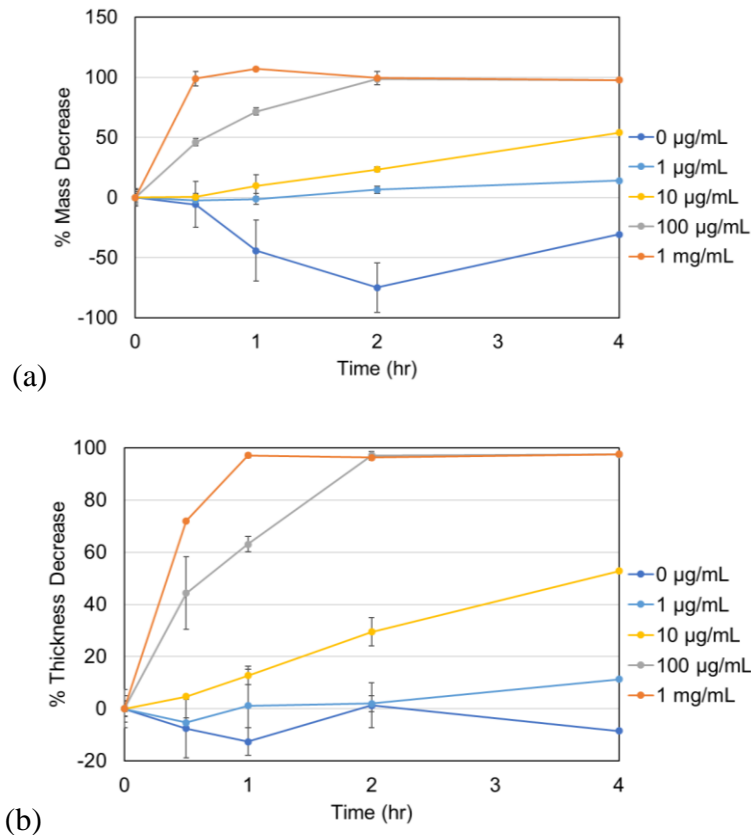


Figure 2-11 Gelatin film responses to varying trypsin concentrations through analysis of resulting %change in in (a) mass and (b) thickness, with each sample removed from incubation at different time points. Error bars depict standard deviation ( $n=3$ ).

I then used these trends to calculate the rate of reaction over time with each concentration, depicted in Figure 2-12 below. The time frames used for 1, 10, 100, and 1000  $\mu\text{g/mL}$  were, for mass, 2, 0.5, 0.5, and 0.5 hours, respectively, and for thickness, 2, 1, 0.5, and 0.5, respectively, due to the length of time observed until saturation. Not only do I observed that the changes in values occur in logarithmic trends, but that they are almost equivalent to each other for both mass ( $\text{mg/hr}$ ) and thickness ( $\mu\text{m/hr}$ ). This is critical in relating these metrics to enzyme concentration, which are quantified using the depicted equations and their respective  $R^2$  coefficients for variance.

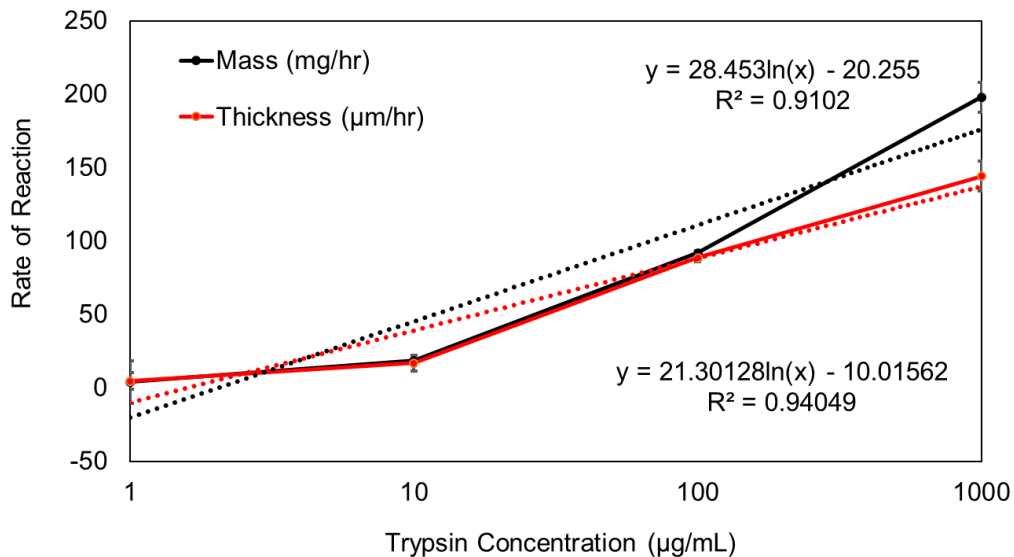


Figure 2-12 Logarithmic rate of reactions of gelatin films in solutions with varying pancreatic trypsin concentrations, calculated using the slopes in percent change of film mass and thickness. Error bars depict standard deviation ( $n=3$ ).

In this section, I briefly described our efforts to characterize the reaction response of gelatin films to varying concentrations of pancreatic trypsin. I evaluated the impact specifically on film mass and thickness, and enable us to use these metrics as means to evaluate the substrate reaction as a subsequent result from the presence of environmental trypsin.

## 2.5 System Modeling for Capacitive Sensing

### 2.5.1 Electrical Behavior of Biomaterial Films

Based on the impedance response demonstrated in Figure 2-6, I observed that the capacitive and resistive elements of the equivalent circuit model of the IDEs both change significantly as the gelatin film hydrolyzes from the trypsin. While the total impedance shifted more significantly at lower frequencies (<100 kHz) reflecting more capacitive effects compared to other frequency range, I also noticed measurable shifts at higher frequencies for resistive effects (>100 kHz), indicating the potential to adapt sensing strategies for either signal type. Because impedance sensing possesses more circuit requirements, adding further challenge to miniaturization of the sensing electronics, I was interested in focusing on transitioning from impedance sensing strategy to solely either a capacitive- or resistive-sensing strategy and determining which would have more sensitivity to changes in film reactions.

Capacitive sensing possesses several benefits over resistive sensing in understanding how thin films structures over IDEs affect either. When a thin film is deposited onto an electronic transducer, the double-layer capacitance ( $C_{dl}$ ), is affected, which can be expressed as the sum of the constant capacitance from an unmodified electrode ( $C_{Au}$ ) and a surface modifier ( $C_{mod}$ ), depicted in Figure 2-13 and expressed in equation (5) [39].  $C_{mod}$  is an indicator of binding to the electrode surface, dependent on the relative permittivity ( $\epsilon_r$ ) and thickness of the film ( $t$ ), and can be calculated by equation (6), where  $\epsilon_0$  is vacuum permittivity ( $8.85 \times 10^{-12}$  F/m) and  $A$  is the electrode area [153]. Equation (7), solving for  $C_{Au}$ , is similar, only with film thickness replaced by the distance between fingers ( $d$ ) [157].

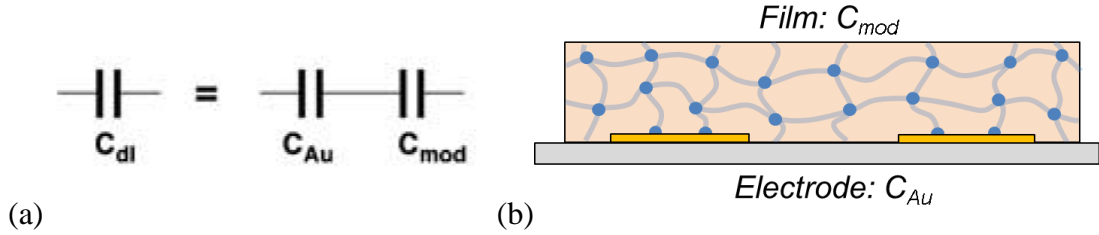


Figure 2-13 (a) Equivalent circuit model and (b) schematic for thin films over impedance sensors. Reproduced with permission from [39].

$$\frac{1}{C_{dl}} = \frac{1}{C_{Au}} + \frac{1}{C_{mod}} \quad (5)$$

$$C_{mod} = \frac{\epsilon_r \epsilon_0 A}{t} \quad (6)$$

$$C_{Au} = \frac{\epsilon_r \epsilon_0 A}{d} \quad (7)$$

The benefit of measuring capacitance lies specifically in  $C_{mod}$ . To clarify, resistive sensing of a degrading insulating film would require that the thickness of the film be reduced at its entirety at one specific location along the surface area for any charge-transfer to occur. This would also affect the  $C_{dl}$  at the location, so the response time would be equivalent. However,  $C_{mod}$  is affected by changes in the rest of the film thickness whereas  $R_s$ , described in Equation (4), is not, thereby indicating that the sensor would respond upon initial degradation at a certain change in thickness that would occur before the reaction has reached the sensor surface. While changes in  $R_s$  were evident through the Nyquist plots from impedance measurements, Equation (6) indicate measuring the capacitance alone can induce a faster change in signal. Ultimately, the more the film is degraded, the more  $C_s$  and  $R_s$  are prominent in their effect. In Appendix B, a COMSOL simulation of the equivalent circuit model is presented, which further highlights the feasibility for capacitive sensing.

### 2.5.3 Sensor Characterization with Varying Film Thickness

In determining the geometries for the next iteration of sensors used in measuring film degradation in response to enzymatic activity, I developed an optical mask, depicted in Figure 6-2 of Appendix A.2, with varying widths and spacings of the IDE electrodes. This was critical for understanding the impact of different film thicknesses on the resulting capacitance and how sensor performance could be optimized with different geometries. Each die on the mask also consisted of four sensors for both (a) higher throughput sensing of single targets or (b) sensing of multiple targets with each sensor output acquired through different multiplexer (MUX) inputs. This will be discussed further in Chapter 3.

Fabrication of the sensors was conducted via drop-casting as described in Section 2.2.1. This was because I was also interested in seeing how the film profile and thickness consistency would change when achieved at the individual die level versus the complete wafer level, as the latter had produced significant variability in the coverage of the film over the wafer, resulting in differing film thicknesses for devices at the center compared to those at the outer wafer perimeter. Additionally, I wanted to establish the expected film thickness when reusing the sensors with newly deposited films. After dicing, the resulting 4-sensor devices, where dicing tape remained over the contact pads as a mask, placed on the spin coater, 200  $\mu\text{L}$  gelatin solution (5 %w/v in  $\text{DIH}_2\text{O}$ ) was loaded on top with pipette, and the spinner was set to spin for 30 seconds at varying spin speeds. After spinning, the sensors were cooled overnight in ambient, crosslinked, and measured with a profilometer similar to those in Section 2.2.1.

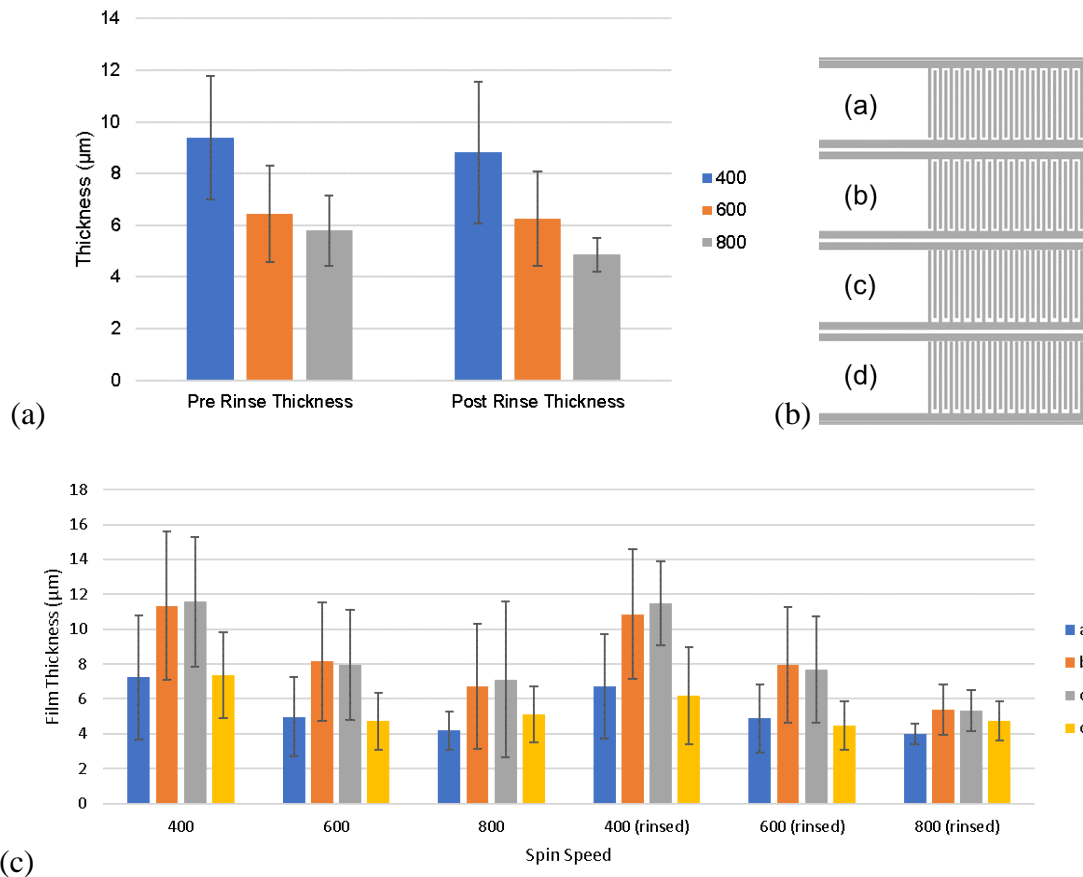


Figure 2-14 (a) Resulting gelatin film thicknesses and different spin speeds, both pre- and post- rinsing with DIH<sub>2</sub>O. (b) Top-level view of example sensor outline, with each sensor label. (c) Resulting film thicknesses for each spin speed, broken down by sensor – using labels from (b) – and rinsing. Error bars depict standard deviation (n=3).

Figure 2-14a depicts the resulting film thicknesses when sensors were spin-coated with 2 mL gelatin solution at 400, 600, and 800 RPM, as well as comparing them before and after rinsing with DIH<sub>2</sub>O and drying. There is an evident decrease in thickness with increasing spin speeds which follows the typical trends found in spin coating recipes, though it must be noted that these are all both (a) thicker than total wafer spinning at 400 RPM (400-700 nm) and (b) thinner than drop-casting alone (60-90 µm), as described in Section 2.2.1. A closer look, however, using the top view sensor image in Figure 2-14b, indicates that there is still lateral thickness variability in Figure 2-14c, where I observed that the films remain thicker for the two central sensors (b &

c) but are thinner for the outer sensors (a & d), likely due to surface tension of the liquid to the wafer. Fortunately, this variability does appear to decrease with increasing spin speed, as evident primarily with the 800 RPM spun sensors after rinsing, indicating a possible better drying efficiency.

The sensors were then analyzed for their series capacitance ( $C_s$ ) and resistance ( $R_s$ ) using an LCR meter (Agilent E4980A) controlled with LabVIEW. The values were calculated using the circuit model depicted in Figure 2-15a. First, depicted in Figure 2-15, I compared how each response changed both in the presence and absence of gelatin films, the latter of which were those spun at 800 RPM and after rinsing. Here, I first noticed that  $C_s$  and  $R_s$  increases and decreases, respectively, with decreasing finger spacing. This is expected through calculating  $C_s$  with equation (7) – using conditions  $C_s = C_{Au}$  when there is no film ( $C_{s-no\ film}$ ), and  $C_s = C_{dl}$  when there is a film ( $C_{s-film}$ ) – where  $C_{Au} \propto d$  (finger distance) and was calculated using,  $\epsilon_r=1.005$  for air, and  $A = 4.4 \times 10^{-6} \text{ m}^2$  (interfacing area, constant over different dimensions used in this work). For  $R_s$ , however, there is no reported dependence on the film thickness, and the trend I observed between the "Film" and "No Film" conditions did not aid clarity to the relationship. However, the measured  $C_{s-no\ film}$  varied compared to  $C_{Au}$ , which when taking the ratio of the measured value over the calculated value was referred to as an offset factor that is likely an effect of parasitic capacitances. Using the resulting  $C_{s-film}$ , I calculate the dielectric constant of the gelatin film ( $\epsilon_{gel}$ ) using equation (8), as  $A$  and  $\epsilon_r$  remain constant:

$$\epsilon_{gel} = \frac{\epsilon_{air} C_{s-film}}{C_{s-no\ film}} \quad (8)$$

This yielded an  $\epsilon_{gel}$  of  $1.23 \pm 0.06$ , which acts as a relatively efficient insulator (likely considering it had little to no moisture) and I could therefore use – along with their respective film thicknesses – to measure each respective  $C_{mod}$ , using equation (6), verifying there was a dependence of capacitance on the film thickness. I then used these factors to calculate the  $C_{dl}$  using equation (5). These results are summarized in Table 2-2.

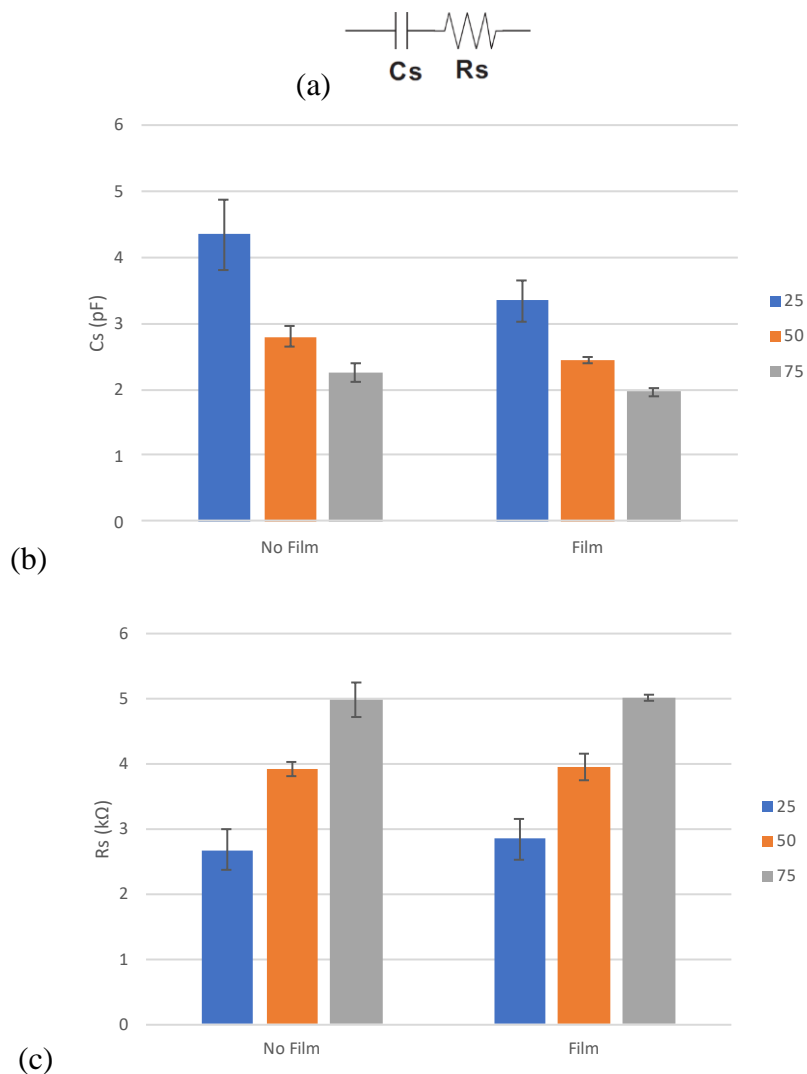
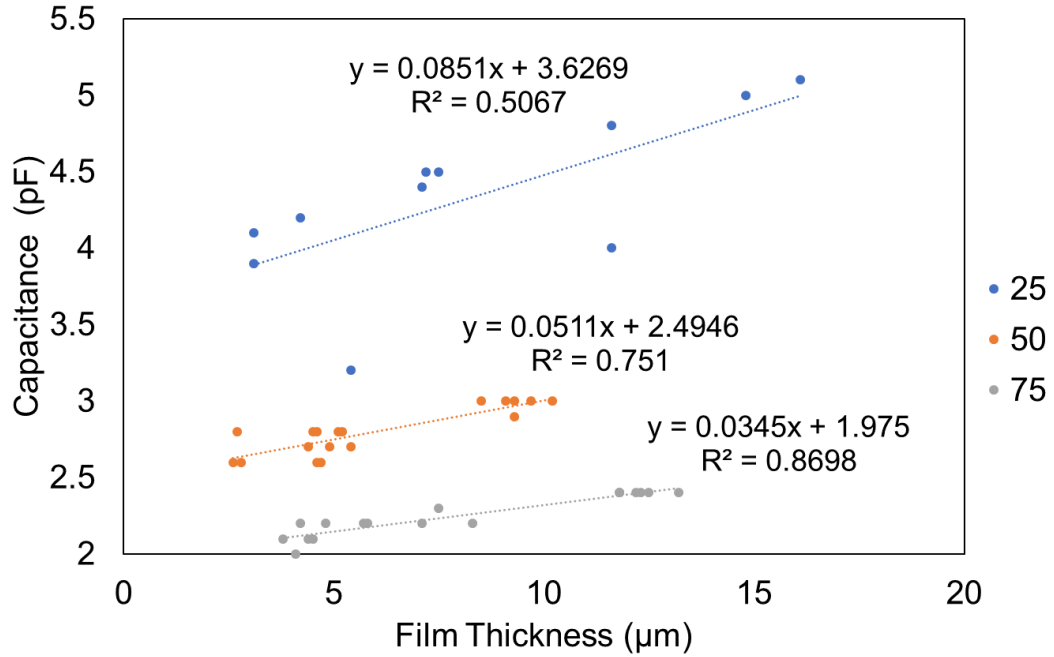


Figure 2-15 (a) Series equivalent circuit mode of LCR meter. (b-c) Electrical (capacitive and resistive, respectively) analysis of sensors across varying electrode spacings and comparing between the presence and absence of a film. Error bars depict standard deviation ( $n=3$ ).

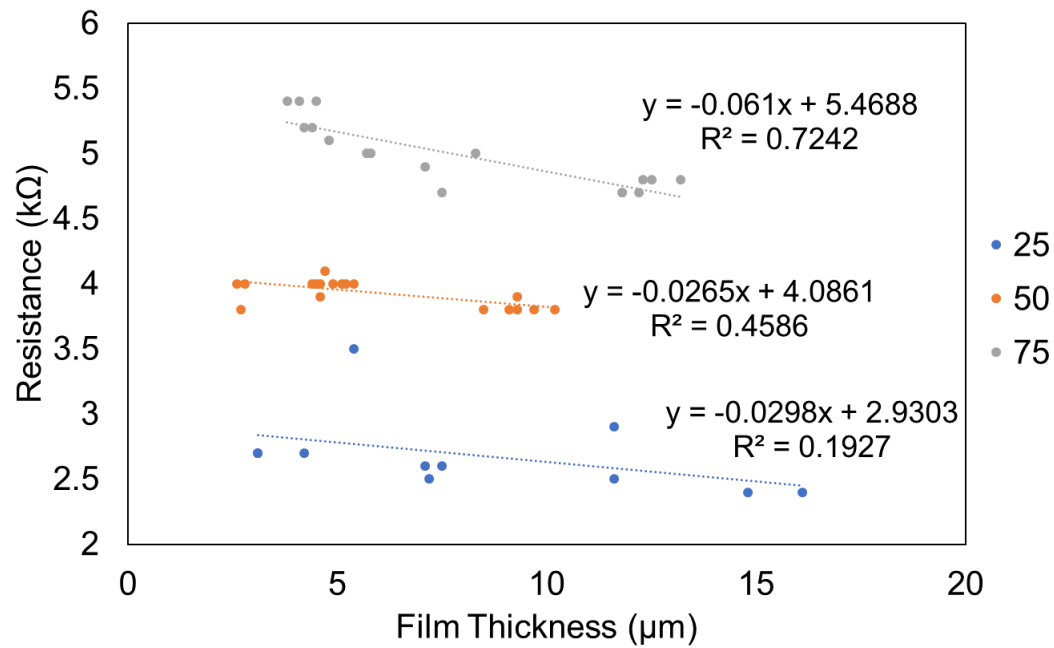
Table 2-2 Parameters used for capacitance analysis of gelatin films.

<b>Width/Spacing (<math>\mu\text{m}</math>)</b>	<b><math>C_{\text{Au}}</math> (pF) (Calculated)</b>	<b><math>C_{\text{S}} - \text{No Film}</math> (pF) (Measured)</b>	<b>Offset Factor</b>	
75	0.587	1.653 $\pm$ 0.35	2.8	
50	0.779	2.073 $\pm$ 0.27	2.7	
25	1.56	2.8 $\pm$ 0.77	1.8	
<b>Film Thickness (<math>\mu\text{m}</math>)</b>	<b><math>C_{\text{S}} - \text{Film}</math> (pF) (Measured)</b>	<b><math>\epsilon_{\text{gel}}</math> (Calculated)</b>	<b><math>C_{\text{MOD}}</math> (pF) (Calculated)</b>	<b><math>C_{\text{DL}}</math> (pF) (Calculated)</b>
1.27 $\pm$ 0.71	1.99 $\pm$ 0.1	1.205	36.93	1.582
1.15 $\pm$ 0.81	2.45 $\pm$ 0.06	1.182	40.04	1.971
1.04 $\pm$ 0.8	3.62 $\pm$ 0.1	1.294	48.43	2.650
	<b>Mean</b>	<b>1.23<math>\pm</math>0.06</b>		

Further analysis, displayed in Figure 2-16, was done to observe the effect of sensor spacing on sensitivity to the change in thickness. Regression analysis was performed with different thicknesses measured, and I found, using the slope from each linear fit trend, that the capacitance increased with increasing thickness more significantly when the sensor finger spacing decreased, indicated by the depicted formulas. I also measured resistance, which was also affected by the film thickness, but in the opposite direction – i.e. the sensitivity decreased with reduced IDE spacing – while the resistance overall would decrease as the film thickness increased. However, regression on these slopes indicated that this change in sensitivity for varying finger spacing was also greater for capacitance (slope= $1.0 \times 10^{-3}$ ) than resistance (slope= $8.0 \times 10^{-4}$ ), indicating that the response would be more sensitive by extracting sensor capacitance.



(a)



(b)

Figure 2-16 Regression analysis of different gelatin film thicknesses and their impacts on sensor (a) capacitance and (b) resistance across 25, 50, and 75  $\mu\text{m}$  electrode spacings.

While these results provide some insight as to the utility of measuring the electrical properties of these gelatin films, there are various limitations as to the extent of this utility. For example, because the films were dried hydrogels, the responses will vary significantly depending on their hydration level and respective conductivity when high ion or electrolyte concentrations in the surrounding media diffuse into the films; the former is limited with higher cross-linking, thus preventing it as a major concern, though a correction from a humidity measurement may also improve accuracy. This may impact film thickness as well, however sensitivity of these particular sensors was only tested within a select range of film thicknesses, preventing us from ascertaining to what extent the sensitivity changes at lower and higher thickness ranges, especially when thinner than the width of the electrode fingers. Additionally, it would be beneficial to test these responses when there was additional media, such as buffer, present above the films, which may affect the resulting double layer capacitance and solution resistance. Finally, even though I presented in Section 2.4 that the hydrolysis reaction between trypsin and gelatin affects the thickness – as well as the mass – of the film, not all reactant-substrate interactions manifest in such surface effects as opposed to the bulk or at more isolated regions. This will be addressed more in chapter 4.

In this section, I described efforts to relate film thickness to electrical properties using literature-based mathematical and equivalent circuit models, as well as perform basic computational modeling to establish relationships between film thickness to sensor capacitance. I further developed strategies for deposition of gelatin films onto microfabricated IDE electrodes, where sensor characterization with different electrode geometries is used to relate the resulting film thicknesses to intrinsic electrical

properties of the films – i.e. capacitance and resistance. This will be used toward determining parameter requirements in designing a microelectronics-based measuring system for film-based biosensing.

## 2.6 Conclusions

The work in this chapter demonstrated an impedance-based sensing strategy for measuring film-degradation using gelatin as a substrate for pancreatic trypsin. While sensor fabrication proved relatively straightforward, the information obtained offered broad insight to enzymatic interactions that occur between the film and various species in the media. I observed a linear relation for the rate of change in impedance over time by measuring the degradation rate of gelatin films by trypsin, and that nonspecific enzymes diminish this effect. The changes in impedance, as well as other electrical properties as determined in Section 2.5, resulting from changes in film morphology and thickness, are likely to translate to similar film and enzyme-targeting combinations.

Decomposing the impedance properties into its fundamental components provides various implications for system design and development into a capsule-based microsystem. In isolating capacitive and resistive elements of the film response to biochemical reactions, I evaluated their respective efficacies to determine optimal choices in the target system metric for assessing the local presence of enzymes. Minimizing system elements to the necessary components is critical when developing a microelectronics system, aiding in subsequent reduction in form factor to scales relevant for different domains, such as the human body. Potential strategies – i.e. a capacitive sensing microelectronic system – that could be implemented when

measuring biomaterial film reactions to biomolecular targets in complex environments such as pancreatic secretions *in vivo* will be discussed further in the following chapters.

### 3. Chapter 3: Packaging and System Miniaturization for Gastrointestinal Navigation

#### 3.1 Capsules and Gastrointestinal Sampling

As discussed in Section 2.1, various techniques are used for measuring GI enzyme content. However, they generally require multiple steps such as sample preparation and multiple rinsing cycles, preventing them from use for *in situ* sensing [158]–[161]. More importantly, samples must first be extracted using other tools and processed externally. Duodenal contents, for example, are traditionally extracted via endoscopic aspiration then analyzed through assay kits, while various sensing protocols for more specific analytes require separation techniques such as centrifugation or filtration [1], [47], [162]. For more direct sampling of GI fluidic contents, protocols vary between merely collecting stool contents to endoscopic aspiration, depending on the target [163], [164].

To transition to *in situ* biosensing for the benefit of real time data acquisition and procedural simplification as described in Chapter 1, strategies must be implemented that can either (1) reduce the number of steps involved or (2) incorporate them into the sensing system for rapid detection upon sampling. Toward this end, capsule-based integrated devices have recently been gaining traction as vehicles for sampling through the gastrointestinal (GI) tract that have the potential to achieve these tasks and overcome various limitations in current medical techniques, such as location restrictions or insufficient sensitivity measures [165], [166]. To become a viable medical solution for its respective function, capsules in the form of autonomous diagnostic systems must be able to navigate and function within the GI tract's

physiological environment, which is often chaotic and inhibitive to systems requiring control over the features affecting the sensing interface, which includes but is not limited to fouling or non-specific interactions [99], [100], [103], [167]–[170]. With the wide range of potential applications, capsules are becoming more ubiquitous in academic settings, and a few are experiencing success in industry aiding practitioners in the clinical field [171]–[173]. As mentioned previously, one of the most successful commercially available examples of capsule-based integrated devices is the capsule endoscope, such as the PillCam (Medtronic). It was initially introduced as a solution to extend the limited range of endoscopic procedures in the GI tract such as a colonoscopy or esophagogastroduodenoscopy [10], [174], [175]. The primary benefit of this technology over traditional endoscopy, other than that it does not require anesthesia or as much involvement from the clinician, is its enhanced ability to access difficult-to-reach GI regions. Overall, these detection technologies aim to understand the state of the GI environment for identifying pathological conditions or obtaining previously inaccessible information in a noninvasive approach.

GI fluids are used in diagnostics for isolating biomarkers related to specific GI pathologies, and targeting specific regions for sampling is critical for associating the biomarker with its source. Additional examples that have yet to mature to clinical implementation require specific sensors that often include complex surface modifications for binding or reacting with a target species, based on the biomarker of interest. One such device measures gas concentrations in the gut, which optical images cannot easily distinguish [100]. Though electrochemical gas sensors have been around since the 19th century, the novelty lies primarily with the integration of this sensor into

an ingestible system, thereby offering clinical potential that did not previously exist [101]. Another device uses fluorescence imaging to determine the occurrence of GI bleeding [99]. This device serves as another alternative to traditional endoscope procedures for real-time monitoring, with more specificity than using capsule endoscopy as discussed above. Additional examples warrant further discussion over the impact of capsule-based biomedical devices, and a prevalent theme is the integration of low-power electronics and relevant sensors within a compact ingestible package [11], [103], [168]–[170], [172].

The most important feature of capsule-based technologies is their departure from benchtop analytical systems toward miniaturization into an *in vivo* sensing platform. For example, while traditional endoscopy possesses more functions than capsule endoscopy, the latter isolates the task of image capture and transmission and delegates the required subtasks to various modules and components within the capsule package. The basic modules involved are depicted in Figure 3-1 below [176].

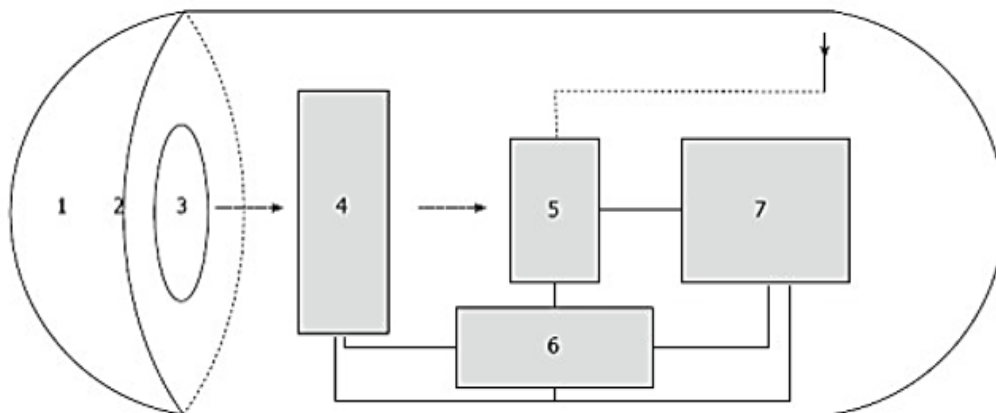


Figure 3-1 Modules contained within endoscopy capsule: (1) Optical Dome, (2) LED, (3) Short-focus lens, (4) CMOS image sensor, (5) RF module, (6) MCU, and (7) Power module [176].

The basic components required for most *in vivo* real-time sensing with wireless signal transmission include: a sensor, microcontroller, signal transceiver, power

supply, and a capsule-like package that can be swallowed [177]. However, for achieving alternative tasks, such as sensing, at the required size scale, energy remains a significant limiting factor that demands controlled allocation of power to as few system modules as possible for minimal time durations. Furthermore, complex tracking systems are often required to monitor whether or not the sensor measurements are occurring in the appropriate region [178]–[181]. These systems can include cumbersome equipment that the patient must wear in the form of a belt-like sensor array unit, and rely on magnetic or RF-based localization technologies that possess significant power requirements [182], [183]. While knowing the location of the capsule is necessary for certain functions where targeting requires more precision, such as monitoring transit time at specific regions or isolating positions of tumors or bleeding, the technologies described above still retain several other fundamental limitations. For one system referred to as the MTS-1 (magnetic tracking system), intestinal and abdominal movement can affect measurement accuracy, requiring simultaneous usage of computer tomography, and therefore additional costly equipment, to obtain anatomical data [178].

Though there are clear benefits to these anatomical tracking systems, they are not always necessary for the application of interest. Other than capsule endoscopes, they are rarely implemented in capsules designated for measuring specific biomarkers. Because these biomarkers are generally secreted at specific locations in the GI tract, we can leverage various features of these regions toward ensuring that the system can target them. One such feature that varies consistently throughout the GI tract is the pH, as illustrated in Figure 3-2 [184], [185]. The pH balance is critical to healthy GI

function, as imbalances can be indicative of or lead to harmful conditions such as inflammatory bowel disease (IBD) or irritable bowel syndrome (IBS), among others [186]–[189]. The pH is also necessary for regulating enzyme and other digestive functions, as most enzymes, such as those relevant to this work in Table 3-1, possess optimal pH ranges [190], [191]. Using materials that respond directly to pH can aid as a passive means of not only targeting the appropriate region and its respective fluid, but ensuring the fluid has a pH within the range for optimal enzyme activity, such as those discussed previously in this thesis.

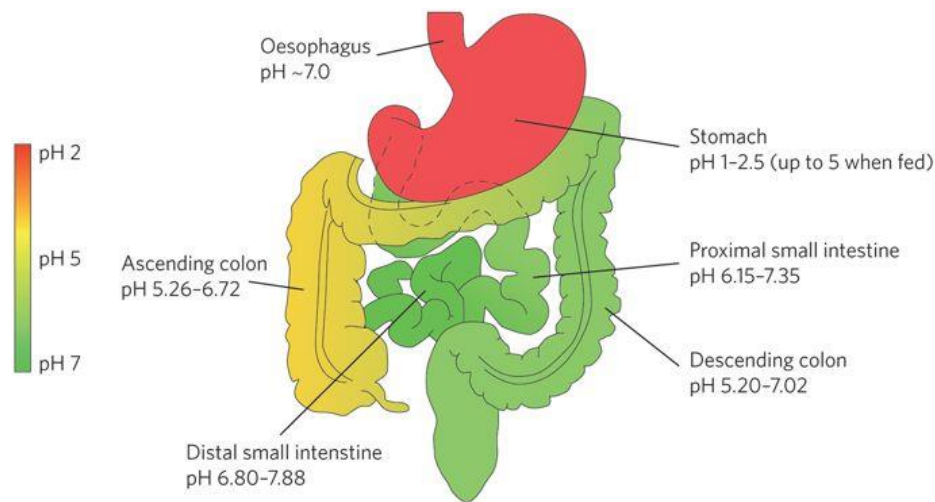


Figure 3-2 Human GI tract morphology with respective pH ranges. Reproduced with permission from [184].

Table 3-1 Various GI enzymes and their pH for optimal activity [16].

Enzyme	pH Optimum
Gastric Lipase	4.0-5.0
Pepsin	1.5-1.6
Pancreatic Lipase	8.0
Trypsin	7.8-8.7
Pancreatic Amylase	6.7-7.0
Urease	7.0
Maltase	6.1-6.8

In this chapter, I elaborate on our development of a wireless electronics system and its encapsulation in a capsule package for monitoring the ability to sample fluid at various targeted GI regions. The electronics interface with similar sensors as those developed in chapter 2, but that (a) require low power and (b) use surrounding pH to approximate location. A 3-D printed custom package encapsulates capacitive sensors, which are multiplexed and interfaced via a capacitive-voltage converter (CVC) with a Bluetooth system-in-package (SiP) that can pair with a mobile device via Bluetooth Low Energy (BLE). The capsule design possesses gratings that are plugged with different polymers, which dissolve under various biochemical conditions to allow for selective fluid entry into a sensing chamber. Once the environmental condition (pH in this study) is met, the dissolution of the polymer in the grating is detected by the capacitive sensors due to fluid entry changing the dielectric property of the chamber.

The polymers tested were chosen to demonstrate potential for sampling in a variety of regions in the GI tract based on pH, with an emphasis on sampling pancreatic secretions as depicted in Figure 3-3. The transition in pH at the duodenum from acidic to neutral conditions due to reactions of gastric juices with pancreatic bicarbonate, which occurs over a time period of ~30-60 minutes, offers a distinct event and time frame that is used in our design to target and sample pancreatic secretions. The gratings are filled with various formulations of pH-sensitive copolymers composed of acrylic and methacrylic acid that are currently used in the pharmaceutical industry for drug delivery to specific GI regions [192]–[194]. Different coating thicknesses are tested to evaluate control over dissolution at varying time scales, as well as combinations, or

layers, of coatings for more complex sequences. Here, I discuss the design of the system packaging, electronics, and their miniaturization.

Dr. Luke Beardslee contributed to the circuit and PCB design for the electronics system, as well as some of the initial capsule concepts. Justin Stine contributed to electronics design, programming, and troubleshooting. Rajendra Mayavan Sathyam contributed to microcontroller programming and development of the android application for signal acquisition. This work was published in contribution to [195].

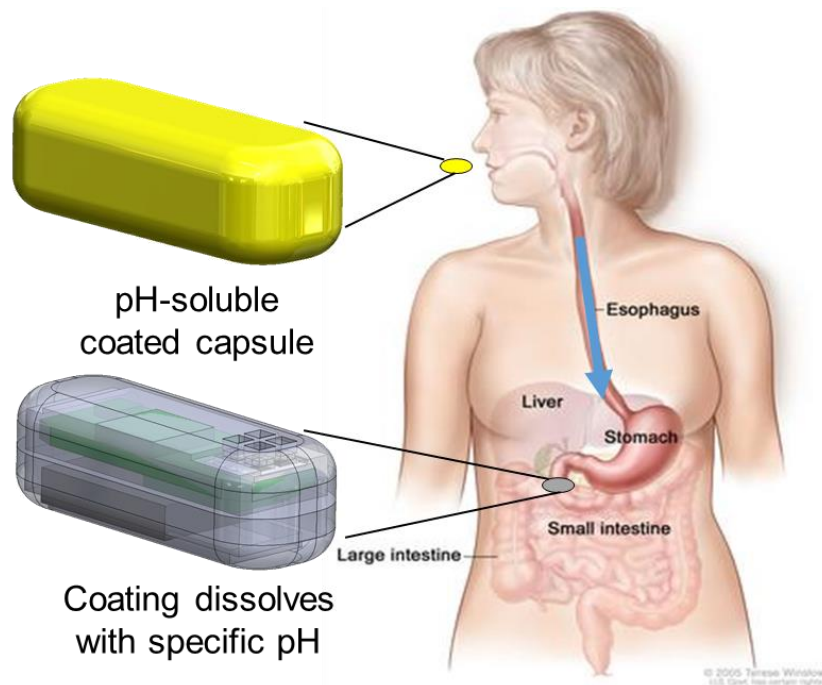


Figure 3-3 Depiction of system outlook and application (Image credits: National Cancer Institute). Polymer coatings are intended to dissolve at either the stomach (pH 1.5-3) or the duodenum (pH 7-8.5). At the duodenum, gastric acid-neutralizing bicarbonate is secreted from the pancreas via the sphincter of Oddi.

### 3.2 System Description

#### 3.2.1 Sensors and External System Electronics

Electrodes consisting of four sensors with a footprint of 3 cm x 1 cm (Appendix A.2) were obtained through a standard “lift-off” process as described in Section 2.2.1.

The resulting interdigitated electrodes (IDEs), a total of 72 pairs, were 50  $\mu\text{m}$  wide with 50  $\mu\text{m}$  spacing and 2 mm long. IDE devices were then diced using a standard dicing saw (Microautomation, Centreville, VA).

The electronics, including various off-the-shelf integrated circuits (IC), used to operate the capsule are summarized in Figure 3-4. In our configuration, four identical capacitive transducers are connected with a multiplexer as inputs (MUX IC, DG4052, Analog Microelectronics, Mainz, Germany), each of which is measured using a CVC IC (CAV444, Analog Microelectronics). The voltage output is connected to the analog-to-digital converter (ADC), a part of the microcontroller unit (MCU, BGM121, Silicon Labs, Austin, TX), which transmits the signal either serially to a computer via UART or wirelessly to a mobile device via BLE, respectively. General-purpose input/output (GPIO) pins from the MCU control the MUX to determine which sensor connects to the CVC. BLE is used as the wireless signal transmission technology because of the ease of interfacing with a smartphone, the availability of components that fit the needed form factor, and the availability of low-power components with a sleep mode. The rechargeable 14 mAh at 3.7 V lithium polymer battery (Powerstream, Orem, UT) was the optimal choice for the design; it satisfies the constraint of a small form factor and is able to source enough power for wireless transmission. Figure 3-5 presents the calibration of the ADC output potential using capacitors with known values. In addition, this figure displays data from the sensors being inserted into and removed from buffer via UART and BLE, respectively, where the slight elevation in signal after removal is due to residue buffer remaining on the sensor surface.

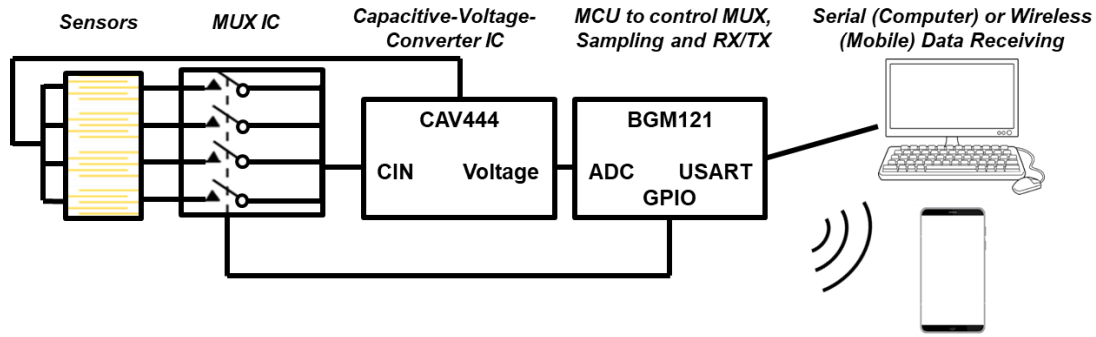


Figure 3-4 System electronics overview. Circuit design includes a multiplexer (MUX) integrated circuit (IC), a capacitance-voltage-converter (CVC) IC, a 1.5 MHz step-up DC-DC converter, and a BLE system-in-package (SiP) micro-controller unit (MCU).

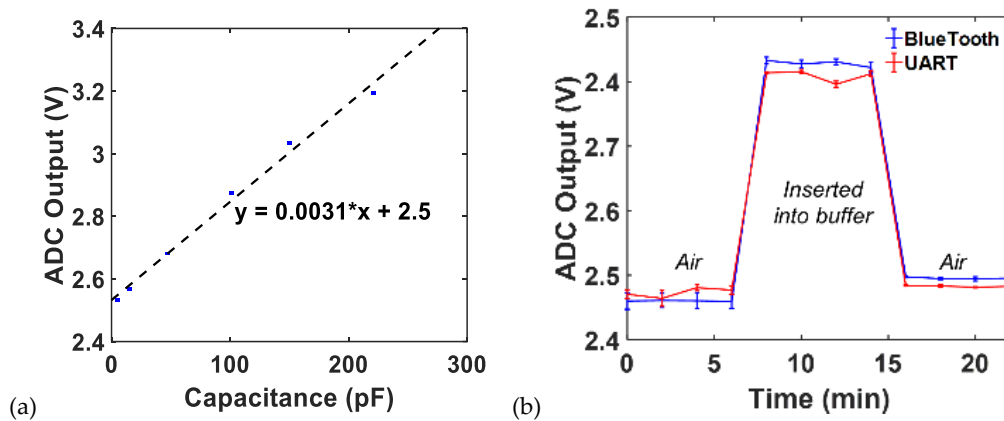


Figure 3-5 (a) Circuit calibration with known capacitors across four multiplexed inputs. The resulting system senses capacitive changes in the 0.8-220 pF dynamic range with a sensitivity of  $3.2 \times 10^{-3}$  pF/mV and operated using a 3.3 V source. (b) Data comparison between Bluetooth versus serial (UART) communication in different experiments, where the capsule (open gratings) was measured in air, inserted into buffer, then removed. Error bars depict standard deviation ( $n=4$ ).

### 3.2.2 Capsule Package Design and Materials

Each capsule is designed in SolidWorks (Dassault Systemes, Vélizy-Villacoublay, France) and 3-D printed from a biocompatible acrylic resin (MED610) using an Objet30 Pro (Stratasys, Rehovot, Israel) to assess the feasibility and utility of the capsule packaging and embedded gratings for sampling, as well as achieve the desired form factor according to previously determined standards for capsule endoscopy [10], [174]. The capsule designs and prints in Figure 3-6 are used for

experiments using an external circuit layout, where only the sensors are inserted into the capsule and the electronics remain external on a soldered protoboard (Adafruit, New York, NY). Gratings consisting of a 3x3 array of 0.4 mm x 0.4 mm holes, which function primarily as chamber inlets, were positioned over sensor regions for fluid accessibility into a hollow space, or sensing chamber. A slot with 600  $\mu\text{m}$  thickness and 1.1 cm width was created to allow for sensor insertion while sensor contact pads remained on the outside of the capsule. The sensor and slot interface was epoxied for sealing, then the capsule was immersed for 1 second in highly viscous 14% Eudragit S 100 (Evonik, Essen, Germany), a methacrylic acid–methyl methacrylate copolymer with 0.3% sodium laurylsulfate in methanol for dip-coating individual layers over up to 5 successive cycles. No bubbles appeared, indicating the polymer solution was not displacing air in the sensing chamber and therefore did not cause the capsule to fill and contact the sensors. Cross-sectioned images were taken of the grating regions, two of which (0 and 1 coating) are depicted in Figure 3-7a-b, and analyzed for thickness over grating and non-grating regions in Figure 3-7c.

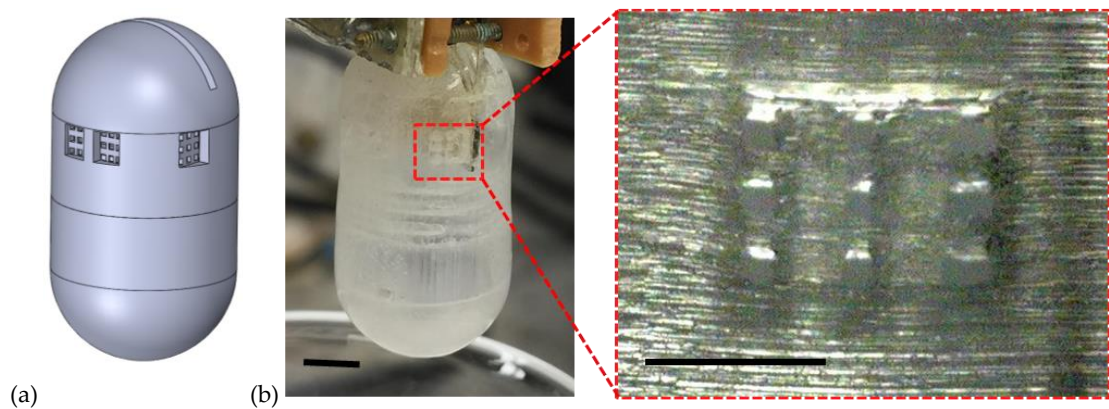


Figure 3-6 (a) CAD model of the capsule used with external circuit. (b) 3-D printed version with zoomed up view of gratings. Scale bar = 1 mm.

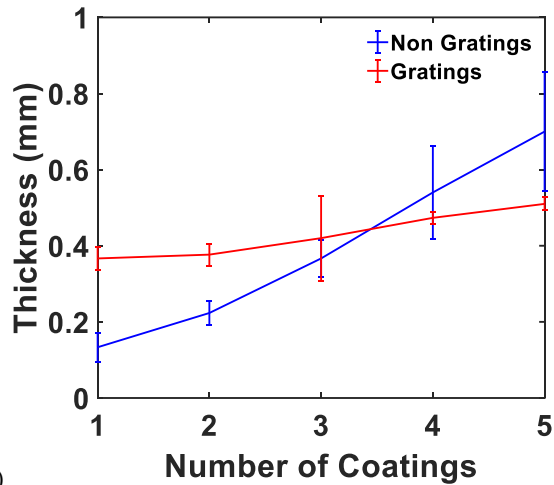
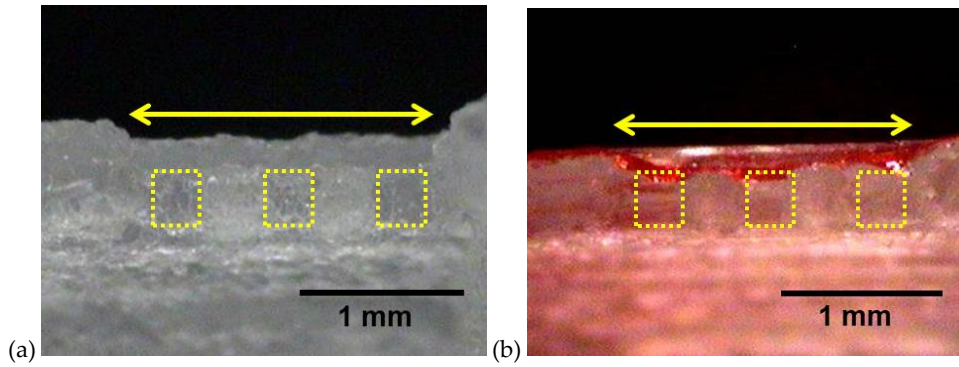


Figure 3-7 Cross-sectional optical images of the sampling gratings (a) uncoated and (b) with 1 coating of polymer, where yellow arrows indicate the grating locations and yellow boxes indicate the inlets. (c) Characterization of polymer coating thickness vs. number of dipping steps from both non-grating and grating regions over the 3-D-printed capsule surface. Error bars depict standard deviation (n=3). Scale bar = 1 mm.

### 3.2.3 System Miniaturization and Assembly

The circuit was embedded into a four-layer printed circuit board (PCB, 25 mm x 10 mm x 2 mm) made of FR4 with a silver finish (Sunstone, Mulino, OR). The PCB, assembled by Screaming Circuits (Canby, OR), is depicted in Figure 3-8a, indicating the pins used to connect to the battery, the contact pads for connecting to the sensors, and the pins for programming the MCU. The schematic of the assembled capsule setup is depicted in Figure 3-8b. New sensors (Appendix A.3), with a smaller footprint to fit between the PCB contact pads while maintaining the same capacitance range, depicted in Figure 3-8c, were fabricated as described previously. The new

sensor IDEs were 10  $\mu\text{m}$  wide and 1.5 mm length, while the new finger spacing of 10  $\mu\text{m}$  increased the sensitivity from 3.6 (for the 50  $\mu\text{m}$  spacing sensors) to 7.3 pF/mV. These sensors were designed to be utilized with the biomaterial films that were described in Section 2.4. Most experiments were performed with the PCB connected to a power supply through wires, as the battery performance had not been optimized at this point for experiments requiring long durations. The PCB and wires were encapsulated in a conformal coating, consisting of acrylic copolymer (CAIG Laboratories, Inc., Poway, CA) for circuit and electrical insulation, and inserted into a modified 3-D printed capsule which directly interfaced the chamber inlets with the sensors. A photograph of the assembled capsule is depicted in Figure 3-8d, while the system specifications are listed in

Table 3-2.

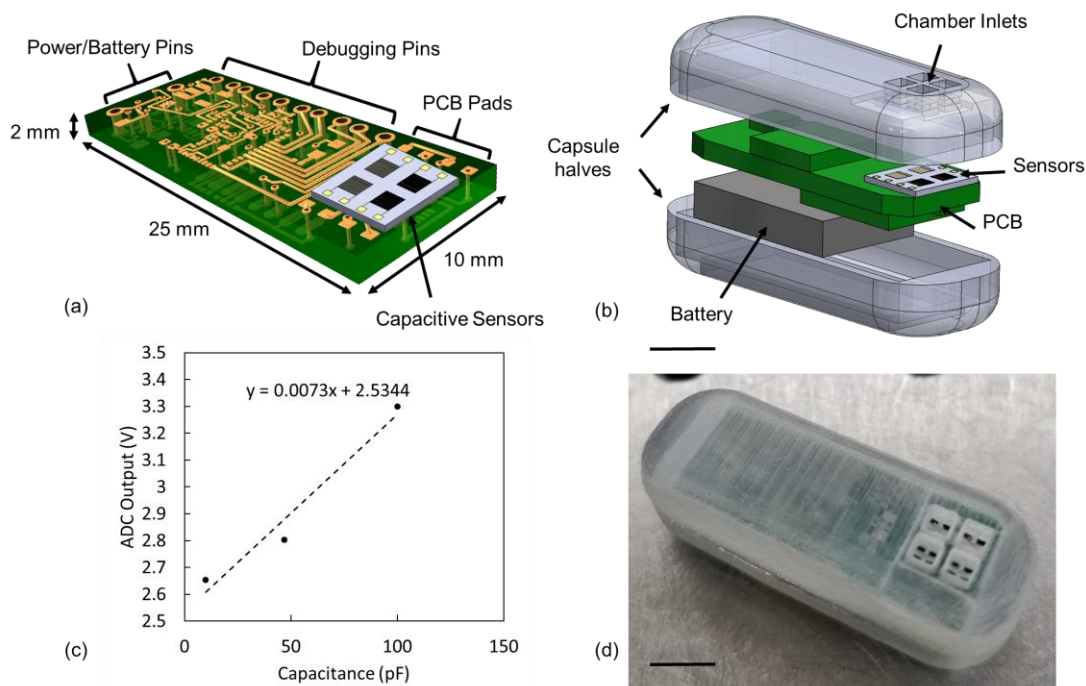


Figure 3-8 (a) PCB rendering with sensor die fixated between designated pads using epoxy. Contact was made by curing conductive silver ink. (b) Schematic of the assembled capsule setup. (c) Calibration of BLE MCU at the PCB level using standard known capacitors. (d) Photograph of assembled capsule. Scale bar = 5 mm unless otherwise specified.

Table 3-2 System Specifications

3D-Printed Shell		Electronics	
Outer Diameter	12.7mm	PCB Length	25.8 mm
Inner Diameter	11.5 mm	PCB Width	10.4 mm
Length	35 mm	Sensor Capacitance Range	0.8-220 pF
Inlet area	4 mm <sup>2</sup>	Sensor Capacitance Sensitivity	7.3 pF/mV
<b>Sensors</b>		Operating Voltage	Operating Voltage
Finger Width	5 μm	Current Consumption	Active: 5 mA
Finger Spacing	5 μm		Deep Sleep: 2.5 μA
Finger Length	750 μm	Battery (Powerstream)	Li-Polymer/14 mAh/3.3 V
Number of Fingers	80	Wireless Communication	BLE 2.4 GHz
Finger Thickness	200/20 Au/Cr nm		

### 3.2.4 Experimental Procedures for pH Sequences

For the circuit layout external to the capsule, the sensor contact pads were connected to the circuit while sandwiched between PCBs with soldered spring-loaded

pins. The capacitance was then transmitted serially from the BGM121 wireless starter kit (WSTK) via UART. All capsules were inserted into heated solutions (37°C) under stirring conditions (250 RPM). A measurement sequence was defined to evaluate polymer coating degradation at various pH states, according to a known pH dissolution profile. Beginning with measurements in air for 5 min, the capsule was then inserted into a solution with a negative control pH, the level of which depended on the polymer plug used. The pH was then adjusted progressively to the positive control pH that was expected to cause dissolution. Solutions beginning with acidic pH consisted of 0.1 M acetic acid (pH 2.9), while solutions beginning with neutral pH were 0.1 M phosphate buffer (pH 7.6). These pH levels were chosen to reflect the pH range of the target regions of the GI tract, specifically the stomach and small intestine for acidic and neutral secretions, respectively [196], [197]. Progressive pH adjustments were performed every 30 min for acid- and neutral-solutions via droplets of 1 M phosphoric acid and 1 M sodium hydroxide, respectively, measured using a standard pH meter (Oyster-10, Extech Industries, Nashua, NH). The coating procedure discussed in Section 3.2.2 was repeated, three coatings each, for Eudragit formulations L 100 and E PO, intended to dissolve at > pH 6 and < pH 5, respectively. The pH progression for their respective experiments were 2.9 to 7.6 and 7.6 to 2.9 in discrete increments of ~1.0 to control for the sensor responses while beginning in non-soluble pH conditions designed to inhibit dissolution. The procedure was repeated with 3 coatings of L 100, followed by 3 coatings of E PO (depicted in the coating rendering in Figure 3-10d), and tested with a pH sequence of 7.6 to 2.9 to 7.6. Once the positive control pH was

reached, the capsule was removed from solution for 10 min and signal transmission was terminated.

The miniaturized system of the capsule with inserted PCB was coated with three coatings of E PO solution, then immersed into both pH 7.6 and pH 2.9 solutions while recording capacitance over time. The recorded capacitance was obtained via BLE by pairing with an Android phone, initiated via a modified application from the manufacturer (Silicon Labs). The data was stored onto the mobile device as a text file and analyzed using a desktop PC. Photographs were taken at the 0, 30-minute, and 1 hour time points during immersion to record progress in coating dissolution. All polymer solutions were 30% w/v in methanol and dyed for enhanced visualization.

All data was plotted using a custom MATLAB (MathWorks) graphical user interface (GUI). For the WSTK obtained data, the signals were recorded into a text file using RealTerm. For the PCB layout, the recorded capacitance was obtained via BLE by pairing with an Android phone, as described previously.

### 3.3 Experimental Results

#### 3.3.1 Sensor Responses

The sensor responses, both in voltage at the ADC and the corresponding capacitance, for capsules with varying numbers of coatings are depicted in Figure 3-9. For 0 coatings, the point at which the capsule was inserted into buffer is indicated by the sharp increase in capacitance at around 5 minutes due to immediate entry of buffer, causing an instant change in the medium dielectric constant at the sensor surface. The data for 1 coating was omitted due to the lack of sealing of the gratings, producing a

similar result as that of the 0-coating sequence. With an increase in the number of coating layers, the rate of the capacitance change is reduced significantly, recorded at approximately 16.0, 5.6, and 1.1 pF/min for 0, 2, and 3 coatings, respectively. The system with 4 coatings did not open within the 140-minute duration, though some drift in capacitance due to a potential increase in humidity was seen. As expected, additional dip coatings corresponded to an increase in the fluid entry time, allowing us to tailor the packaging to different time scales based on coating thickness from corresponding measurements in Figure 3-7c.

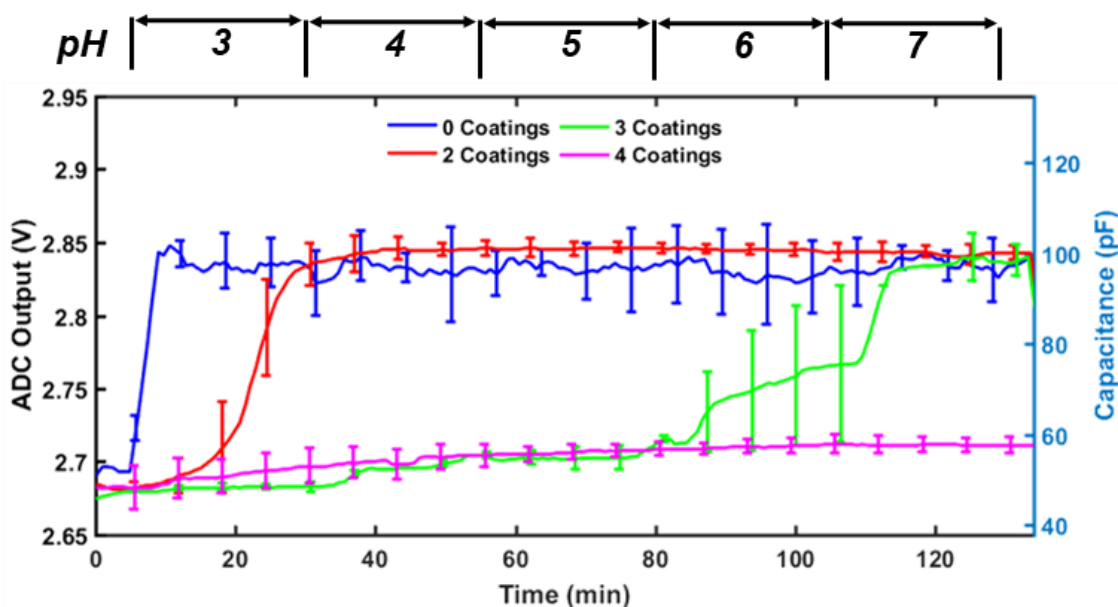


Figure 3-9 Sensor responses (inserted into buffer at 5 min) of capsules with different numbers of S 100 coatings (0, 2, 3, and 4, respectively) with increasing pH using titers of 1 M NaOH. Error bars depict standard deviation (n=4). Chamber filling is characterized by a capacitance change of ~50 pF from the initial capacitance in air. For each formulation, it was determined that 3 coatings were optimal for the w/v% used.

### 3.3.2 Coating Variety and Combinations

After varying the coating thickness, I tested polymer formulations that would dissolve at different pH ranges. Real-time capacitance measurements for the pH sequences of the L 100 and E PO coated capsules (3 dip-coatings each) are depicted in

Figure 3-10a-b, respectively, with the latter pH in which the coatings were intended to dissolve enough to achieve sampling; the distinct drop in pH toward the end of each sequence denotes when the capsule was removed from the sample. The resulting capacitance indicated that sampling occurred in the appropriate ranges (neutral for L 100 and acidic for E PO), implying both the viability of these materials as coatings and their potential for targeting different GI regions. To allow for sampling in a more complex sequence such as that expected between the mouth and the small intestine (neutral – acidic – neutral pH, respectively), I layered 3 coatings each of L 100 and E PO sequentially over the capsule surface, depicted in Figure 3-10c. The resulting measurements with the sequence used, consisting of pH 7 to 3 to 7, are displayed in Figure 3-10d, where the increase in capacitance to saturation occurs at the return to neutral pH. This indicates that the E PO coating was able to protect the L 100 coating while transitioning to pH 3, while the L 100 coating ensured the gratings were sealed until the system returned to neutral pH.

It is important to note that the slope between the baseline capacitance and the saturated capacitance varied with polymer type. This difference in timing was most likely affected by variations in each polymer's dissolution rate. Alternatively, it is possible that it was also affected by their respective apparent viscosity at the solution concentration used (L 100: 60-120 mPa-s, S 100: 50-200 mPa-s, E PO: 3-6 mPa-s, according to the manufacturer), which varies the amount of plug infill during the initial coating and polymer remaining in subsequent steps. This would also impact the rate of solvent dissipation, specifically the methanol to air, for each coating. No observable

differences in coating appearance were seen during the coating process with each interval between coatings.

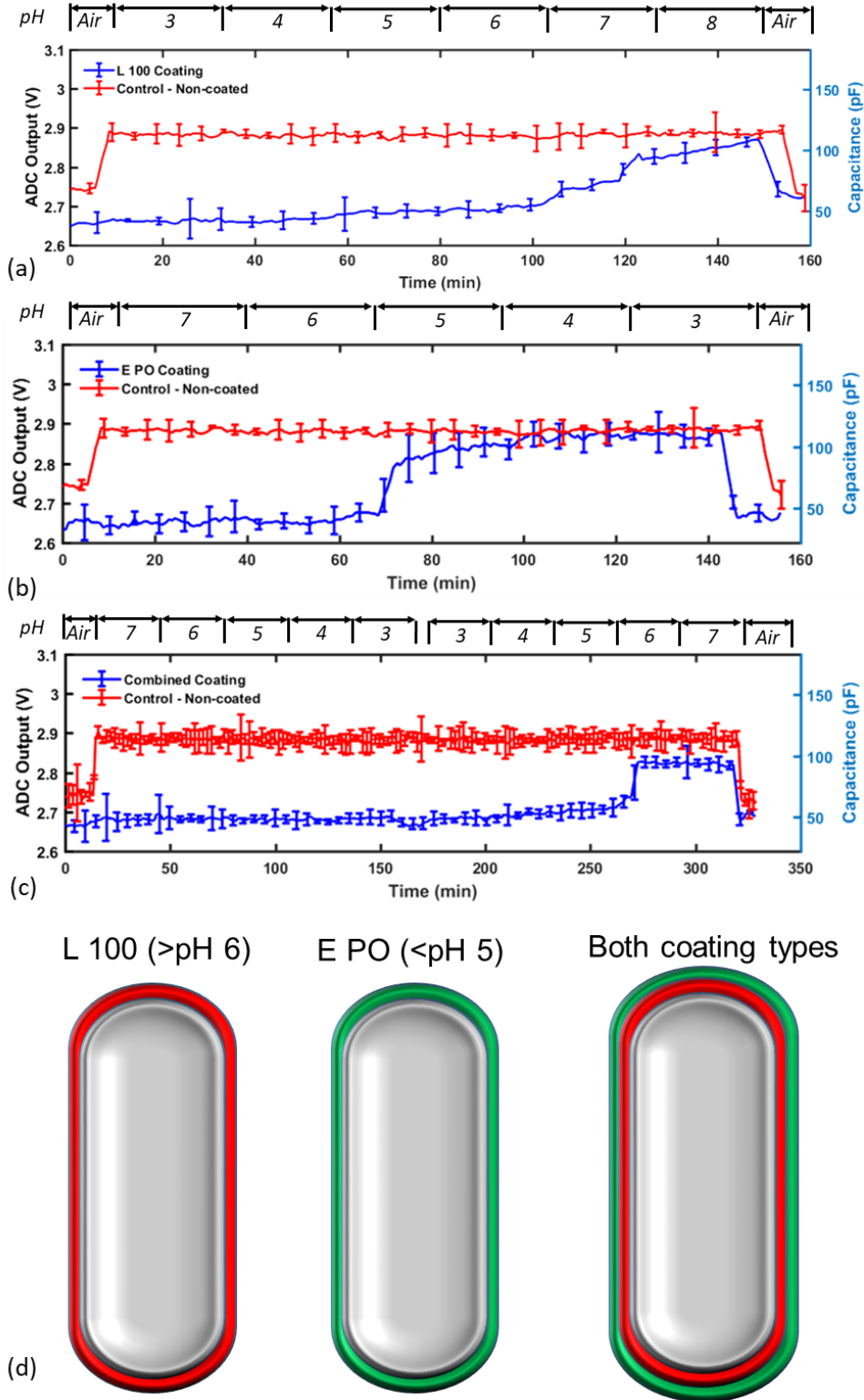


Figure 3-10 Sensor responses inserted into capsules with different types of coatings (3 dip-coatings each) compared to uncoated controls: (a) L 100, (b) E PO, and (c) combined coatings, where E PO is outer-most and L 100 is between the 3-D-printed capsule and the E PO layers. Error bars depict standard deviation (n=4). (d) Capsule rendering for displaying coating conditions for each sequence.

### 3.3.3 Assembled Capsule Coating and Sensor Responses

Assembled capsules were tested to ensure functionality of the fully integrated system. The insulated PCB with the sensor connected was inserted into neutral buffer, before insertion into the capsule, resulting in a spike and saturation in capacitance similar to the previous immersion experiments (data not shown). The current was monitored throughout to ensure the insulation of the board components was leak proof. The system was then inserted into the capsule and retested, producing the real-time capacitance readout (data not shown). The capacitance measurements produced from the polymer coated capsule in both neutral and acidic buffer are depicted in Figure 3-11. Here, I observed that the sensors continued to measure the same capacitance from beginning to end for the neutral buffer, indicating that there was a lack of buffer inflow because the plug remained intact. Conversely, for the acidic buffer, a spike in capacitance is measured at about 23-27 minutes for each capsule, about 18-22 minutes after insertion into the solution. Interestingly, I observed that the change in capacitance is only ~20 pF compared to the 50 pF shift for the external electronics, which I found was due to the presence of additional parasitic capacitances introduced during the assembly process. However, there remains a distinct signal increase in the acidic pH compared to the neutral pH upon dissolution of the polymer coating.

For additional qualitative validation, the photographs in Figure 3-12 depict little to no change in the capsule coating throughout the neutral buffer sequence, whereas the coating is mostly dissolved – both in the gratings the non-grating regions of the capsule surface – as the experiment with the acidic buffer progressed. This result is consistent with the recorded capacitance measurements, indicating a specific time

point at which the buffer contacted the sensor. Based on the results in Section 3.3.1 and 3.3.2, I could tailor this fluid intake for different timing windows by varying coating thicknesses, as well as coating materials.

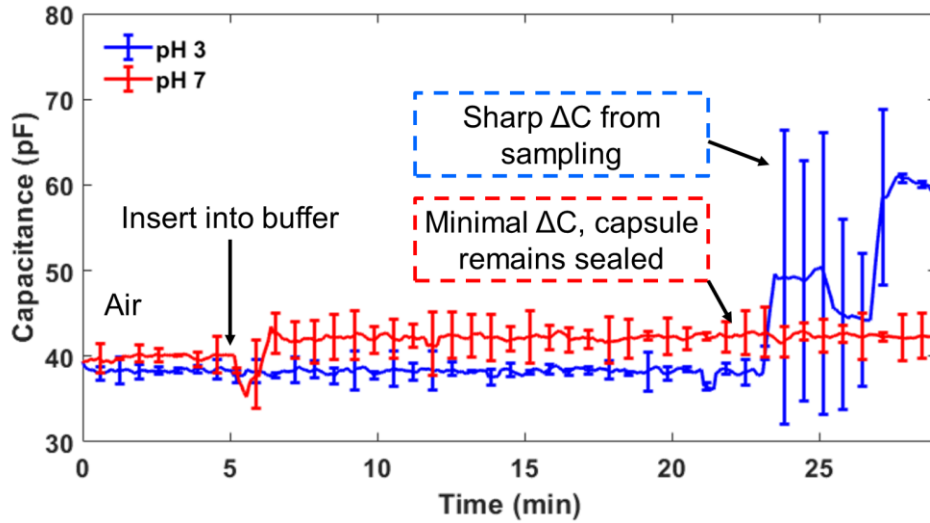


Figure 3-11 Real-time representative trials of capacitance measurements obtained via BLE from the 3x coated capsule immersed in control (neutral, pH 7) (red) and specific target (blue) pH (acidic, pH 3). The rapid increase in capacitance represents buffer inflow and contact with the sensors, due to coating dissolution. (n=2).

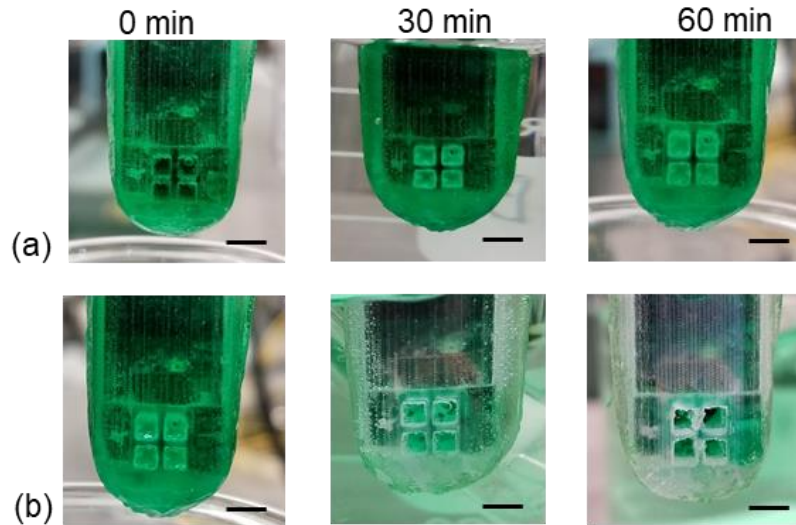


Figure 3-12 Progression of polymer coating throughout (a) control and (b) pH-based dissolution tests. Beginning, 30 minutes, and 1 hour immersion periods are from the left, middle, and right, respectively. Scale bar = 3 mm.

In this section, I described efforts to characterize the capsule coatings toward targeted fluid sampling in pH-specific regions. This was performed using our microelectronics system in a capsule platform, and was directed toward understanding the time scales achievable with different coatings thicknesses as well as different coating varieties through different pH sequences, i.e. from acidic to neutral, neutral to acidic, or a combination of neutral-acidic-neutral. This will be used toward sensing more specific molecules of interest, such as those present in the duodenum, while at target regions as described in chapter 4.

### 3.4 Mechanical Testing

An additional feature considered for evaluating packaging efficacy was determining failure points for mechanical fracture. While the forces present during human peristalsis are relatively low, it is still important to perform some basic tests on the capsule to ensure it can withstand them [117], [118]. These forces vary significantly in the literature regardless of the GI region, ranging from 0.2 N in the duodenum to a high of 20.5 N during gastric emptying [198]–[200]. However, these forces can vary depending on the structure of the probe, and one work presents these forces through the scope of a magnetic pill, reporting significantly lower values than with this type of probe [201]. While the tensile strength of the material I used – i.e. the MED610, 50-60 MPa – suggests it can withstand these forces, the structural integrity can vary based on features such as the layer thickness and number of layers used. Further, the capsule’s structure is inherently non-symmetrical, with the longitudinal length at 30 mm and axial length at 11 mm, thereby altering the contact surface area with the tissue and therefore the force distribution throughout the capsule body.

To produce a basic evaluation of the force required to fracture the assembled capsule, a load frame was set up to apply force by compressing the capsule on either side from multiple axes. For each test, the 3D printed capsule bottom and top components were bonded together along the perimeter using epoxy (Devcon, Danvers, MA), then allowed to set over 24-hour periods to ensure complete curing. A diagram of the axes tested can be seen in Figure 3-13a below.

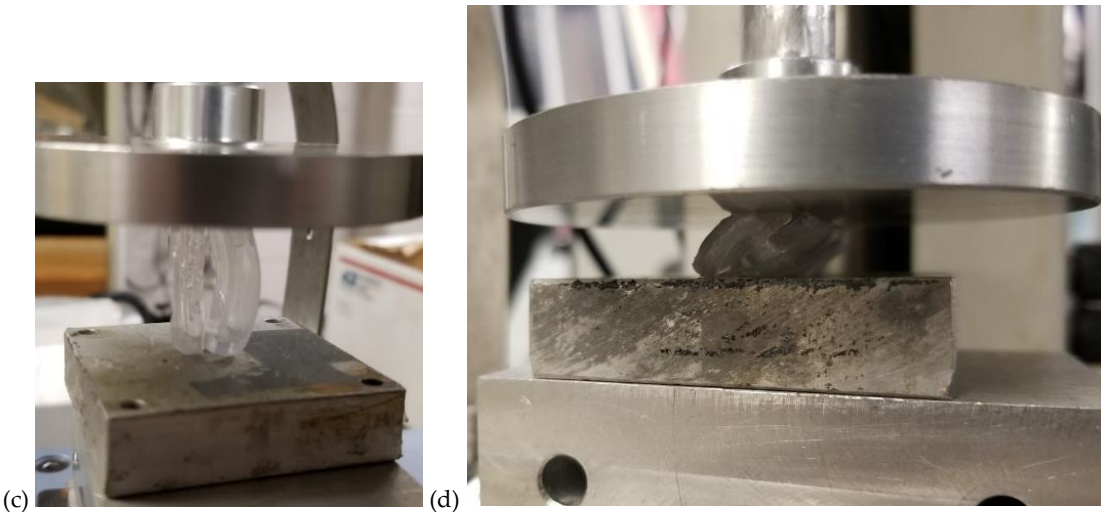
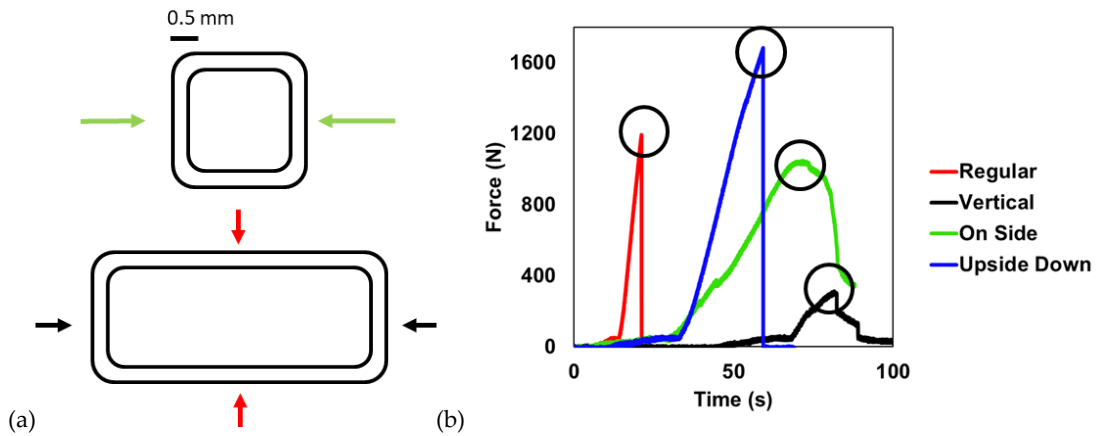


Figure 3-13 (a) Diagram illustrating the regions along each axis where pressure was applied along the load frame. The colors are used for reference in (b) the applied force profiles for each setting. The failure point for each is indicated with each black circle. (c-d) Representative photographs of the capsule package upon reaching failure more for “vertical” and “on side” setups, respectively. (n=1 for each condition).

Figure 3-13b depicts each force profile generated with an Imada model MX 500 load frame with a Z2H-440 2 kN load cell that has a load resolution of 0.1 kg

(Northbrook, IL), performing flexural tests with assistance from Mr. Nelson Quispe. As indicated with each circle, the failure points for each condition corresponding to the applied points in (a) were ~1189, 1681, 1040, and 301 N for the “regular”, “vertical”, “on side”, and “upside down” positions, respectively, each of which far exceed the ranges anticipated during peristalsis. Figure 3-13c-d shows representative photographs of the failure modes for some of the setups, in which I observed failure points along the edges where the capsule surface had been epoxied. This was critical to understand asymmetries in the capsule assembly, which can ideally be improved through more robust and precise alignment procedures.

In this section, I determined potential failure modes for the capsule structure when stress is applied from different axes. While the failure force for each configuration exceeds expected values from peristalsis by, at the very least, one order of magnitude, the package rigidity could potentially be modified through more consistent applications of epoxy or other industrial sealants along the edges, and may even increase with the addition of the polymer coatings investigated earlier in this chapter.

### 3.5 Conclusions

In this chapter, I presented our investigation and characterization of packaging materials using a wireless microsystem capable of targeted fluid sampling based on pH-selective dissolution of polymer coatings. Due to the interface with the phone app and usage of off-the-shelf components for the circuit, this system enables a user-friendly and cost-effective means of real-time data acquisition for GI fluid sampling dependent on targeted physiological characteristics. While further testing is critical to

understand the *in vivo* efficacy of the wireless electronics and signal acquisition, the system enables facile real-time evaluation of applied stimuli, which in this work consisted of dynamic pH profiles and their impact on various pH-targeting coatings.

Various limitations were noted during optimization and analysis. The conditions applied to test the coatings consisted of transient pH-sequences, whereas it is critical to test the response of each set of coatings, likely for those with thicknesses produced from 3-4 dip-coatings, over time at each distinct pH (3-7) to determine their respective abilities to maintain structural integrity. From a mechanical perspective, future capsule structures will likely be tailored by using fluid flow mechanical simulations to design enhanced inlet geometries that would enable more rapid sampling upon coating dissolution. The plug infill process could be improved to become more precise, accounting for viscosity of the polymer solution to improve uniformity across multiple coatings while continuing to maintain an effective seal. Furthermore, the slopes used to determine sampling rate may be affected by the presence of air bubbles in the sensing chamber, delaying the ability of the buffer solution to contact the sensor surface and thus reducing the accuracy of our assumed sampling rate.

Our future work consists of using additional coating and plug materials that would react with more specific analytes present in GI fluids, such as peptide- or polysaccharide-based coatings which dissolve in response to digestive enzymes from pancreatic secretions. This platform will be adapted to have multiple sampling and sensing chambers, individually coated with a variety of biomarker-specific materials toward multiplexed and specific biomolecular identification and therefore enhanced utility and customization for diagnosing different GI pathologies.

## 4. Chapter 4: Biochemical Capacitive Sensing with Triglyceride Films and Module Integration into Capsule System

### 4.1 Capsule-Based System Integration

In revisiting Table 1.1 and Table 3-1, various enzymes that play important roles to GI health are only present in specific regions, which can be targeted based on environmental pH. Devices designed to sense the enzyme in its target environment must therefore consider how best to isolate its signals relative to other potential stimuli. These stimuli can be primarily biochemical, such as the presence of other enzymes, ions, or different types of biomolecules, or physical, such as those from peristalsis or general body movement.

The capsule systems discussed previously utilize a variety of technologies for isolating their target signals to achieve specificity. The gas-sensing capsule, for example, utilizes gas-permeable membranes of graphene nanocomposites that are hydrophobic, aiding in phase separation of gas from liquid [12], [13], [100], [202]. The rest of the capsule package, i.e. everywhere without the membrane, is made of a polyethylene shell that remains inert and protects the internal system from the GI environment. Meanwhile, one of the blood-detecting capsules is inherently specific due to genetically engineered *E. coli* that become luminescent in the presence of extracellular heme [102]. These devices as well as capsule endoscopes, however, do not have the challenge of performing functions at specific GI regions, as they are intended to function throughout the entirety of the GI tract. This often yields higher power requirements, which can lead to battery exhaustion if the operation time exceeds its limits, such as during capsule retention, therefore preventing procedural completion

[16]. When targeting markers that are only accessible in specific regions, the capsule does not need to function in irrelevant regions. Therefore, ensuring the device is only operating when certain environmental conditions are met, i.e. reducing the operation interval, can aid simultaneously in minimizing power consumption and nonspecific interference.

Chapter 3 of this dissertation highlighted the portion of this work involves adapting a capacitive sensing system to know when the pH of the local fluid reached a certain level within the context of a capsule-package. Because the focus application of this dissertation is detecting pancreatic enzymes in the GI tract, system operation is confined to targeting pancreatic secretions after passing through the stomach, which possesses a pH of 1-2.5 and rises in the duodenum and small intestine to neutral levels according to Figure 3-2. In this chapter, I discuss our efforts to adapt our system to specifically sample secretions mimicking duodenal contents and subsequently measure pancreatic lipase and the impact of additional biomolecules that would be present. The system is low-cost, biocompatible, and easily interfaces with a mobile phone for wirelessly collecting data via BLE. The system offers promise for further development of ingestible diagnostic systems that would benefit from novel integration and packaging strategies for measuring biomarkers in GI secretions.

#### 4.2 Pancreatic Lipase Sensing Strategies

Pancreatic lipase (PL), as discussed throughout this work, is an essential hydrolytic enzyme for digestion and absorption of consumed triglycerides. Though other digestive lipases, such as gastric lipase (GL), also provide this capability, PL has a much higher specific activity – 10,000  $\mu\text{M}$  of free fatty acids (FFAs) compared to

1000 uM for PL and GL, respectively – thereby contributing more potency and nutrient release [16]. Table 1-1 describes the various pathologies in which it becomes compromised, such as pancreatitis (both acute and chronic), adenocarcinoma, and general pancreatic insufficiency (umbrella label for reduction in pancreatic digestive enzyme activity), but may also occur in those suffering from cystic fibrosis or celiac disease [1], [2], [65], [82], [203]–[205].

Traditional means of PL evaluation are achieved most commonly using blood samples, though they can occasionally be tested in stool samples as well [206], [207]. Alternatively, PL can be measured directly from pancreatic secretions, collected through methods such as direct pancreas function testing (PFT) or endoscopic PFT. The prior utilizes an oroduodenal tube for access, then pancreatic stimulation via injection of hormones secretin or cholecystokinin (CCK). Unfortunately, this process is not standardized and the range is dependent on the center in which it is performed [208], [209]. Additionally, while exocrine insufficiency is more likely to become apparent during late stages of conditions like PA, it often contributes to malnutrition that can lead to a poorer prognosis even with surgery [210]. This implies, and has been shown, that treatments for exocrine insufficiency, i.e. pancreatic enzyme replacement therapy, can improve outcomes for PA patients [211]. Improving methods for monitoring exocrine insufficiency are therefore likely to aid in this process.

Blood tests for lipase begin with centrifugation to extract the serum, then tested through a variety of methods such as colorimetric assay (570 nm wavelength absorption proportional to enzymatic activity) or titrimetric (pH of the solution indicates the extent of reaction). Pancreatic fluid samples, on the other hand, are only used to analyze

electrolyte concentrations due to accuracy limitations for enzyme measurements. These concentrations are determined using clinical chemistry autoanalyzers, which generally rely on ion-selective electrodes and measured voltage differences with varying concentrations of ions [209], [212], [213]. As a result, blood tests are chosen as the gold standards for lipase analysis, though are only useful when the condition severity requires stronger treatment.

Novel methods for lipase detection have been emerging to improve upon current standards through features such as increasing accessibility and functioning with different sample types by removing required separation steps or hardware [214]. One sensor based on surface acoustic waves (SAW) monitored the frequency shift based on a change in solution conductance proportional to the lipase concentration. The solution conductance changed due to release of fatty acid from a triolein substrate [215]. Another sensor used screen-printed electrodes with immobilized Prussian Blue – which reacts with  $H_2O_2$  resulting from glycerol, a hydrolytic byproduct of triglycerides and lipase, and  $NAD^+$  after reacting with NADH oxidase – for measuring the lipase concentration via amperometry [216]. However, these processes are relatively indirect and require either multiple reagents or highly specific conditions, likely limiting their ability to function as intended if immersed into GI secretions.

Mirsky et al., however, describe an alternative scheme using short-chain and long-chain phospholipid substrates over gold capacitor electrodes to measure hydrolysis from phospholipase activity. The hydrolysis causes the substrate to become water soluble, thereby desorbing from the electrode surface into aqueous phase and increasing the electrode capacitance [217]. This strategy measures a more direct result

of the lipase activity, which may translate better to *in situ* environments. Furthermore, the strategy is readily adaptable to our microelectronics system developed in chapter 3 of this thesis.

However, the human duodenum is a host to not only pancreatic enzymes but incoming contents from the bile duct, specifically bile acids (BA). BAs are synthesized from cholesterol by hepatocytes; they are shown to be elevated in GI secretions during BA malabsorption and can be further related to conditions such as irritable bowel syndrome-associated diarrhea and colorectal cancer [218]–[220]. Because of their amphipathic nature, BAs such as cholic and deoxycholic acid act as natural detergents that emulsify triglycerides to form micelles through intercalation, aiding their digestion by PL into absorbable monoglycerides and fatty acids [221]. Below, I describe our efforts to not only measure pancreatic lipase activity based on its ability to cause a triglyceride substrate to dissolve, but to characterize our system by testing our film with BAs to determine potential nonspecific impacts and how it may affect sensing of PL.

### 4.3 System Setup

#### 4.3.1 Film Deposition

The sensing mechanism is based on the enzymatic and physicochemical reactions presented in Figure 4-1, which features (a) the hydrolysis of triglyceride ester linkages by PL and (b) the emulsification of triglyceride globules by BAs. Stearin was used as a model triglyceride due to its high melting temperature range (54–72.5°C) to remain stable at physiological temperature (37–39°C). The triglyceride used consist of a mixture of stearin and glycerol (SG), where several different ratios were tested. The

combinations tested include stearin, 2:1, 1:1, and 1:2 of stearin:glycerol after allowing to melt in a 100°C water bath prior to deposition. Multiple strategies for film deposition onto the sensors were tested, as depicted in Figure 4-2. The films used for testing with GI species were deposited via dip-coating of the sensor-PCB assemblies (SPAs, discussed in Section 3.2.3), depicted in Figure 4-2b. The SPAs were pre-heated for 5 minutes to above substrate melting temperature (~100°C), then immersed and subsequently removed at ~10 mm/s. The films were air cooled at ambient forming SG-coated SPAs (SG-SPAs), and resulting thicknesses were measured using calipers.

The SG-SPAs were inserted into the capsule via the assembly process in Figure 4-3, and the capsules were subsequently dip-coated into in pH-sensitive copolymer solution, depicted in Figure 4-2c. The copolymer solution utilized for this study was 30% Eudragit L100 in methanol, producing coatings  $783 \pm 60 \mu\text{m}$  thick using a previously described coating process[195].

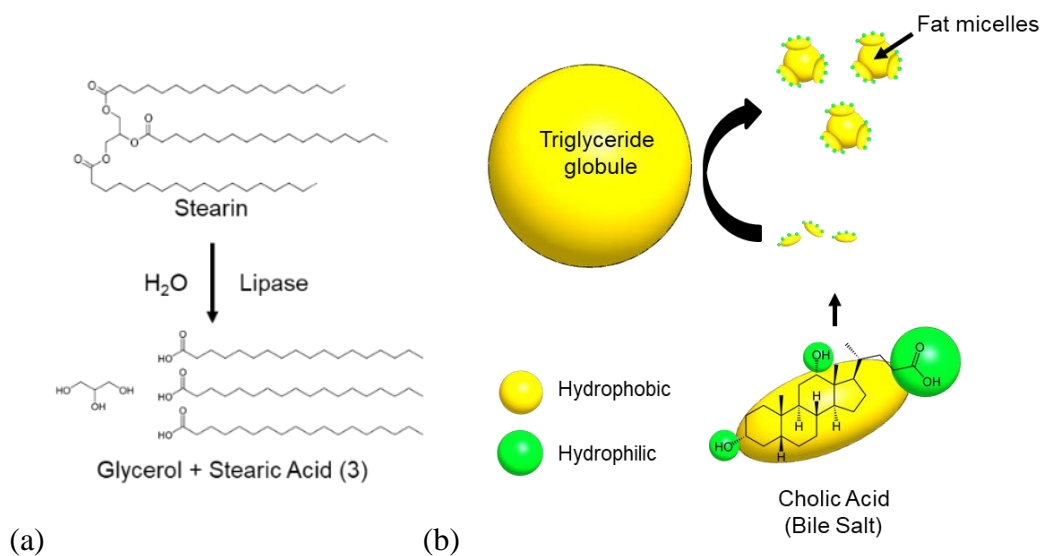


Figure 4-1 (a) Lipase-induced hydrolytic digestion of stearin into glycerol and three stearic acid molecules. (b) Bile salt-induced emulsification of triglyceride globules into micelles.

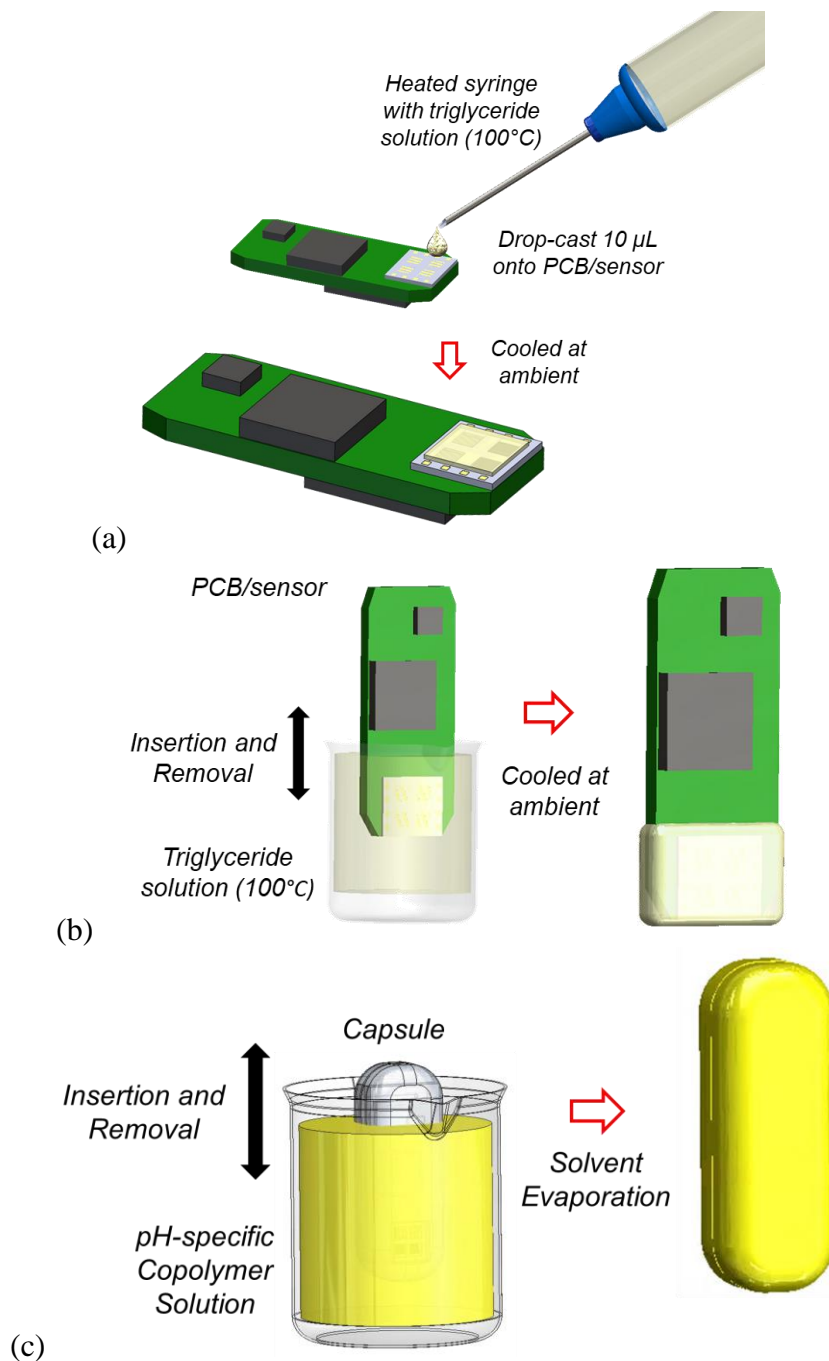


Figure 4-2 Deposition strategies for obtaining TG films over sensors: (a) drop-casting and (b) dip-coating of molten TG solution while the substrates were either left at ambient or pre-heated to TG melting temperature for 5 minutes. (c) Dip-coating of assembled capsules into dyed pH-sensitive copolymer solutions to form GI-targeting coatings, repeated for sequential coatings.

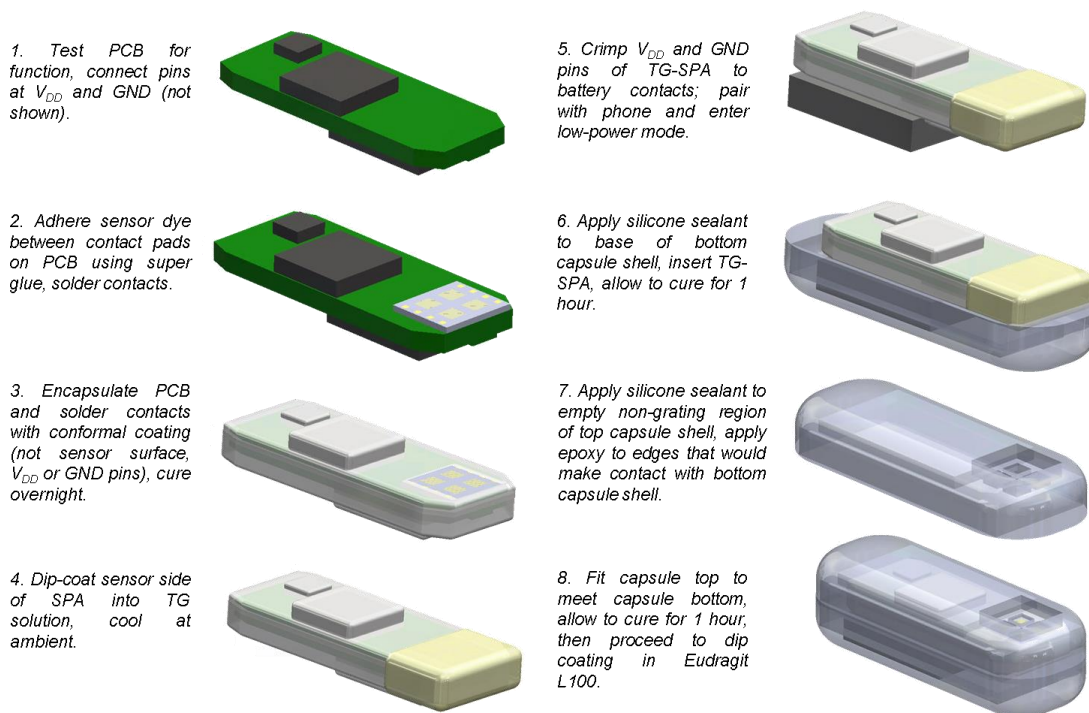


Figure 4-3 Assembly process for platform. Steps 1-4 used for sensor characterization of TG-SPAs with connection of  $V_{DD}$  and GND to external power supply, while Steps 5-8 are used for testing complete capsule. At Step 5, after connection to Lithium polymer battery. Deep Sleep mode is entered for a 3-hour time period via transmitted signal to allow for curing of adhesion and coating materials at respective steps. After Step 8, capsule electronics enter Active mode to enable capacitance measurements and signal transmission to mobile phone.

#### 4.3.2 Sensing Characterization

SG-SPA characterization was performed while powered by an Agilent E3631A DC power supply (Santa Clara, CA). For the SG-SPAs prepared in Section 4.3.1, each experiment was initiated with baseline measurements while the device was suspended in air. After 5 minutes, the devices were lowered into a 50 mL beaker containing solutions of either negative control – i.e. buffer only – then subsequent test conditions, described below. All buffer solutions consisted of 40 mL of 0.1 M phosphate buffered saline (PBS) on a hot plate set to 300 RPM stir via magnetic stir bar to equilibrate the solution and temperature at 39°C. All solutions were prepared using deionized water

from E-pure Ultrapure Water Purification Systems (DIH<sub>2</sub>O; resistivity=18.0 Ω-cm; Thermo Scientific, Waltham, MA).

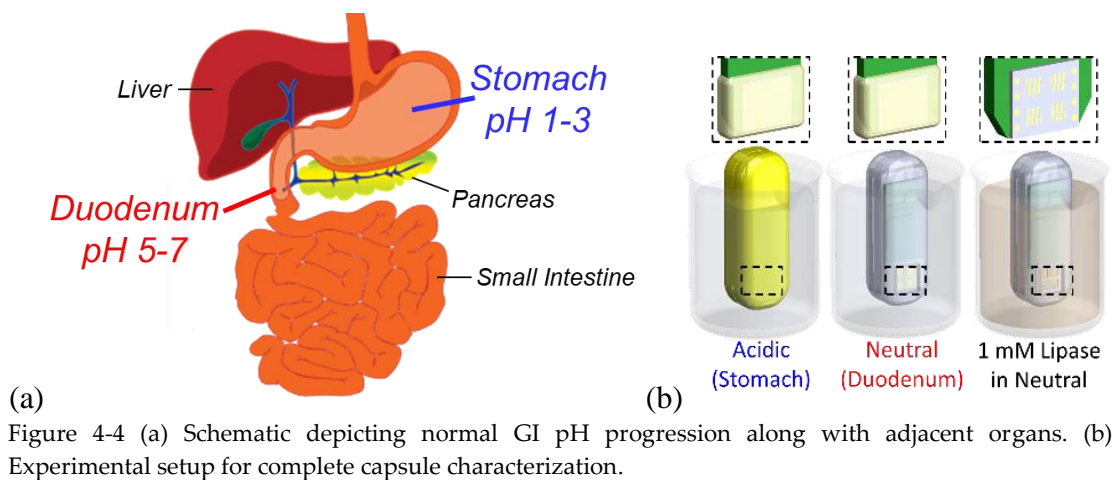
The sensor capacitance response was determined for each analyte in an environment that simulated fluids present in the duodenum. SG-SPAs were immersed in pH 7.3 buffer containing varying concentrations of either porcine PL or a BA mixture of sodium cholate and sodium deoxycholate (Sigma Aldrich, St. Louis, MO). PL was tested at 1 mM, 100 μM, and 10 μM concentrations, while BA was tested across 7, 0.7, and 0.07 %w/v. To measure potential impact of nonspecific enzymes, porcine pancreatic trypsin (Sigma) was also tested alone at 100 μM, a concentration that exceeds maximum expected outputs by >250 % [222]. Each solution was incubated for 30 minutes at 39°C prior to insertion into a beaker for testing the SG-SPAs to ensure complete solubility.

#### 4.3.3 SEM Analysis for Film Morphology

Pre-heated sensor die were inserted into molten 2:1 SG solution prepared as described in Section 4.3.1. The sensors were then cooled at ambient (23°C) for 24 hours, then incubated in glass petri dishes containing PBS (0.1 M) alone or with either 100 μM PL, 0.7 %w/v BA or 100 μM trypsin, respectively. Each solution was maintained at 39°C under 300 rpm stir. Sensors were removed from solution after either 30- or 60-minutes, rinsed with DIH<sub>2</sub>O, dried for 24 hours, then prepared in a carbon coater to deposit coatings of conductive carbon (MED 010 Balzers Union Carbon Coater, Balzers Union, Liechtenstein). The samples were then viewed under a Hitachi S-3400 scanning electron microscope (SEM).

#### 4.3.4 pH-Dependent Sampling and Sensing

Following a similar procedure as in Section 4.3.2, measurements were initiated while suspending the coated capsule in air and powered by a Li-polymer battery (Powerstream, West Orem, Utah). The capsules were then sequentially inserted for a duration of 25 min into several solutions, which mimicked the pH transition between the stomach (acidic) and duodenum (neutral), as depicted in Figure 4-4. The solutions consisted of the following conditions: (i) 0.1 M acetic acid (pH 3), (ii) PBS (pH 7.3), and (iii) 1 mM PL in PBS (pH 7.3). This sequence was chosen to reflect the capsule transit throughout the GI tract with the subsequent presence of a specific biomarker residing in the SI, in this case PL.



#### 4.4 Results and Discussion

This work presents a sensing strategy using triglyceride films to detect duodenal contents, such as lipase and bile acids, in a wireless capacitive-sensing platform. The sensors were designed to measure the capacitive response when fluid enters the sensing chamber. Under biological stimuli from species in the environment, the substrate films deposited over the sensors would undergo reactions, such as hydrolysis or

emulsification, that alter their dielectric property. Gradually, the dissolution of the film substrate exposes the electrode fingers to the infiltrating fluid, causing an increase in capacitance. The sensor capacitance was measured for SG-SPAs and coated capsules inserted into various solutions containing biochemical stimuli that would induce changes in capacitance over different lengths of time when compared to non-specific controls or buffer alone.

Stearin was the material chosen as our model triglyceride, as described in B. Triglycerides, in general, are significant to traditional human diets, and its digestion is enabled due to emulsion and subsequent hydrolysis by BAs and PL, respectively. Due to its rigidity and low water solubility – an effect of having longer chain fatty acids – unmodified stearin is an inefficient substrate for hydrolysis. Other triglycerides such as oleic acid – a shorter chain fatty acid found in olive oil – are used as standard substrate for lipase assays; however, these substrates are incompatible with our system function in the small intestine due to having a melting point below physiological temperature [223]. Previous reports modify stearin as a substrate using suspensions with glycerol by enhancing the quality of the interface it would have with lipase [224]–[226]. Lipase activity on triglycerides is generally dependent on the surface area, which increases significantly with rougher surfaces or when emulsified into micelles by BAs. While crystalline stearin films are naturally hydrophobic, glycerol is hydrophilic due to polar –OH groups, enhancing the interface between the species in solution and the film substrate, as well as a stable film deposition and adhesion over the sensor surfaces.

Because the platform has demonstrated utility for monitoring changes in sensor capacitance ( $C$ ), I could characterize dielectric properties of the films through estimation by Equation (9):

$$C = \frac{2\varepsilon_r\varepsilon_0lwn}{d} = \frac{\varepsilon_r\varepsilon_0A}{d} \quad (9)$$

This is similar to equation (7) back in Chapter 2, where it uses  $\varepsilon_0$  (vacuum permittivity),  $\varepsilon_r$  (dielectric constant),  $l$  (finger length),  $w$  (finger width),  $n$  (numbers of electrode fingers), and  $d$  (distance of separation), where  $2lwn$  can be simplified to  $A$  (total area of both electrodes). Therefore, changes in the dielectric properties of the films are proportional to measured capacitance ( $C$ ), and indicate the extent of hydrolysis or emulsification of the substrate over the sensor. To account for changes in baseline capacitance between experiments, I presented sensor response as the percent change in capacitance ( $\% \Delta C$ ), which is calculated with equation (10):

$$\% \Delta C = \left( \frac{C_n - C_1}{C_1} \right) * 100 \quad (10)$$

When no film is present – i.e. one of our negative controls – and the sensor is inserted into PBS, the mean  $\% \Delta C$  is  $39.5 \pm 1.4$ , likely a resulting effect of increase in dielectric constant combined with ionic reactions with the  $\text{SiO}_2$  films, which can be mitigated in the future through more inert films [227]. As expected, insertion into molten and cooled SG solutions produced negligible  $\% \Delta C$ , indicating that changes in capacitance are limited to (1) when the SG material is influenced by an environmental condition – such as the applied solutions and constituent analytes described in C – and (2) due to downstream effects on the  $\text{SiO}_2$  films once the insulating integrity of the SG films becomes compromised, though this latter condition is not studied further here.

I first tested the effect of different deposition strategies of the SG solutions onto our sensors, depicted in Figure 4-5. Drop-casting and dip-coating of molten SG solution, while the substrates were either left at ambient or pre-heated for 5 minutes to SG melting temperature, were compared. Substrate temperature was considered a significant factor due to its effect on surface tension, and therefore wetting of the solution [228]. In the case of drop-casting, three phases (i.e. solid, liquid, gas) are present at the sensor surface during the entirety of the process, thus surface tension becomes a more dominant factor for wetting, and therefore coating, the sensors. Wetting through dip-coating, however, causes most of the sensor surface (except for the edges) to be exposed to only two phases with the ability for a complete wetting and sealing layer, reducing the dependency on surface tension. Additionally, the order of the wetting transition has a direct impact on the adsorbed film thickness, such that the greater the discontinuity in the interfacial energy between phases, the greater the thickness. This discontinuity is reflected by the difference in temperature between the substrate and film, which I observed through thinner films produced when the substrates are pre-heated. Additionally, the SiO<sub>2</sub> films on the sensor surfaces are generally hydrophilic, with surface energies of  $\sim 73.8$  mJ/m<sup>2</sup>, compared to most triglycerides, which maintain surface energies ranging from 25-30 mJ/m<sup>2</sup>; this increases with temperature as well, producing further discontinuity and, therefore, wetting angle [229], [230]. Adhesion between the SiO<sub>2</sub> and SG layers is primarily based on van der Waals interactions; however, I found that the drop-casted films were not stable, and failed to prevent buffer from interacting with the sensors (data not shown) [231]. After comparing the efficacy of the film deposition methods, SG-SPAs were

tested using films produced through pre-heating the substrate to 100°C and dip-coating, which yielded an average film thickness of 210±60.3 μm. The total sensor area was 0.06 mm<sup>2</sup>, indicating each film volume over the sensors to be 1.25x10<sup>-5</sup> cm<sup>3</sup>. In comparing the sensor response for different SG film compositions (see C), I found the 2:1 SG ratio films to be most stable when in buffer alone (Figure 4-6), hence their implementation in the following sensor characterization experiments. From the 2:1 SG ratio, I could calculate the volume of stearin contained within the film to be 0.84x10<sup>-5</sup> cm<sup>3</sup>, and with a density of 0.862 g/cm<sup>3</sup>, the stearin mass was found to be 0.724x10<sup>-5</sup> g, or 8.12x10<sup>-9</sup> mol (molecular weight of stearin:891.5 g/mol).

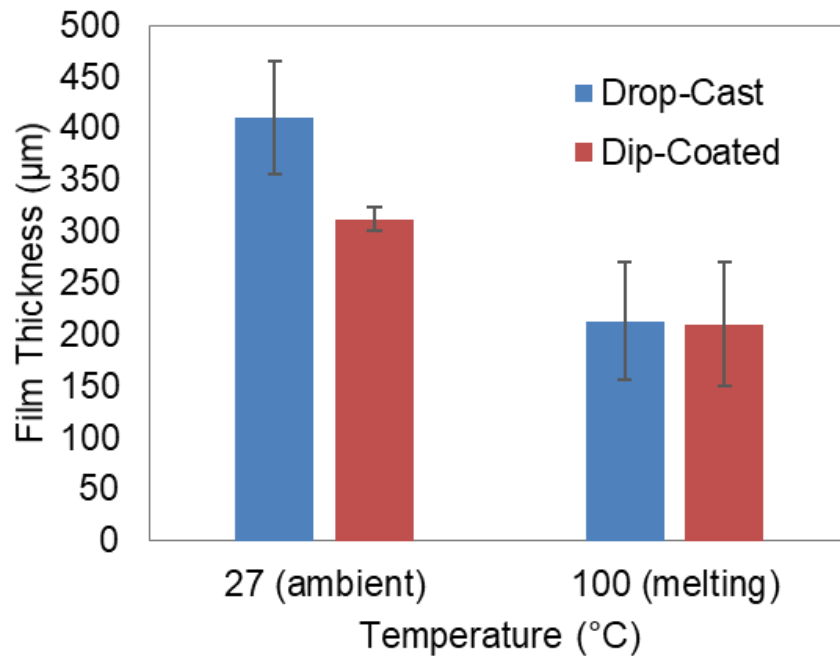


Figure 4-5 Resulting thicknesses in films with each deposition strategy and initial SPA temperature. Error bars depict standard deviation (n=3).

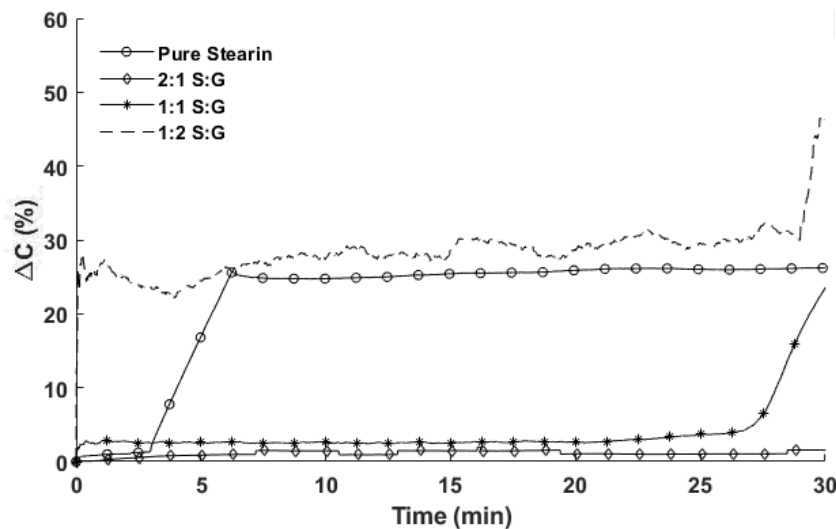


Figure 4-6 Representative sensor response testing after insertion of TG-SPAs into buffer solution (0.1 M PBS) when TG film composed of either pure stearin or stearin:glycerol (S:G) ratios of 2:1, 1:1, or 1:2. Film most stable, i.e. least response over time, with the 2:1 S:G ratio compared to other compositions. (n=2).

The standard concentration of PL expected in healthy unstimulated duodenal fluid ranges from 1-10  $\mu\text{M}$  [232]. Conversely, average duodenal secretions contain 0.7 % w/v BA, which reflects the median concentration tested in this work [233]. Because PL is dependent on BAs for improving the enzyme-substrate interface with triglycerides, it was necessary to determine the individual effect of both species on the dielectric properties of the film, which can range from characteristics such as ratio of stearic acid to glycerol via hydrolysis, stearin to glycerol through emulsion separation, or even overall SG film to solution contact with the sensor surface. Figure 4-7 presents the capacitive response ( $\% \Delta C$ ) of the SG-SPA over time upon immediate insertion into the solution at  $t=0$  minutes, where the concentration of the biological stimuli was varied for PL (0.01-1 mM) and BAs (0.07-7 % w/v), as well as pancreatic trypsin (100  $\mu\text{M}$ ) to measure potential nonspecific interactions. However, it must be noted that these are representative trials and more runs are required to determine film robustness and reliability to different concentrations of lipase. Each sequence begins directly following

insertion of the SG-SPA into the test solution. Measurements were compared to a buffer-only solution (7.3 pH, PBS) as a negative control. The capacitance responses of films to both PL and BAs produced trends that altered proportionally to the concentration of the analytes present. The measurement was conducted over the course of 40 minutes, consistent with the expected transit time of most contents passing through the duodenum, though longer time scales have been reported [234]. Additionally, nonspecific activity testing with extracted duodenal secretions and its regular contents will be necessary for increasing confidence in sensor specificity, though stearin appears to be a resilient insulator to negative controls. To modify the system for response to lower concentrations, it is likely that parameters such as concentration of substrate at the sensor surface or film thickness will need to be reduced such that the dielectric properties of the film can change faster. This is consistent with our findings where films exceeding 200  $\mu\text{m}$  thickness produced no significant change in capacitance compared to buffer alone (data not shown), indicating that increasing film thickness may reduce reactivity or penetration of the enzyme. Reducing the film thickness would be feasible through closer matching of the surface energies, such as through temperature or surface tension, between the SPAs and SG solution before dip-coating, as well as dissolving the triglyceride in nonpolar solvents such as ethers, hexane, or chloroform in lower concentrations [78], [235]

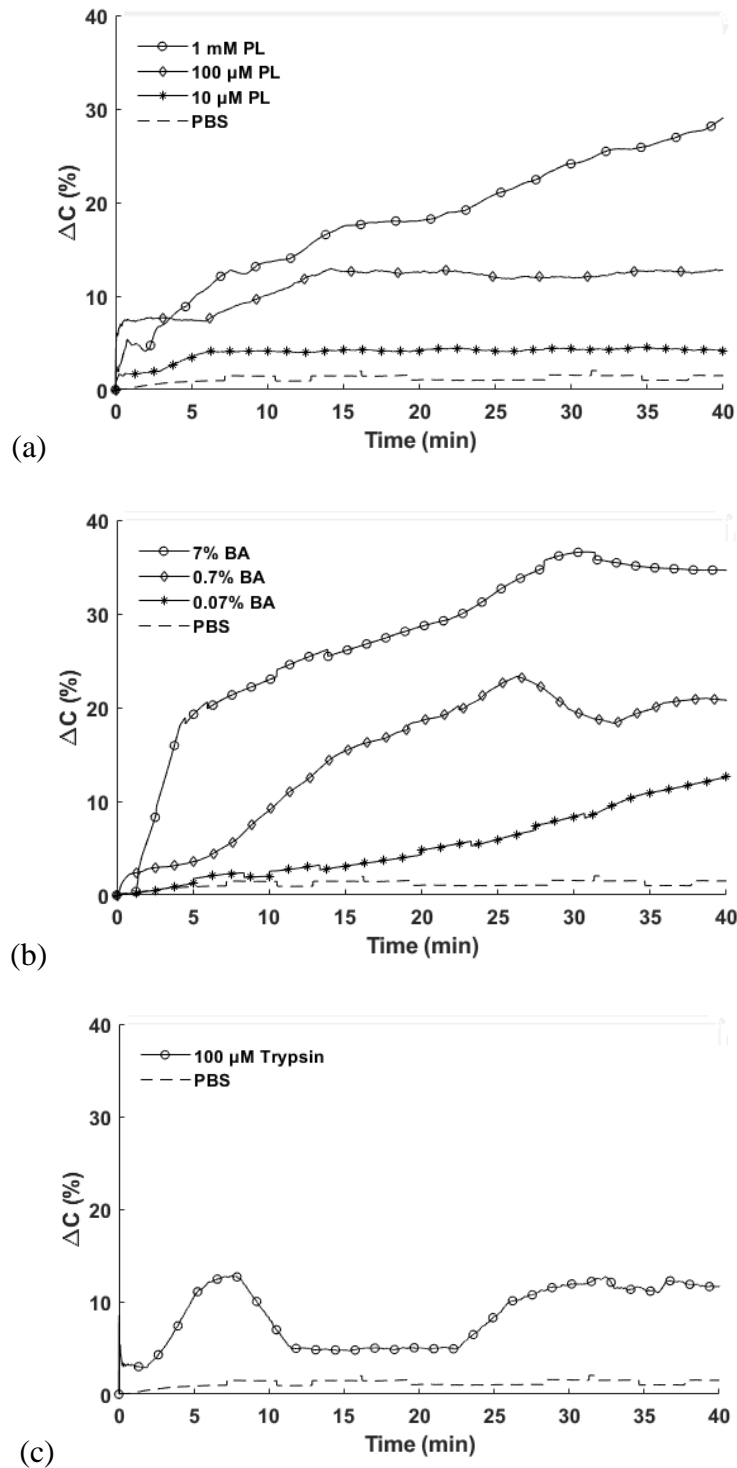


Figure 4-7 Sensing in the presence of different biochemical species at varying concentrations. (a) PL, (b) BAs, and (c) pancreatic trypsin.

After measuring the capacitive response to each concentration, I used the slopes of the capacitive response for the first 30 minutes of sampling ( $\% \Delta C / \Delta T$ ) as a metric

to fit the sensitivity. While we cannot model the data without more trial runs in future works, this provides insight as to the kinetic efficacy of each analyte to the substrate, which may change due to the difference in reactive mechanism for each analyte, i.e. hydrolysis and emulsification for PL and BAs, respectively. For example, hydrolysis via PL produces glycerol and stearic acid, each of which impact the capacitance of the sensor interface at both the SG and SiO<sub>2</sub> films differently. Alternatively, emulsification does not alter the material chemical composition, merely the particle size and therefore phase properties of the film, allowing enhanced exposure of the SiO<sub>2</sub> films and subsequently electrode surface to constituents in the environmental fluid, even those such as divalent cations [236]. These results produce insight as to the existence of potential differences in the dielectric impact between hydrolytic and emulsion kinetics, though further investigation is required to yield specific electrochemical effects of GI analytes on these individual materials.

Morphological differences comparing the impact of each species on the SG films were viewed under SEM (110x magnification), after deposition of a carbon coating for conductivity. The films had been incubated under stir condition to each solution, and removed at two time points, 30 minutes and 60 minutes, as shown in Figure 4-8. The 30-minute time point was used to correspond the film morphology to the endpoints of the  $\% \Delta C / \Delta T$  values used earlier, while the 60-minute time point was used to determine if any significant changes in the film morphology occurred beyond the used duration. Here, I observed little difference between the samples exposed to either PBS or trypsin, whereas the surfaces for PL and BA indicate significant qualitative changes in roughness and crystallization, respectively. For the PL-exposed

sample, the surface appears significantly smoother, likely an effect of the hydrolytic interface occurring between PL and the stearin that reduces surface roughness, and therefore interfacial surface area, until eventual saturation. The BA-exposed sample, however, presents the formation of an increasingly fragmented stearin surface, offering insight as to how hydrolysis and emulsification manifest differently on the substrate. Based on the capacitive changes observed in Figure 4-7, these structural changes may be direct indicators for changes in either dielectric properties of the film material or, through emulsification-induced fragmentation, surface area of the underlying electrodes to the high-dielectric behavior of the buffer. The lack of significant change between the 30- and 60-minute time points also imply that the durations used are enough to correspond signal saturation to the morphological state.

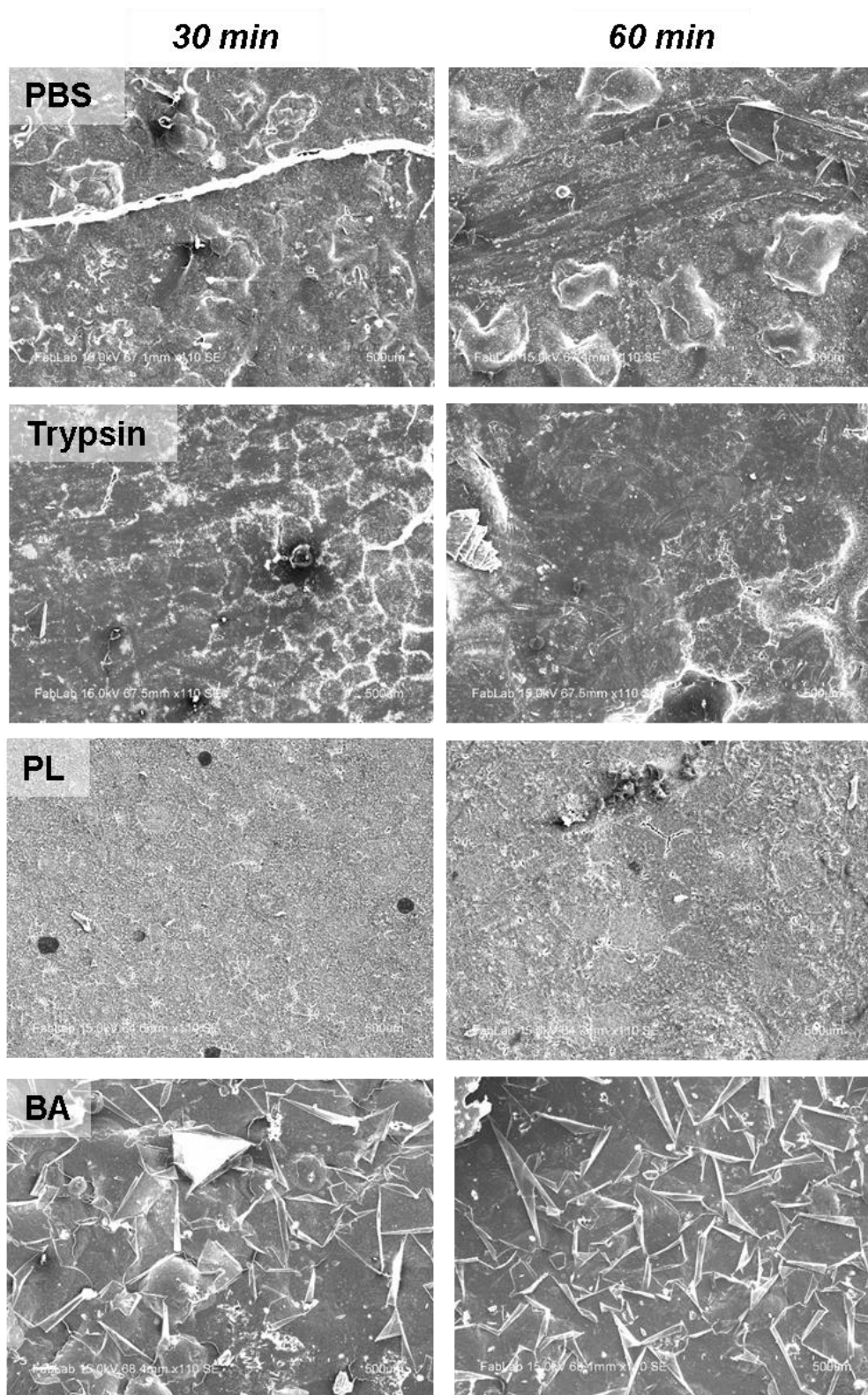
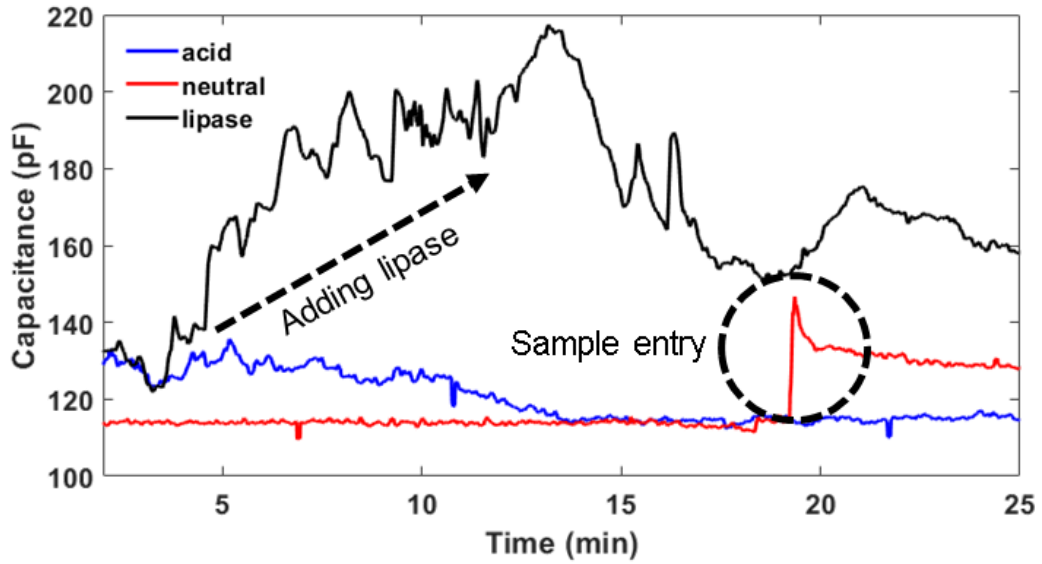


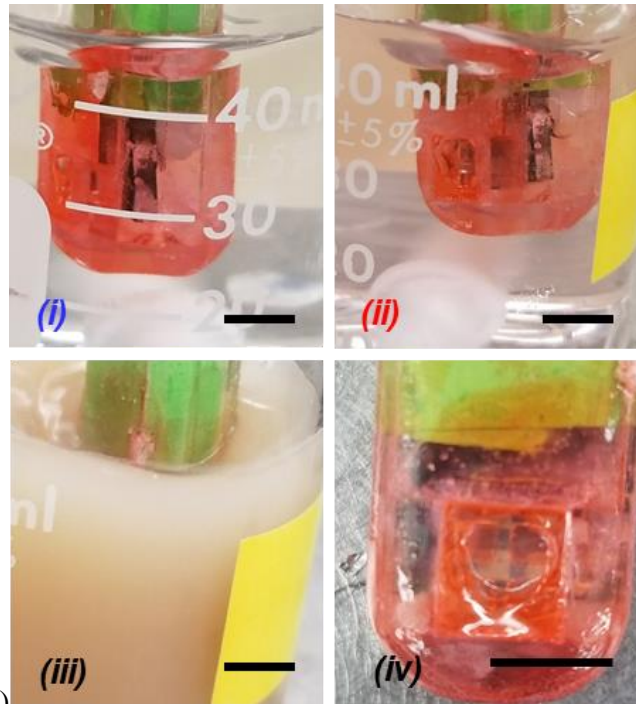
Figure 4-8 Representative SEM images for characterization of SG films after exposure to various solutions at 30- and 60-minute time intervals. (n=3).

Finally, I tested the ability to measure PL within the capsule to simulate detection in the duodenum environment. Figure 4-9 presents the result of testing the coated capsule containing the SG-SPAs for performing pH-targeted sampling. The respective conditions are labeled as *acid*, *neutral*, and *lipase*, where the capsule was inserted into a pH 3 solution (0.1 M acetic acid) to represent acidic contents for the stomach, pH 7.3 solution (0.1 M PBS) for the duodenum, and addition of PL (1 mM PL in 0.1 M PBS) as a target analyte, respectively. Here, the sensor responses are overlaid for more direct sequence comparison, and presented in capacitance rather than  $\% \Delta C$  to show how they compare from beginning to end of each condition. Upon insertion into the *acid* condition, I observed negative drift from  $\sim 129.5 \pm 0.772$  pF, eventually saturating at  $115.2 \pm 0.759$  pF, though no inflow of solution into the capsule was evident through visual inspection and the color of the buffer solution remained clear as indicated in Figure 4-9b-I [195]. After  $\sim 19$  minutes of incubation in the *neutral* condition (0.1 M PBS), a distinct increase in capacitance to 146.1 pF was observed, before reaching saturation at  $127.9 \pm 0.433$  pF. Additionally, the color of the solution gained a red hue reflective of the Eudragit L100 coating color, as seen in Figure 4-9b-ii, indicating sample entry. Once the capsule was inserted into the *lipase* condition, I observed an immediate effect similar to the capacitance sequences observed in Figure 4-7a, where there is a rapid increase in capacitance over  $\sim 14$  minutes to reach  $216.0 \pm 0.602$  pF, or 66.8% increase from the beginning, with some signal fluctuation and decrease as well until it levels around  $158.5 \pm 0.913$  pF, or a 22.4% increase. Due to the opacity of the PL solution, I did not discern any distinguishable features until

capsule removal, where there is a noticeable region in the Eudragit L100 coating where the fluid could enter the capsule sensing chamber, shown in Figure 4-9b-iv.



(a)



(b)

Figure 4-9 (a) Combined pH sampling and enzyme sensing in integrated capsule. Measurements were initiated after immersion into acidic solution for 25 minutes (blue), after which the capsules were removed and immersed into a neutral solution (red), where a spike was observed around 19 minutes, indicated by the circle. Finally, the capsule was removed and immersed into a solution containing 1 mM lipase (black), where a distinct increase in capacitance is observed, indicated by the arrow. (b) Photographs taken of the capsule at the end of each respective sequence, designated by the label color: b-i: acid condition, b-ii: neutral condition, b-iii: lipase condition, and b-iv lipase condition after removal from the solution. (n=1).

I then calculated the slope from the first 30 minutes of the *lipase* condition to yield 0.198 pF/min. Comparing the linear fits of the slopes show changes with concentration of PL. This slope is expected when the concentration is ~160  $\mu\text{M}$ , even though the applied concentration was 1 mM. This is calculated as a 6.25-fold loss in sensor response, indicating loss in SG-SPA response to the analyte when packaged within the capsule rather than when tested without it; this is not surprising, though, considering the differences in fluid dynamics and flow profile of the analyte in the sensing chamber as opposed to when the SG-SPA is surrounded by the fluid in the beaker. However, this emphasizes the need to enhance the exposure of the SG-coated sensors to the surrounding environment, which can be implemented by reducing the thickness of the 3D-printed shell at the inlets or by embedding the sensors directly onto the outermost packaging of the capsule. Ultimately, this experiment demonstrated the sequential ability of the capsule package to remain intact in a potential gastric environment, dissolve from duodenal fluids and allow detection of PL in the same environment. Based on the results presented in Figure 4-7, it is likely this similar strategy can be leveraged to detect BAs in target pH environments as well, as well as for measuring PL or BA related pathologies such as those discussed above.

In this section, I described our efforts to develop various triglyceride film deposition protocols, including the impact of composition and method on stability, and the subsequent integration into the capsule system and pH-soluble coatings discussed in chapter 3. Further, we gained an understanding of how the sensing response can be applied to both hydrolytic and emulsification reactions, which possess utility for detection of a broader range of targets than initially intended. While further efforts

should be established in enhance specificity to individual reactions at a time, this maintains significant advancements to the potential impact of capsule-embedded sensing technologies.

#### 4.5 Conclusion

This work presents a proof-of-concept demonstration of triglyceride-based coatings for monitoring duodenal analytes in an integrated capsule system. The system can measure and wirelessly transmit changes in capacitance due to both film hydrolysis and emulsification reactions as a result of exposure to PL and BAs, respectively. For PL, I measured signals for 10  $\mu\text{M}$ -1 mM concentrations, whereas for BAs I could distinguish between 0.07, 0.7, and 7 w/v% concentrations, each of which are within physiologically relevant ranges for healthy and abnormal levels. For each concentration, I used the observed slope produced from the first 30 minutes, which is well within the average duration range for material traveling through the human duodenum, to relate the signal to its respective concentration [234]. Furthermore, I characterized morphological differences in triglyceride-based films after exposure to various duodenal contents, giving insight as to the physical manifestation of hydrolytic versus emulsification reaction mechanism. Finally, I demonstrated the ability to detect PL after subsequent targeting at a pH-specific environment, and found that the design of the sensing chamber and the respective inlets could be thinned to prevent reduction in the reactive interface between the sensor surface and environmental contents.

There are several limitations to our methods for signal analysis and the platform in general. For example, parametric analyses of slopes over different time intervals may allow for distinguishing between each film response over time, thus producing more

sensitive or optimal fitting equations to match the concentration with the  $\% \Delta C / \Delta T$ . The sensor responses are also likely to increase sensitivity if the insulating films can be deposited with reduced thicknesses; this would change the amount of substrate and therefore amount of reaction that needs to occur to increase the rate of change in dielectric mismatch between the film and environmental solution, potential altering resulting concentration range for other GI regions where it may be relevant. Next, each species was tested in isolation, and their simultaneous presence has been shown to reduce efficacy due to non-specific film interactions depending on the material used [144]. Therefore, it is critical that future work will focus on characterizing and optimizing the sensor performance over a wider concentration range, adding more non-specific species to determine further reaction specificity, and incorporate additional food-based materials, such as gelatin – substrates for monitoring other types of pancreatic enzymes [144]. Additionally, different capsule coating materials could be used toward measuring these species in different GI environments – based on their pH – as well as enhance the exposure of the substrate to materials in the external environment. Finally, the sensor response can be utilized to trigger the release of on-board actuation mechanisms or drug payloads for feedback-enhanced control over targeted therapies. Ultimately, this platform provides opportunities for sensing hydrolytic and emulsification reactions, such as through other enzymes or biologicals similar to the species discussed in this work, along with an innovative packaging strategy toward passive GI targeting in minimally invasive and ingestible diagnostics.

## 5. Chapter 5: Concluding Remarks

### Highlights

- Electrical characterization of film-based sensing strategy for bioelectronic interfacing
  - Distinguished impedimetric and geometric trends produced from specific and nonspecific film interactions
  - Corresponded impedance trends with enzyme concentration
  - Tailorable for a variety of films for different reactant-substrate interactions
  - Characterized for different sensor geometries
  - Determined potential signal metrics for integrated sensing systems
- Development of coating-based packaging strategy to enable gastrointestinal targeting of microsystem platforms
  - Targeting demonstrated for environments with different pH range
  - Suggestive for targeting gastrointestinal regions such as the duodenum and stomach
  - Adaptable for multi-layered coatings toward dissolution after sequential pH ranges
  - Demonstrated resilience to expected gastrointestinal mechanical forces
- Demonstration of microelectronics sensing system for detecting duodenal targets with triglyceride films
  - Various deposition strategies for triglyceride materials

- Evaluated with dependency on sensor substrate and material composition
  - Characterized morphological changes occurring at the microscale in response to hydrolytic vs emulsification reactions
    - Sensor response similarities between pancreatic lipase and bile acids
  - Reduced response for nonspecific enzymes
- Integration of sensing system within capsule package demonstrates feasibility for pH-specific environmental targeting and subsequent sensing
  - Distinguished between sampling signal and specific marker signal
  - Developed assembly and validation protocols for device function

### 5.1 Summary

This study presents the design and characterization of various critical elements, summarized in Table 5-1, required in integrating sensing and targeting strategies into a capsule platform for evaluating GI health. This work explored a capacitive-based sensing and detection method relying on the reaction of deposited biomaterial films with specific biomolecules, specifically pancreatic trypsin, lipase, and bile acids, within the context of a capsule-sized microelectronics system capable of wireless, real-time monitoring. The first experimental chapter, i.e. chapter 2, described the development of a proof-of-concept method that measured impedance of these films and isolated specific relevant electrical elements that could be used to design a microelectronics system with capsule-sized form factor, and investigated various deposition strategies for integration with traditional microelectromechanical system (MEMS)-based

fabrication processes. Chapter 3 then presents our passive approach to targeting specific GI fluids based on their pH profile. This was achieved using coatings – consisting of copolymers utilized in the pharmaceutical industry for targeted drug delivery functions – that were repurposed for protecting our sensor surfaces in nonspecific pH environments and dissolving, thereby exposing the surfaces, at the regions of interest. Specifically, I tested the ability to sample in acidic ( $\text{pH} < 3$ ) and neutral/basic ( $\text{pH} \geq 7$ ) environments, and used a novel microelectronics capacitive sensing platform, coupled with wireless capabilities for interfacing with a mobile app, to characterize the sensor response when the coatings were implemented over 3D-printed capsule structures used for housing the sensors. Finally, in chapter 4, I demonstrated the platform for measuring triglyceride films and their responses to various duodenal contents such as pancreatic lipase and bile acids, as well as its integration within the coated capsule package described in chapter 3. Figure 5-1 illustrates the prospective data flow from the capsule device, where wireless data extraction enables external access to the status of the potential concentration of the biomolecule of interest at the target region to the patient’s physician, offering insight as to critical information about their health that would aid prognosis.

Table 5-1 Summary of system parameters for the capsule device with reference to their respective chapters for more detail.

Module	Characteristic	Metrics	Chapter
Packaging (Outer)	Eudragit (Dip-coating) MED610 (3D-Printing)	35 mm x 12.7 mm	3
Packaging (Inner)	Conformal Coating Silicone Sealant Epoxy	33.8 mm x 11.5 mm	3,4
Sensing Method	Capacitance	0.8-220 pF 7.3 pF/mV	3,4
Sensing Targets/Substrates	Trypsin (Sensor Only) Lipase/Bile Acids (SPA/Capsule)	Gelatin/Glutaraldehyde Stearin/Glycerol	2,4
Wireless Comm.	Bluetooth LE	2.4 GHz	3,4
Power Source	Li-Polymer	14 mAh/3.3V	3,4

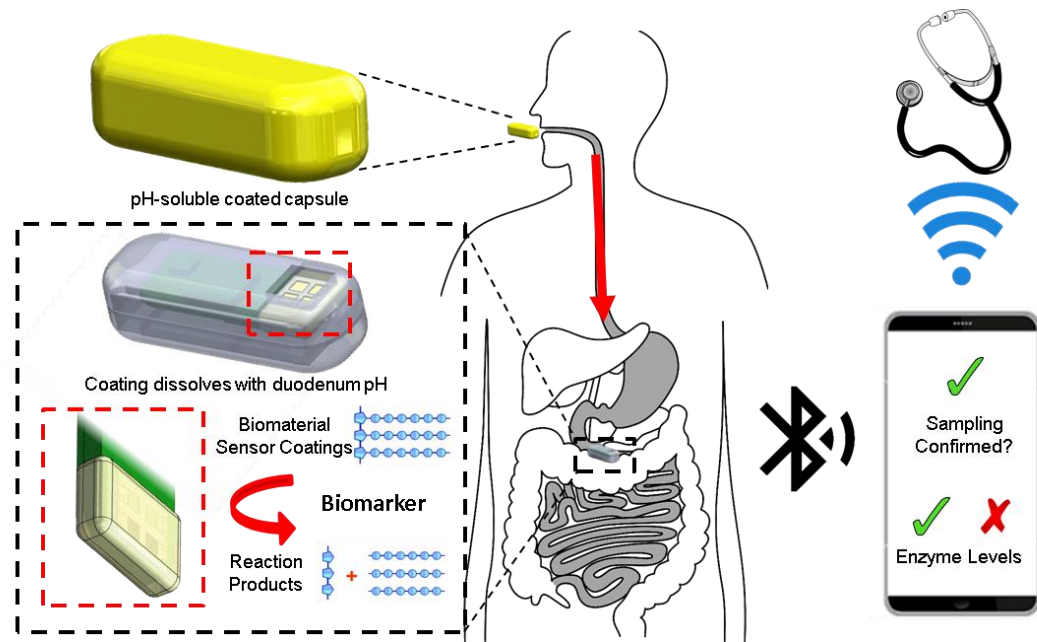


Figure 5-1 Depiction of application. The capsule is protection in environmental pH reflecting that of the stomach until reaching the small intestine via pH-sensitive polymer coating. Upon dissolution, the fluid is sampled via embedded gratings, and pancreatic lipase reacts with triglyceride coatings to increase the capacitance of the sensors. This is transmitted to a phone wirelessly, and the data can be shared with medical practitioners.

In chapter 2, I first studied gelatin films, specifically methods for their deposition and crosslinking for physiological stability and their overall integration with microfabricated impedance sensors for responding to various pancreatic enzymes. Using IDE sensor designs initially intended for measuring biofilm growth, I was interested in observing their utility for measuring biomaterial film processes that involved their reduction instead [142]. After preliminary results involving impedance trends – such as those over spectra from 10 Hz-1 MHz at specific frequencies and through Nyquist analyses – specific to our target enzyme, i.e. pancreatic trypsin, I compared them to trends produced when either the film was absent and/or in the presence of nonspecific enzymes (lipase and amylase). This yielded observable distinctions, such as those seen in Figure 5-2, between them that I then used to optimize sensor design parameters, which involved characterization of various process parameters and resulting films that could be produced with different spin speeds and device geometries while determining feasible sensor parameters that could enhance sensitivity. Impedance results were also decomposed into real and imaginary elements, enabling our transition to measuring capacitance with a subsequently developed capacitive-sensing and wireless electronics platform.

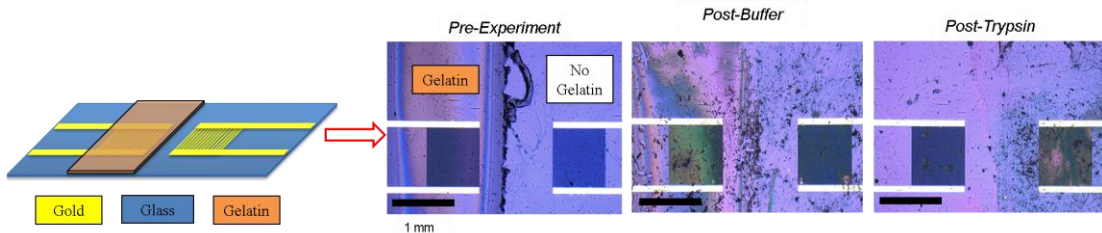


Figure 5-2 (Left) Schematic and (right) optical images of sensors with deposited film. The optical images indicate distinct removal of film after trypsin response compared to buffer alone, where the film remains relatively intact.

Chapter 3 consists of using the platform, after thorough assembly and calibration processes, to evaluate a novel packaging strategy with a capsule form factor to enable passive targeting of the capsule into simulated target GI regions based on their pH. Various capsule geometries were designed and considered for testing, each with some feature that overcame one of the prior iteration's flaws; each design required at least inlets that allow inflow of environmental fluid into a chamber containing the sensors. Eudragit E PO, S100, and L100 polymer coatings were tested for targeting simulated fluids for the stomach, duodenum, and ileum, respectively, with an emphasis on coating thickness and measuring the time of dissolution and subsequent filling of the sensing chamber. The platform was transitioned into a microelectronics system, depicted in Figure 5-3, with a small form factor for subsequent integration into a capsule system, after which additional assembly testing led to its validation as an independent system, powered with a Li-polymer battery and controlled through commands from a mobile app. As described in chapter 3, the primary utility of the system is not just through its potential for *in vivo* use, but for enabling user-friendly and real-time measurement acquisition through different applied stimuli and their impacts on various system characteristics.

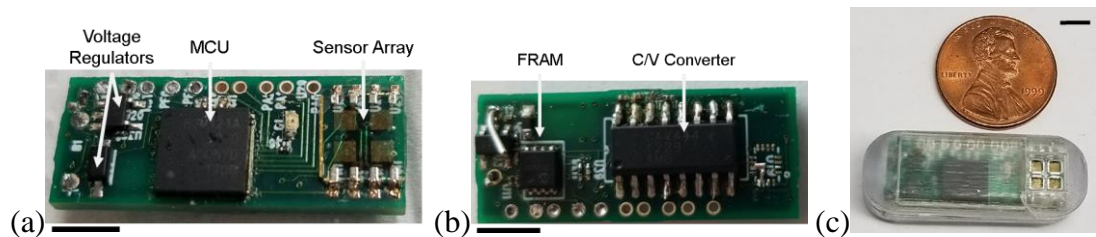


Figure 5-3 (a) Top and (b) bottom views of sensor-connected PCB, and (c) photograph of assembled capsule. Scale bar=5 mm.

Based on the fundamental approaches we developed using capacitance as a metric for measuring biomaterial film reactions with specific and nonspecific targets, I

further adapted the sensors used in the microelectronics system, or SPA, to measure triglyceride film reactions in chapter 4. Stearin films were deposited in molten phase and with glycerol as a solution modifier and subsequent cooling using multiple approaches, with dip-coating producing the most stable to the implemented physiologically simulating environments. The amorphous films were characterized, offering signal profiles that also suggested dependencies on film qualities, and observed to affect electrical properties of the sensor surface by measuring capacitance and morphology, with the SG-SPAs and via SEM, respectively. These features were analyzed in response to hydrolytic reactions from pancreatic lipase as well as emulsification from bile acids. The capacitance response over time was found to vary with concentration, and while this implies that neither signal can be isolated if both are simultaneously present, this also reduces limitations as to the types of reactions that can be measured with the platform. Furthermore, the SG-SPAs were then assembled within the Eudragit coated capsules, which were observed to protect the sensors in acidic conditions until the environment reached neutral conditions. Upon sampling, application of PL into the solution produced more significant changes in capacitance, reflecting the ability to perform pH-targeted sensing with the encapsulated SG-SPAs.

## 5.2 Future Outlook

The work presented in this dissertation has led to the emergence of new directions that can be pursued for either enhancing characterization methods for capsule devices or additional features for more complex functionalities.

### 5.2.1 Gastrointestinal-Simulating Biochemical and Biomechanical Conditions

Predicting capsule function *in vivo* through benchtop experimentation relies significantly on how well the testing platform mimics the target environment. The capsule geometry has been most utilized because it is already implemented in pharmaceuticals for daily use, but can be implied that it limits disruption to most GI functions. Most benchtop tests, such as those performed in this dissertation, consist of beaker-level testing and isolated or low complexity solution compositions until they are implemented in animal models for the next phase of device characterizations, specifically porcine due to its distinct fundamental similarities to humans in terms of anatomy, physiology, and nutrition, among others [237]. However, more complex functions desired in later capsule designs may produce more risk to the GI environment of the animal, while there also may not be enough comparison between them and humans to imply downstream clinical success. This leads to costly experimentation requirements that can be remediated through lower-cost testing setups to provide more relevant results and expectations.

A primary feature of the GI tract that can alter device function is the state of its biochemical composition over time, especially considering its variability upon stimulation through either intravenous administration or oral ingestion. A few examples, as discussed in chapter 1 of this thesis, of how the output can change is through tests such as the secretin-CCK and Lundh tests, where injected hormones or a carefully devised meal can stimulate increased pancreatic secretion output for higher sampling rates and enzyme concentrations in the duodenum [55], [126]. While such simulants only account for changes in pancreatic output, it is critical to evaluating

device function that the device be tested in the presence of other GI secretions, such as those present in the gastric environment. To compensate for this variability, some procedures implement methods of establishing control over GI content, which can be observed in the preparation for capsule or normal endoscopic procedures. Here, the patient is instructed to fast overnight, cleanse with polyethylene glycol (PEG) solutions, or drinking clear solutions such as water to ensure visualization remains unimpeded [238].

For the device presented in this dissertation, it is likely that future developments will require the establishment of similar preparations while assessing how different stimulants can affect device efficacy. This efficacy, however, must be evaluated from multiple perspectives. Most relevant to the characterizations performed in this work, however, are the impact of such preparations on (a) sensing and (b) packaging or targeting efficacies. For *in vitro* characterizations, fluids should be altered periodically through various conditions – such as aliquots of enzymes presented in Table 1-1, various local PEG concentrations, or different pH levels for example – and how the system responds. For (a), it must be understood how film-coated sensors react both through resulting capacitive signals, as well as potential morphological changes, including the impact on film mass and thickness. For (b), sensors without films must be tested with these fluids, when integrated into capsules coated with the Eudragit formulations described in Chapter 3, to determine how the timing of coating dissolution can behave. Ultimately, both sensing and GI-targeting functions should be tested when film-coated sensors are integrated within coated capsules, and capacitance signals should be monitored when each stimulus is applied in real-time.

From a mechanical perspective, models for replicating the forces – such as traction, contact, and peristaltic wave propagation – produced in GI peristalsis have been designed for capsule devices [239]. Much work has been done on understanding the mechanics of various regions of GI propulsion, with robotic capsule devices aiding in this evaluation by providing metrics for their own motility [240], [241]. For this dissertation, simulating intestinal propulsion would aid significantly in evaluating the integrity of the capsule coatings, enabling us to implement further design changes that could affect their respective efficacies, especially in both specific and nonspecific pH environments.

Figure 5-4 presents a concept developed by Prateek Sayyarapaju and I, consisting of 3D-printed components for intestinal peristalsis simulation. The advent of 3D-printing has enabled facile fabrication of numerous components types, varying in characteristics such as rigidity, opacity, and biocompatibility, such that we can vary the material for each component to serve best for its respective purpose. The system consists of a tissue-mimicking tube, which is designated to hold the capsule in a portion that is squeezed on both sides around the capsule edges to limit its motion. This squeezing is achieved with peristaltic rings, which are interchangeable to modify the change in diameter that occurs with muscle contractions. The tube is fastened on both sides to a chain looped around a motor-interfacing gear, which can be programmed for different speeds. Different programming can aid in mimicking different peristaltic motility conditions, while the lumen of the tube can be modified with excised tissue samples. Furthermore, the tube contains fluidic inlets on either side (one of which can function as an outlet), allowing for the implementation of different fluid profiles

described previously in this section. The use cases of such a system are for testing of features such as (a) sensor noise due to peristalsis, (b) capsule mechanical integrity, and (c) the supplemental effect of GI-simulating fluids on capsule integrity and sampling. While the system is limited regarding printable materials and motor robustness, there is potential to isolate relevant peristalsis conditions that can aid predicting the efficacy of targeting or sensing functions of the capsule.

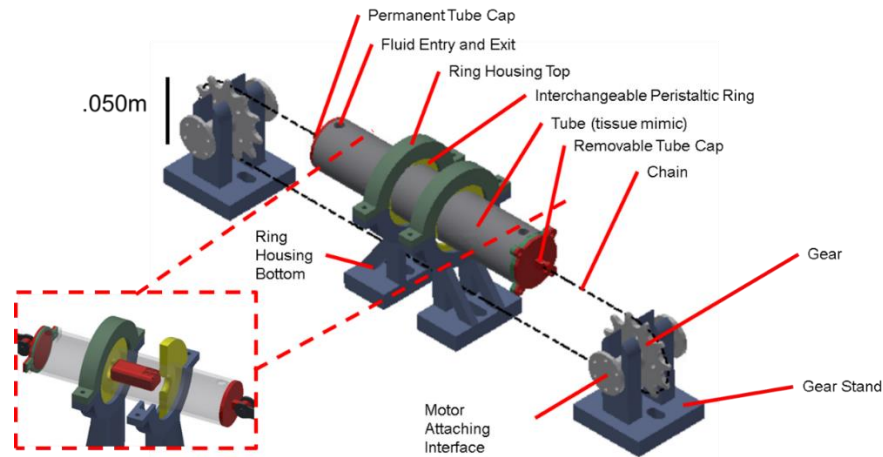


Figure 5-4 Peristalsis simulator, consisting mostly of 3D printed components.

### 5.2.2 Anchoring Capsules

Because content transit through the GI tract is generally a temporary process, most capsule devices are designed for metric measurement as single time points along specific locations of the canal trajectory. However, some conditions would benefit more from continuous monitoring of a metric at the same location over extended time periods, such as ulcer progression in the stomach or inflammation in the colon [242]–[244]. System implantation or retention is a function required for several devices intended for long-term residence in the GI tract, though it can be challenging to embed such functions into a capsule without clinical interventions such as surgery [245].

One of the challenges with adhesion in the GI tract is due to surface variation. For example, structures such as villi and microvilli, such as those depicted in Figure 5-5a, are present along the lumen, which are critical for increasing intestinal surface area and therefore nutrient absorption into underlying blood vessels [246], [247]. After investigating various fabrication processes, one of my mentees, Aditya Nilacantan, had 3D-printed example villi surfaces for potential testing with capsule-based anchoring structures. Some work has been done on capsule-based adhesion mechanisms to the GI mucosa (Figure 5-5c), though we have also designed various microhooks, bioinspired by microneedles from common GI parasites, that we have also 3D-printed for facile integration with our capsule shells (Figure 5-5d) [231], [248]. Though the depicted concept would require appropriate spatial and mass distribution of electronic components, the microhooks could enable a passive approach to anchor the capsule to the mucosa for measuring a metric in the same location for multiple instances. We further envision, due to the ability to simultaneously and wirelessly transmit signals to our microelectronics platform, the active triggering of anchor actuation upon external command. Such advancements would be critical to establishing further levels of control to the system while *in vivo*, thereby expanding the time scales for measuring specific analytes of interest at target locations in the GI tract.

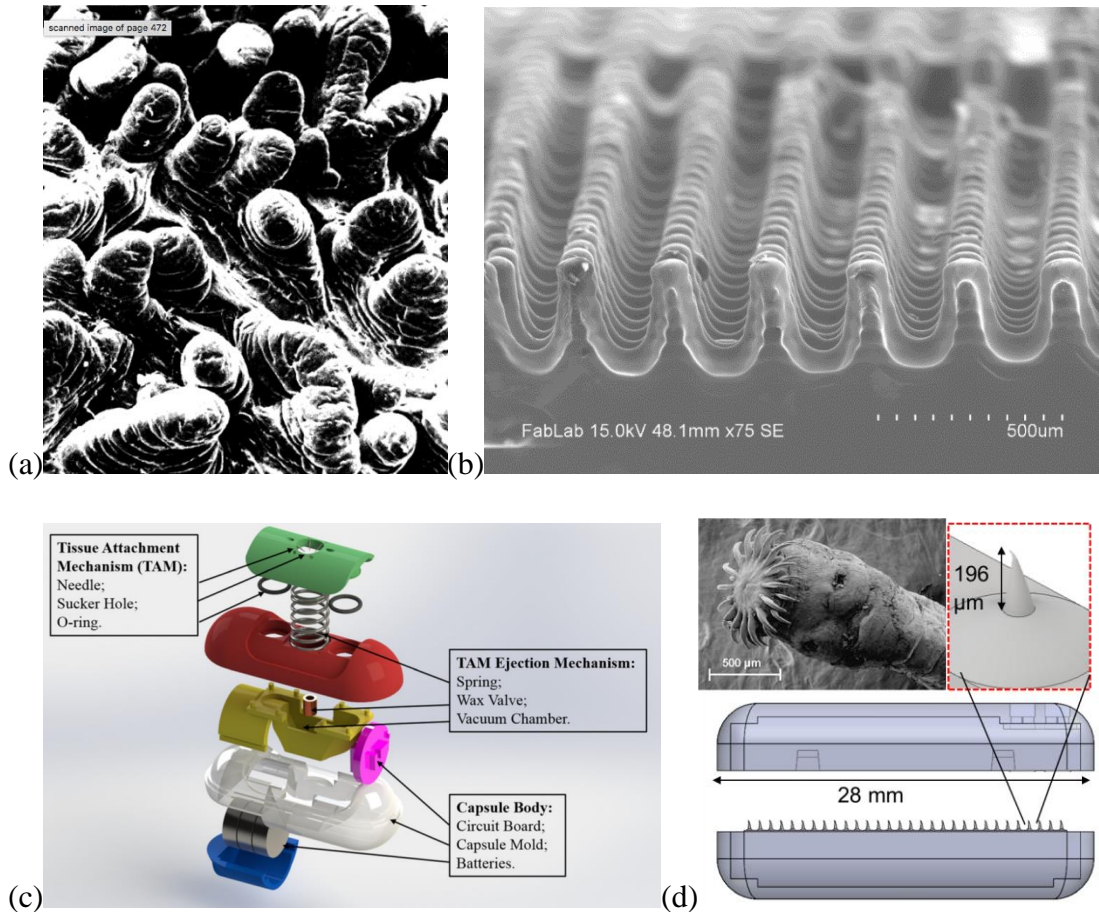


Figure 5-5 SEM imaging of (a) porcine (reproduced with permission from [246]) and (b) 3D-printed villi with an EnvisionTEC Perfactory 4. (c) Implantation capsule robot (reproduced with permission from [249]). (d) 3D-printed anchoring concept for passive capsule implantation; left inset: head of *Taenia Solium* Scolex (reproduced with permission from [248]), right inset: close-up of microhook mimic.

### 5.2.3 Feedback-Triggered Therapeutic Release

A primary purpose of biosensors in the clinical setting is to understand the state of a physiological metric and determine whether intervention is necessary to revert an unhealthy or pathological condition back to homeostasis for said metric. For example, patients with diabetes, after learning through a blood glucose sensor that they have high blood sugar, understand that they require insulin [250]. Figure 5-6 depicts the organs in or closely related to the GI tract, and lists various associated conditions that ingestible capsules could aid through feedback-triggered therapeutics [251].

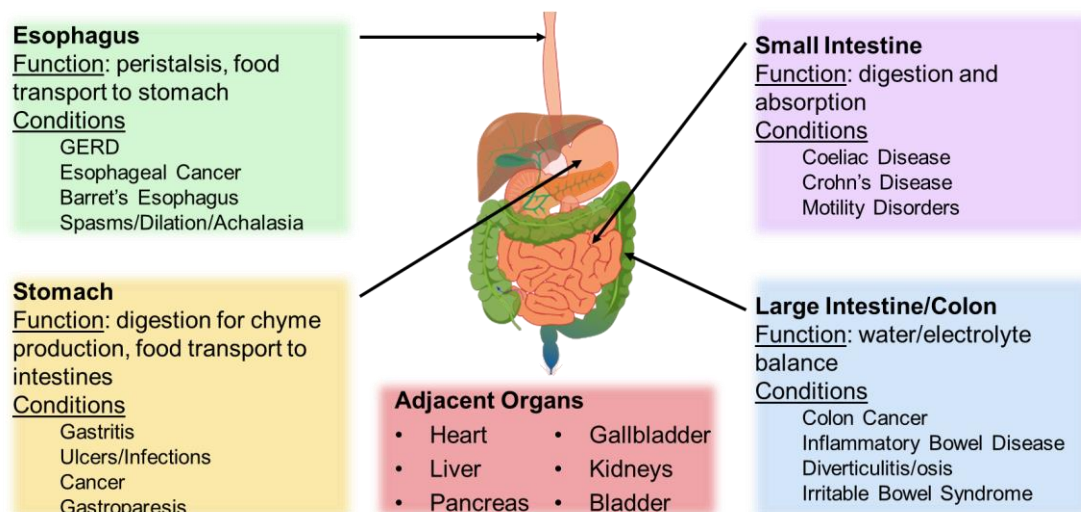


Figure 5-6 Physiology of GI affected regions, reflecting potentially relevant information accessible by capsule devices.

The same would be said for the detected analytes from the work in this dissertation, i.e. low levels of pancreatic trypsin or lipase resulting from conditions such as pancreatitis, pancreatic cancer, or cystic fibrosis would prompt a dose or supplement of these enzymes from an external source [1], [4], [150]. Because the platform is programmable, it is well within the system limits to use the acquired information to trigger another system to release enzyme supplements. This would require various conditions to be satisfied: (1) the information would need to be processed appropriately such that an algorithm for interpreting the film response would indicate an enzyme efficiency, and (2) the platform would need to be modified to allow control over a mechanism, using either the previous algorithm or patient-enabled from a button on the mobile app, for either actuating a drug-release switch or dissolving a reservoir-enclosing membrane [231].

### 5.3 Conclusion

The GI tract is a complex environment that, while relatively well understood, continues to demonstrate itself as a hub for unknown physiological interactions that demand interrogation. Ingestible devices require a small form factor to reduce potential downstream risk to patient health, which, combined with the current state of microelectronics components and a lack of control inherent to content consumption, remain significant limitations to the range of achievable device functions. This dissertation addresses fabrication and integration strategies in embedding novel capsule functions by designing systems for (a) interfacing various biochemical reactions with electronic sensing modalities through biomaterial films and (b) targeted sampling of GI-simulating environments and their contents using pH-soluble coatings materials as system packaging. Disassociating electrical signal and system elements from interfacing with biomaterial reactions led to a platform design that, while useful for a variety of capacitive and/or film-based sensing challenges, was demonstrated here for detecting pancreatic enzyme activity and characterizing packaging integrity within the context of an integrated capsule.

The discussed designs, fabrication processes, and resulting assembled devices represent significant technological advances to bioelectronics interfacing and the field of ingestible technologies. The final capsule sets a precedent for GI targeting microsensors and the types of biomolecular species that can be detected, revolutionizing the capabilities of such devices for aiding healthcare paradigms from new perspectives and in low risk settings. The device and materials are relatively low cost, with facile interfacing with users (i.e. patients or clinicians) toward establishing

new goals in personalized medicine. The capsule serves additionally as a research tool, enabling the elucidation of how target physiological metrics, such as enzymes or bile acids, respond *in situ* to different stimuli and during varying conditions. Ultimately, the strategies implemented with this capsule platform for targeting sampling and sensing in GI environments facilitate future development in non-invasive GI diagnostics, both in academia regarding the manner in which molecular trends are observed during different pathologies, as well as clinically due to a reduction in the clinical interface required to obtain medically-relevant information.

## 6. Appendices

### *6.1 Appendix A: Masks Used*

#### A.1 Microfluidic Impedance Sensing

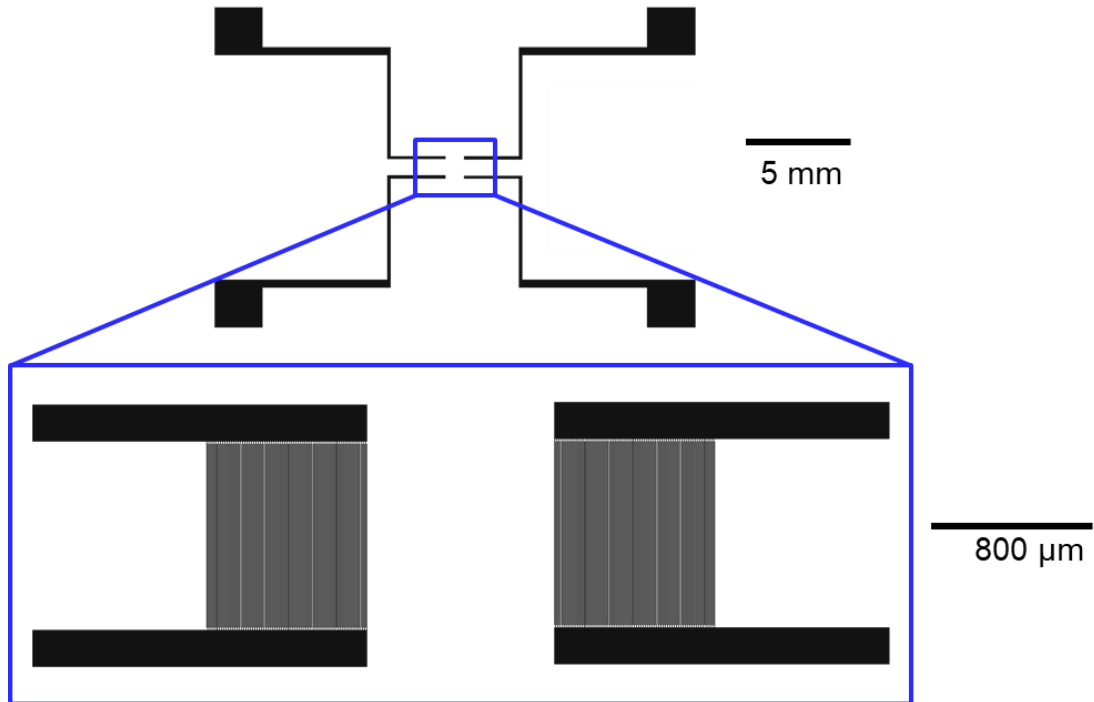


Figure 6-1 IDE sensors used in chapter 2. Finger width: 2  $\mu\text{m}$ , finger spacing: 4  $\mu\text{m}$ , finger length: 1 mm, number of fingers per electrode: 65.

## A.2 First Capsule Mask for Capacitive Sensing

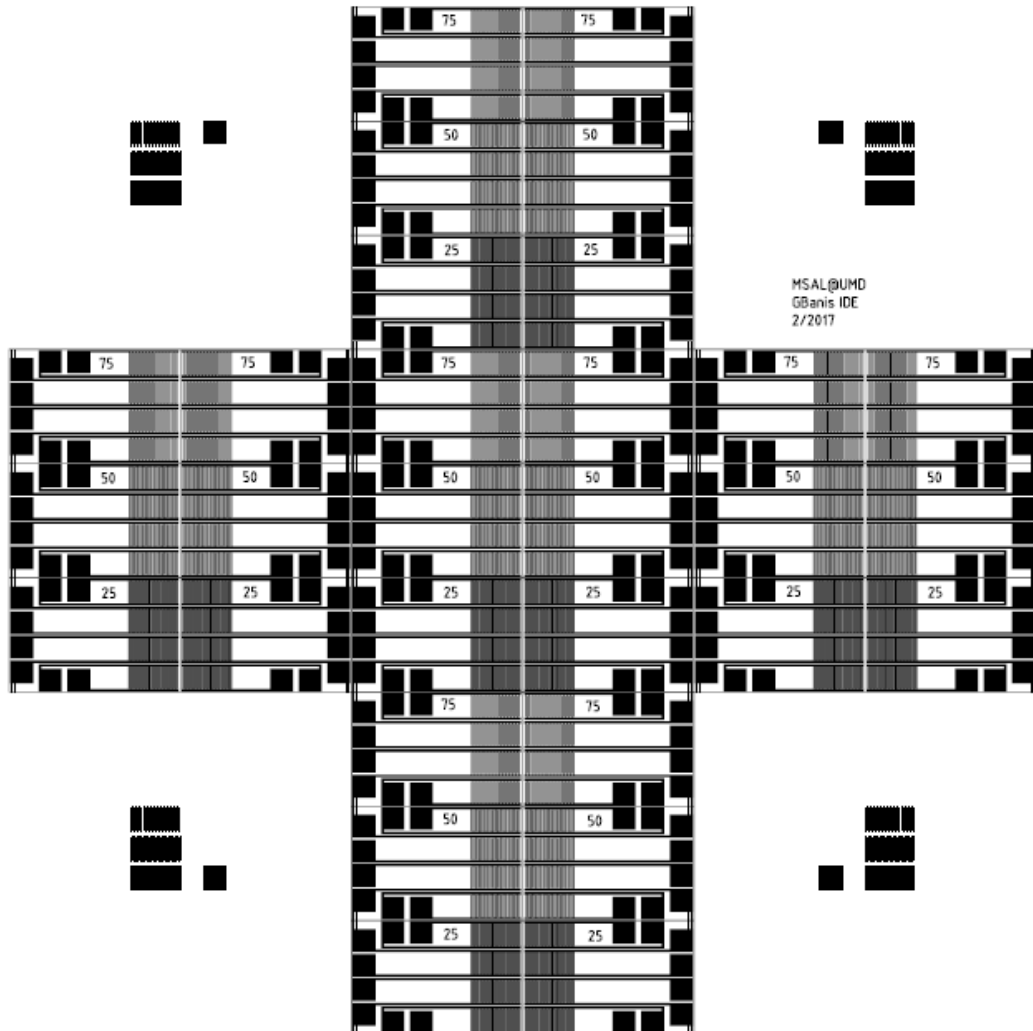


Figure 6-2 IDE sensor patterns used in chapter 3 to measure integrity of the packaging coatings. (a) Complete photomask with 10 die for each 4x1 sensor die, each with different finger geometries: 25, 50, and 75  $\mu\text{m}$  width and spacing and 44, 22, and 14 fingers per electrode, respectively. Finger length: 2 mm.

### A.3 Sensors used for SPA

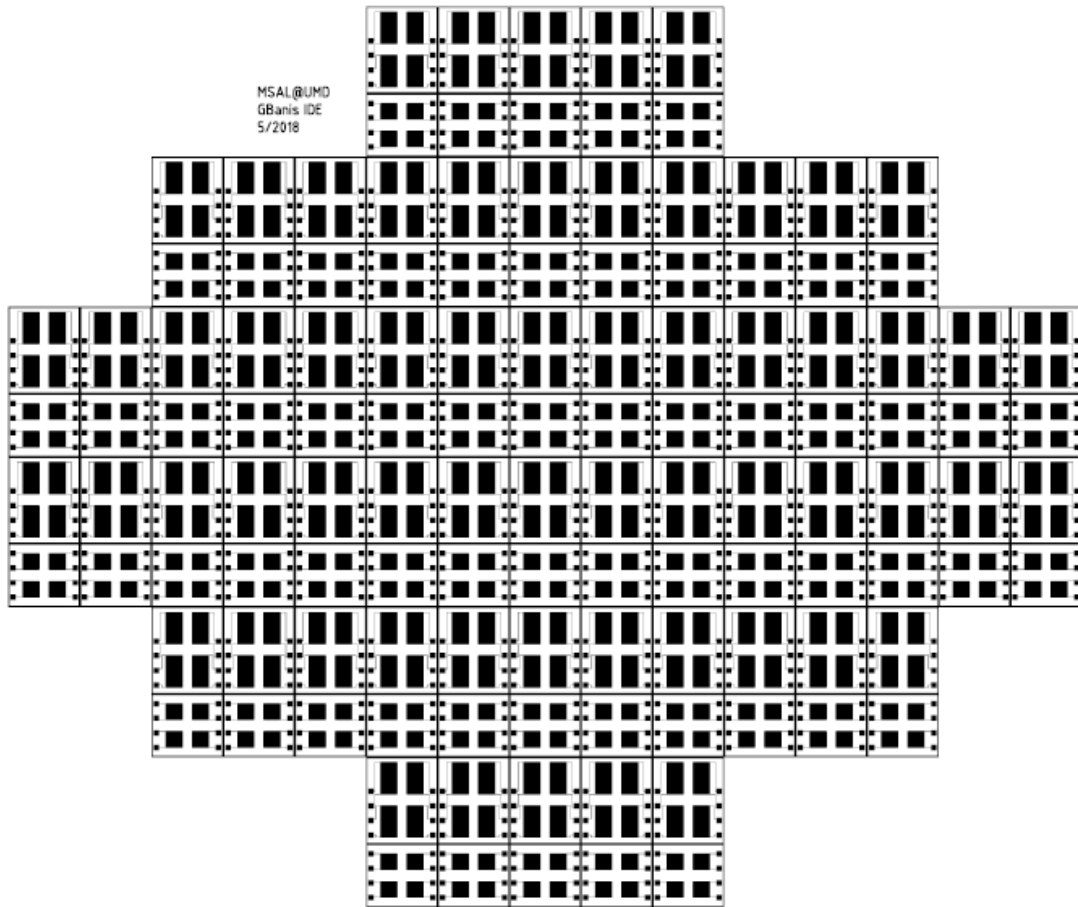


Figure 6-3 IDE sensor patterns used in chapters 3 and 4 for SPAs. Mask Design: 124 Sensor Output, 62 each of long (length=3 mm) /short (1.5 mm) versions. Number of fingers per electrodes = 40.

6.2 Appendix B: COMSOL Simulation and Results

To reduce computational processing requirements, I reduced the sensor to a two-finger unit rather than 146 fingers, used earlier in this chapter. One finger is denoted as working electrode while the other is the ground, and the material properties and dimensions used are listed in Table 6-1. A cross-sectioned diagram of our model and the conditions I used are depicted below in a, electrodes are simulated with either no film, a 0.5  $\mu\text{m}$  thick (to represent partially digested), and 1  $\mu\text{m}$  thick (to represent undigested) films. For comparison, the capacitance of the sensors was measured using LCR meter (Agilent E4980A) controlled with LabVIEW. Measurements were carried out sequentially in air, in phosphate buffer (PB; pH 7.5), and finally in 1 mg/mL bovine pancreatic trypsin in PB at 37°C (physiological temperature) under constant stirring. Sensors tested were either coated in gelatin or uncoated. AC signals were swept from 100 kHz to 1 MHz at 50 mV in every 90 seconds. I observed films before and after each experiment and compared extracted parallel capacitance experimental results to COMSOL Multiphysics simulation results. Direct DC capacitance responses were calculated for films with a 100  $\mu\text{m}$  average thickness or 0  $\mu\text{m}$  (no film) surrounded by either buffer or air. Simulation capacitance was obtained for only two fingers in the sensor, but was scaled up accordingly for IDEs [252].

Table 6-1 Parameters used for the COMSOL simulation.

<b>Material</b>	<b>Glass (substrate)</b>	<b>Gelatin (film)</b>	<b>Pbs (buffer)</b>	<b>Gold (electrodes)</b>
<b>Conductivity (s/m)</b>	1.0e-14	7.0e-5	1.52	44.2e6
<b>Dimension (width x depth x height)</b>	1 mm x 6 $\mu\text{m}$ x 0.4 $\mu\text{m}$	1 mm x 6 $\mu\text{m}$ x 1-0.5 $\mu\text{m}$	1 mm x 6 $\mu\text{m}$ x 10 $\mu\text{m}$	1 mm x 1 $\mu\text{m}$ x 200 nm (x2) (4 $\mu\text{m}$ spacing)

Figure 6-4 (b) demonstrates a comparison of capacitance signals for both experimental and simulation results. As indicated by the y-axes, the capacitance magnitudes from the experiment are slightly offset from the simulation results, though the trends are similar. The decrease in capacitance for the film-coated sensors from air to buffer are interesting but not unexpected, as it likely reflects charge dissipation from the film, which is at the surface of the electrode, to the buffer due to its electrical conductivity (air:  $5.5E-15$  S/M compared to PBS:  $1.52$  S/M). The step change in capacitance due to buffer contact to the electrodes is preceded however, and indicates the potential for monitoring capacitance alone to measure film digestion rather than total impedance. This result becomes reflected further in the next few chapters, both for monitoring film digestion and sampling of environmental buffer.

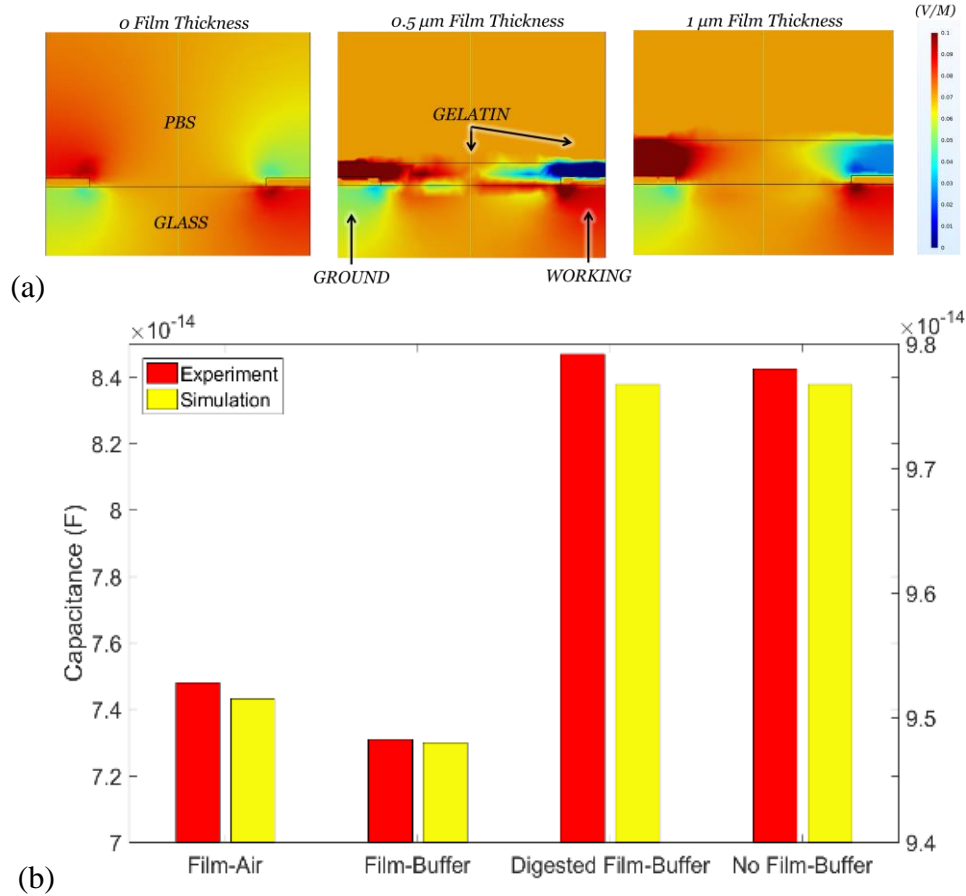


Figure 6-4 (a) Cross-section of simulation model (top to bottom: medium, film, sensor, wafer), (b) mean capacitance from experimental degradation of film over IDE sensor (left y-axis) and simulation (right y-axis) results. Between electrode fingers, electric field intensity increases significantly in the presence of gelatin. Electric field height decreases significantly, the magnitude remains the same, and lateral electric field distribution is altered.

#### 6.4 Appendix C: MATLAB Analysis Code and GUI

This MATLAB code automatically initializes a GUI, depicted in Figure 6-5, that enables input of up to four data sequences over time, with customization over time and percent change in capacitance (x- and y-axes, respectively) ranges, applied smoothing filters, and legend labels. The sequences used must be in a .csv file format with data arrangement such as that depicted in Figure 6-6.

```

function varargout = multi_data_sequences_5_31_19(varargin)
% MULTI_DATA_SEQUENCES_5_31_19 MATLAB code for
multi_data_sequences_5_31_19.fig
%     MULTI_DATA_SEQUENCES_5_31_19, by itself, creates a new
MULTI_DATA_SEQUENCES_5_31_19 or raises the existing
%     singleton*.
%
%     H = MULTI_DATA_SEQUENCES_5_31_19 returns the handle to a new
MULTI_DATA_SEQUENCES_5_31_19 or the handle to
%     the existing singleton*.
%
%
MULTI_DATA_SEQUENCES_5_31_19('CALLBACK',hObject,eventData,handles,...
.) calls the local
%     function named CALLBACK in MULTI_DATA_SEQUENCES_5_31_19.M
with the given input arguments.
%
%     MULTI_DATA_SEQUENCES_5_31_19('Property','Value',...) creates
a new MULTI_DATA_SEQUENCES_5_31_19 or raises the
%     existing singleton*. Starting from the left, property value
pairs are
%     applied to the GUI before
multi_data_sequences_5_31_19_OpeningFcn gets called. An
%     unrecognized property name or invalid value makes property
application
%     stop. All inputs are passed to
multi_data_sequences_5_31_19_OpeningFcn via varargin.
%
%     *See GUI Options on GUIDE's Tools menu. Choose "GUI allows
only one
%     instance to run (singleton)".
%
% See also: GUIDE, GUIDATA, GUIHANDLES

% Edit the above text to modify the response to help
multi_data_sequences_5_31_19

% Last Modified by GUIDE v2.5 05-Jun-2019 15:50:08

% Begin initialization code - DO NOT EDIT
gui_Singleton = 1;
gui_State = struct('gui_Name',       mfilename, ...
                  'gui_Singleton',  gui_Singleton, ...
                  'gui_OpeningFcn', @multi_data_sequences_5_31_19_OpeningFcn, ...
                  'gui_OutputFcn',  @multi_data_sequences_5_31_19_OutputFcn, ...
                  'gui_LayoutFcn',  [] , ...
                  'gui_Callback',    []);
if nargin && ischar(varargin{1})
    gui_State.gui_Callback = str2func(varargin{1});
end

if nargout

```

```

    [varargout{1:nargout}] = gui_mainfcn(gui_State, varargin{:});
else
    gui_mainfcn(gui_State, varargin{:});
end
% End initialization code - DO NOT EDIT

% --- Executes just before multi_data_sequences_5_31_19 is made
visible.
function multi_data_sequences_5_31_19_OpeningFcn(hObject, eventdata,
handles, varargin)

handles.output = hObject;
guidata(hObject, handles);

% --- Outputs from this function are returned to the command line.
function varargout = multi_data_sequences_5_31_19_OutputFcn(hObject,
eventdata, handles)
varargout{1} = handles.output;

% _____ Set Value Objects for Plots _____ %

% _____ Filter Setting _____ %

function edit1_Callback(hObject, eventdata, handles)

% --- Executes during object creation, after setting all properties.
function edit1_CreateFcn(hObject, eventdata, handles)
if ispc && isequal(get(hObject, 'BackgroundColor'),
get(0, 'defaultUicontrolBackgroundColor'))
    set(hObject, 'BackgroundColor', 'white');
end

% --- Executes on button press in pushbutton9.
function pushbutton9_Callback(hObject, eventdata, handles)
handles = guidata(hObject);
s1 = get(handles.edit1, 'String');
handles.filter=str2double(s1);
guidata(hObject, handles);

% _____ End Time 1 Setting _____ %

function edit5_Callback(hObject, eventdata, handles)

% --- Executes during object creation, after setting all properties.
function edit5_CreateFcn(hObject, eventdata, handles)
if ispc && isequal(get(hObject, 'BackgroundColor'),
get(0, 'defaultUicontrolBackgroundColor'))
    set(hObject, 'BackgroundColor', 'white');
end

```

```

% --- Executes on button press in pushbutton11.
function pushbutton11_Callback(hObject, eventdata, handles)
handles = guidata(hObject);
et1 = get(handles.edit5, 'String');
endtime1=str2double(et1);
guidata(hObject, handles);
axes(handles.axes1);
xlim([0 endtime1])

% _____ End Time 2 Setting _____ %

function edit6_Callback(hObject, eventdata, handles)

% --- Executes during object creation, after setting all properties.
function edit6_CreateFcn(hObject, eventdata, handles)
if ispc && isequal(get(hObject, 'BackgroundColor'),
get(0, 'defaultUiControlBackgroundColor'))
    set(hObject, 'BackgroundColor', 'white');
end

% --- Executes on button press in pushbutton12.
function pushbutton12_Callback(hObject, eventdata, handles)
handles = guidata(hObject);
et2 = get(handles.edit6, 'String');
endtime2=str2double(et2);
guidata(hObject, handles);
axes(handles.axes2);
xlim([0 endtime2])

% _____ End Time 3 Setting _____ %

function edit7_Callback(hObject, eventdata, handles)

% --- Executes during object creation, after setting all properties.
function edit7_CreateFcn(hObject, eventdata, handles)

if ispc && isequal(get(hObject, 'BackgroundColor'),
get(0, 'defaultUiControlBackgroundColor'))
    set(hObject, 'BackgroundColor', 'white');
end

% --- Executes on button press in pushbutton13.
function pushbutton13_Callback(hObject, eventdata, handles)
handles = guidata(hObject);
et3 = get(handles.edit7, 'String');
endtime3=str2double(et3);
guidata(hObject, handles);
axes(handles.axes3);
xlim([0 endtime3])

```

```

% _____ End Time 4 Setting _____ %

function edit8_Callback(hObject, eventdata, handles)

% --- Executes during object creation, after setting all properties.
function edit8_CreateFcn(hObject, eventdata, handles)
if ispc && isequal(get(hObject,'BackgroundColor'),
get(0,'defaultUiControlBackgroundColor'))
    set(hObject,'BackgroundColor','white');
end

% --- Executes on button press in pushbutton14.
function pushbutton14_Callback(hObject, eventdata, handles)
handles = guidata(hObject);
et4 = get(handles.edit8,'String');
endtime4=str2double(et4);
guidata(hObject, handles);
axes(handles.axes4);
xlim([0 endtime4])

% _____ PLOTTING DATA _____ %

% --- Executes on button press in pushbutton1.
function pushbutton1_Callback(hObject, eventdata, handles)

global filename1
global pathname
global currentfolder

[filename1, pathname] = uigetfile({'C:\George\Capsule
Experiments\BLE\Calibration\*.csv'})
currentfolder = fullfile(pathname, filename1);
if isequal(filename1,0) || isequal(pathname,0)
    return
end

fileID = fopen(fullfile(pathname, filename1));

temp = fscanf(fileID,'%d',[8 Inf]);
handles.fileData = temp';
guidata(hObject, handles);

% _____ Plot 1 Stuff _____ %

% _____ below this, actual time _____ %
%path=('C:\George\');
path=pathname;

```

```

file_path=strcat(path,filename1);
class(file_path);
Time = GetFileTime(file_path);
Time_1=struct2cell(Time);
finish=Time_1(3);
start=strsplit(filename1,"-");
start_date=str2double(start(5));
%start_hour=str2double(start(6));
%start_min=str2double(start(7));
global name1

table1 = readtable(filename1);
sensor1=table2array(table1(:,2));

end_date=start_date;
end_totaltime=table2array(table1(:,1));

timex1=cell2mat(end_totaltime(1,1));
start_time=strsplit(timex1,":");
start_hour=str2double(start_time(1));
start_min=str2double(start_time(2));
timex=cell2mat(end_totaltime(length(end_totaltime),1));
end_time=strsplit(timex,":");
end_hour=str2double(end_time(1));
end_min=str2double(end_time(2));

cap_val_1=[];
for j=1:length(sensor1)
    volt_val_1(j,:) = 1/((4095/3.3)/(sensor1(j)))-0.05;
    %cap_val_1(j,:) = ((volt_val_1(j,:)-volt_val_1(1))/0.0031);
    cap_val_1(j,:) = ((volt_val_1(j,)-2.5325)/0.0031);
    delta_cap_1(j,:) = abs(cap_val_1(j,:)-
cap_val_1(1,:))*100/abs(cap_val_1(1,:));
end
total_cap_val_1=cap_val_1;
total_delta_cap_val_1=delta_cap_1;

%_____Setting up time_____
N= length(sensor1);
Total_time = (end_date - start_date) * 24 * 60 * 60 + (end_hour -
start_hour)* 60 * 60 + (end_min - start_min) * 60; % Calculate
total time in seconds
Time_step = Total_time/(N-1); % average step time in seconds between
two consecutive runs
Time_s = 0: Time_step: Total_time; % create an array called time
Time_m = Time_s/(60); % row array of time in hours
m=1;

%_____ plot 1 stuff_____
filter = handles.filter;
axes(handles.axes1);
handles.h1=plot(handles.axes1,Time_m(m:length(total_delta_cap_val_1)
),smooth(total_delta_cap_val_1(1:length(total_delta_cap_val_1)),filt
er), 'ko-
```

```

', 'MarkerSize', 5, 'MarkerIndices', 1:75:length(total_delta_cap_val_1))
;
hold on
mean(total_delta_cap_val_1(8:24))
std(total_delta_cap_val_1(8:24))
total_delta_cap_val_1=total_delta_cap_val_1.';
%p=polyfit(Time_m(1:2000),total_delta_cap_val_1(1:2000),1); %for
%publications, 2000 points = 33 min
et1 = get(handles.edit5, 'String');
endtime1=str2double(et1);
endtime1p=endtime1*60;
p=polyfit(Time_m(1:endtime1p),total_delta_cap_val_1(1:endtime1p),1);
xp = linspace(0,endtime1);
yp = polyval(p,xp);
plot(handles.axes1,xp,yp+2, 'k-', 'LineWidth', 2) %display when want
%trendline
hold on
xlabel('Time (min)', 'FontSize', 12, 'FontWeight', 'bold')
ylabel('\DeltaC (%)', 'FontSize', 12, 'FontWeight', 'bold')
%ylim([0 150])
%xlim([0 60])
set(gca, 'fontsize', 12, 'FontWeight', 'bold', 'box', 'off')
ax = gca;
% Place equation in upper left of graph.
xl = xlim;
yl = ylim;
xt = 0.05 * (xl(2)-xl(1)) + xl(1);
yt = 0.90 * (yl(2)-yl(1)) + yl(1);
caption = sprintf('y = %f * x + %f', p(1), p(2));
text(handles.axes1,xt, yt, caption, 'FontSize', 10, 'Color', 'k');
%%display when wanting equation

[filepath,name1,ext] = fileparts(filename1);
set(handles.text2, 'String', name1);
set(gcf, 'PaperPositionMode', 'auto')
print([num2str(name1)], '-dtiffn', '-r0')

%_____group plot stuff_____
axes(handles.axes4);
handles.h1=plot(handles.axes4,Time_m(m:length(total_delta_cap_val_1)
),smooth(total_delta_cap_val_1(1:length(total_delta_cap_val_1)),filt
er), 'ko-
', 'MarkerSize', 5, 'MarkerIndices', 1:75:length(total_delta_cap_val_1))
;
hold on
xlabel('Time (min)', 'FontSize', 12, 'FontWeight', 'bold')
ylabel('\DeltaC (%)', 'FontSize', 12, 'FontWeight', 'bold')
%ylim([0 100])
%xlim([0 60])
set(gca, 'fontsize', 12, 'FontWeight', 'bold', 'box', 'off')
ax = gca;
%_____END DATA 1_____

```

```

% --- Executes on button press in pushbutton2.
function pushbutton2_Callback(hObject, eventdata, handles)

global filename2
global pathname2
global currentfolder2

[filename2, pathname2] = uigetfile({'C:\George\Capsule
Experiments\BLE\Calibration\*.csv'})
currentfolder2 = fullfile(pathname2, filename2);
if isequal(filename2,0) || isequal(pathname2,0)
    return
end

fileID = fopen(fullfile(pathname2, filename2));

temp = fscanf(fileID, '%d', [8 Inf]);
handles.fileData = temp';
guidata(hObject, handles);

% _____ Plot 2 Stuff _____ %

% _____ below this, actual time _____ %
%path=('C:\George\');
path=pathname2;
file_path=strcat(path,filename2);
class(file_path);
Time = GetFileTime(file_path);
Time_1=struct2cell(Time);
finish=Time_1(3);
start=strsplit(filename2, "-");
start_date=str2double(start(5));
%start_hour=str2double(start(6));
%start_min=str2double(start(7));
global name2

table1 = readtable(filename2);
sensor1=table2array(table1(:,2));

end_date=start_date;
end_totaltime=table2array(table1(:,1));

timex1=cell2mat(end_totaltime(1,1));
start_time=strsplit(timex1, ":");
start_hour=str2double(start_time(1));
start_min=str2double(start_time(2));
timex=cell2mat(end_totaltime(length(end_totaltime),1));
end_time=strsplit(timex, ":");
end_hour=str2double(end_time(1));
end_min=str2double(end_time(2));

cap_val_1=[];

```

```

for j=1:length(sensor1)
    volt_val_1(j,:) = 1/((4095/3.3)/(sensor1(j)))-0.05;
    %cap_val_1(j,:) = ((volt_val_1(j,:)-volt_val_1(1))/0.0031);
    cap_val_1(j,:) = ((volt_val_1(j,:)-2.5325)/0.0031);
    delta_cap_1(j,:) = abs(cap_val_1(j,:)-
cap_val_1(1,:))*100/abs(cap_val_1(1,:));
end

total_cap_val_1=cap_val_1;
total_delta_cap_val_1=delta_cap_1;

%_____Setting up time_____
N= length(sensor1);
Total_time = (end_date - start_date) * 24 * 60 * 60 + (end_hour -
start_hour)* 60 * 60 + (end_min - start_min) * 60; % Calculate
total time in seconds
Time_step = Total_time/(N-1); % average step time in seconds between
two consecutive runs
Time_s = 0: Time_step: Total_time; % create an array called time
Time_m = Time_s/(60); % row array of time in hours
m=1;

%_____plot 2 stuff_____
filter = handles.filter;
axes(handles.axes2);
handles.h2=plot(handles.axes2,Time_m(m:length(total_delta_cap_val_1)
),smooth(total_delta_cap_val_1(1:length(total_delta_cap_val_1)),filt
er), 'kd-
', 'MarkerSize', 5, 'MarkerIndices', 1:75:length(total_delta_cap_val_1)
);
hold on
total_delta_cap_val_1=total_delta_cap_val_1.';
%p=polyfit(Time_m(1:2000),total_delta_cap_val_1(1:2000),1); %for
%publications, 2000 points = 33 min
et1 = get(handles.edit6, 'String');
endtimel=str2double(et1);
endtimelp=endtimel*60;
p=polyfit(Time_m(1:endtimelp),total_delta_cap_val_1(1:endtimelp),1);
xp = linspace(0,endtimel);
yp = polyval(p,xp);
plot(handles.axes2,xp,yp+2, 'k-', 'LineWidth', 2)
hold on
xlabel('Time (min)', 'FontSize', 12, 'FontWeight', 'bold')
ylabel('\DeltaC (%)', 'FontSize', 12, 'FontWeight', 'bold')
%ylim([0 150])
%xlim([0 60])
set(gca, 'fontsize', 12, 'FontWeight', 'bold', 'box', 'off')
ax = gca;
% Place equation in upper left of graph.
xl = xlim;
yl = ylim;
xt = 0.05 * (xl(2)-xl(1)) + xl(1);
yt = 0.90 * (yl(2)-yl(1)) + yl(1);
caption = sprintf('y = %f * x + %f', p(1), p(2));
text(handles.axes2,xt, yt, caption, 'FontSize', 10, 'Color', 'k');

```

```

[filepath,name2,ext] = fileparts(filename2);
set(handles.text3, 'String', name2);
set(gcf, 'PaperPositionMode', 'auto')
print([num2str(name2)], '-dtiffn', '-r0')

axes(handles.axes4);
handles.h2=plot(handles.axes4,Time_m(m:length(total_delta_cap_val_1)
),smooth(total_delta_cap_val_1(1:length(total_delta_cap_val_1)),filter), 'kd-
', 'MarkerSize', 5, 'MarkerIndices', 1:75:length(total_delta_cap_val_1))
;
hold on
xlabel('Time (min)', 'FontSize', 12, 'FontWeight', 'bold')
ylabel('\DeltaC (%)', 'FontSize', 12, 'FontWeight', 'bold')
%ylim([0 100])
%xlim([0 60])
set(gca, 'fontsize', 12, 'FontWeight', 'bold', 'box', 'off')
ax = gca;
% _____END DATA 2 _____ %

% --- Executes on button press in pushbutton3.
function pushbutton3_Callback(hObject, eventdata, handles)

global filename3
global pathname3
global currentfolder

[filename3, pathname3] = uigetfile({'C:\George\Capsule
Experiments\BLE\Calibration\*.csv'})
currentfolder = fullfile(pathname3, filename3);
if isequal(filename3,0) || isequal(pathname3,0)
    return
end

fileID = fopen(fullfile(pathname3, filename3));

temp = fscanf(fileID, '%d', [8 Inf]);
handles.fileData = temp';
guidata(hObject, handles);

% _____Plot 3 Stuff _____ %

% _____below this, actual time _____ %
%path=('C:\George\');
path=pathname3;
file_path=strcat(path, filename3);
class(file_path);
Time = GetFileTime(file_path);
Time_1=struct2cell(Time);
finish=Time_1(3);
start=strsplit(filename3, "-");
start_date=str2double(start(5));

```

```

%start_hour=str2double(start(6));
%start_min=str2double(start(7));
global name3

table1 = readtable(filename3);
sensor1=table2array(table1(:,2));

end_date=start_date;
end_totalltime=table2array(table1(:,1));

timex1=cell2mat(end_totalltime(1,1));
start_time=strsplit(timex1,":");
start_hour=str2double(start_time(1));
start_min=str2double(start_time(2));
timex=cell2mat(end_totalltime(length(end_totalltime),1));
end_time=strsplit(timex,":");
end_hour=str2double(end_time(1));
end_min=str2double(end_time(2));

cap_val_1=[];
for j=1:length(sensor1)
    volt_val_1(j,:) = 1/((4095/3.3)/(sensor1(j)))-0.05;
    %cap_val_1(j,:) = ((volt_val_1(j,)-volt_val_1(1))/0.0031);
    cap_val_1(j,:) = ((volt_val_1(j,)-2.5325)/0.0031);
    delta_cap_1(j,:) = abs(cap_val_1(j,))-
cap_val_1(1,))*100/abs(cap_val_1(1,));
end
total_cap_val_1=cap_val_1;
total_delta_cap_val_1=delta_cap_1;

%_____Setting up time_____
N= length(sensor1);
Total_time = (end_date - start_date) * 24 * 60 * 60 + (end_hour -
start_hour)* 60 * 60 + (end_min - start_min) * 60; % Calculate
total time in seconds
Time_step = Total_time/(N-1); % average step time in seconds between
two consecutive runs
Time_s = 0: Time_step: Total_time; % create an array called time
Time_m = Time_s/(60); % row array of time in hours
m=1;
%_____ plot 3 stuff _____
filter = handles.filter;
axes(handles.axes3);
handles.h3=plot(handles.axes3,Time_m(m:length(total_delta_cap_val_1)
),smooth(total_delta_cap_val_1(1:length(total_delta_cap_val_1)),filt
er),'k*-
','MarkerSize',5,'MarkerIndices',1:75:length(total_delta_cap_val_1))
;
hold on
total_delta_cap_val_1=total_delta_cap_val_1.';
%p=polyfit(Time_m(1:2000),total_delta_cap_val_1(1:2000),1); %for
%publications, 2000 points = 33 min
et1 = get(handles.edit7,'String');
endtime1=str2double(et1);
endtime1p=endtime1*60;

```

```

p=polyfit(Time_m(1:endtime1p),total_delta_cap_val_1(1:endtime1p),1);
xp = linspace(0,endtime1);
yp = polyval(p,xp);
plot(handles.axes3,xp,yp+2,'k-','LineWidth',2)
hold on
xlabel('Time (min)', 'FontSize',12,'FontWeight','bold')
ylabel('\DeltaC (%)', 'FontSize',12,'FontWeight','bold')
%ylim([0 50])
%xlim([0 60])
set(gca,'fontsize',12,'FontWeight','bold','box','off')
ax = gca;
% Place equation in upper left of graph.
xl = xlim;
yl = ylim;
xt = 0.05 * (xl(2)-xl(1)) + xl(1);
yt = 0.90 * (yl(2)-yl(1)) + yl(1);
caption = sprintf('y = %f * x + %f', p(1), p(2));
text(handles.axes3,xt, yt, caption, 'FontSize', 10, 'Color', 'k');

[filepath,name3,ext] = fileparts(filename3);
set(handles.text4, 'String', name3);
set(gcf, 'PaperPositionMode', 'auto')
print([num2str(name3)], '-dtiffn', '-r0')

axes(handles.axes4);
handles.h3=plot(handles.axes4,Time_m(m:length(total_delta_cap_val_1)
),smooth(total_delta_cap_val_1(1:length(total_delta_cap_val_1)),filt
er),'k*-
','MarkerSize',5,'MarkerIndices',1:75:length(total_delta_cap_val_1))
;
hold on
xlabel('Time (min)', 'FontSize',12,'FontWeight','bold')
ylabel('\DeltaC (%)', 'FontSize',12,'FontWeight','bold')
%ylim([0 150])
%xlim([0 60])
set(gca,'fontsize',12,'FontWeight','bold','box','off')
ax = gca;
% _____END DATA 3_____ %

% --- Executes on button press in pushbutton4.
function pushbutton4_Callback(hObject, eventdata, handles)
cla(handles.axes1,'reset');
fclose('all');

% --- Executes on button press in pushbutton5.
function pushbutton5_Callback(hObject, eventdata, handles)
cla(handles.axes2,'reset');
fclose('all');

% --- Executes on button press in pushbutton6.
function pushbutton6_Callback(hObject, eventdata, handles)
cla(handles.axes3,'reset');
fclose('all');

```

```

% --- Executes on button press in pushbutton7.
function pushbutton7_Callback(hObject, eventdata, handles)
cla(handles.axes4, 'reset');
fclose('all');

function edit2_Callback(hObject, eventdata, handles)

% --- Executes during object creation, after setting all properties.
function edit2_CreateFcn(hObject, eventdata, handles)
if ispc && isequal(get(hObject, 'BackgroundColor'),
get(0, 'defaultUiControlBackgroundColor'))
    set(hObject, 'BackgroundColor', 'white');
end

function edit3_Callback(hObject, eventdata, handles)

% --- Executes during object creation, after setting all properties.
function edit3_CreateFcn(hObject, eventdata, handles)
if ispc && isequal(get(hObject, 'BackgroundColor'),
get(0, 'defaultUiControlBackgroundColor'))
    set(hObject, 'BackgroundColor', 'white');
end

function edit4_Callback(hObject, eventdata, handles)

% --- Executes during object creation, after setting all properties.
function edit4_CreateFcn(hObject, eventdata, handles)
if ispc && isequal(get(hObject, 'BackgroundColor'),
get(0, 'defaultUiControlBackgroundColor'))
    set(hObject, 'BackgroundColor', 'white');
end

% --- Executes on button press in pushbutton10.
function pushbutton10_Callback(hObject, eventdata, handles)
handles = guidata(hObject);

l1 = get(handles.edit2, 'String');
l2 = get(handles.edit3, 'String');
l3 = get(handles.edit4, 'String');
guidata(hObject, handles);

axes(handles.axes4);
legend(l1,l2, l3, 'Location', 'northwest')
legend boxoff

function edit9_Callback(hObject, eventdata, handles)

% --- Executes during object creation, after setting all properties.
function edit9_CreateFcn(hObject, eventdata, handles)
if ispc && isequal(get(hObject, 'BackgroundColor'),
get(0, 'defaultUiControlBackgroundColor'))
    set(hObject, 'BackgroundColor', 'white');
end

```

```

% --- Executes on button press in pushbutton15.
function pushbutton15_Callback(hObject, eventdata, handles)
handles = guidata(hObject);
my1 = get(handles.edit9, 'String');
maxy1=str2double(my1);
guidata(hObject, handles);
axes(handles.axes4);
ylim([0 maxy1])

% _____ Additional Plot Stuff _____ %

% --- Executes on button press in pushbutton16.
function pushbutton16_Callback(hObject, eventdata, handles)

global filename1
global pathname
global currentfolder

[filename1, pathname] = uigetfile({'C:\George\Capsule
Experiments\BLE\Calibration\*.csv'})
currentfolder = fullfile(pathname, filename1);
if isequal(filename1,0) || isequal(pathname,0)
    return
end

fileID = fopen(fullfile(pathname, filename1));

temp = fscanf(fileID, '%d', [8 Inf]);
handles.fileData = temp';
guidata(hObject, handles);

% _____ Additional Plot Stuff _____ %

% _____ below this, actual time _____ %
%path=('C:\George\');
path=pathname;
file_path=strcat(path,filename1);
class(file_path);
Time = GetFileTime(file_path);
Time_1=struct2cell(Time);
finish=Time_1(3);
start=strsplit(filename1, "-");
start_date=str2double(start(5));
start_hour=str2double(start(6));
start_min=str2double(start(7));
global name1

table1 = readtable(filename1);
sensor1=table2array(table1(:,2));

end_date=start_date;
end_totalltime=table2array(table1(:,1));

```

```

timex=cell2mat(end_totvertime(length(end_totvertime),1));
end_time=strsplit(timex,":");
end_hour=str2double(end_time(1));
end_min=str2double(end_time(2));

cap_val_1=[];
for j=1:length(sensor1)
    volt_val_1(j,:) = 1/((4095/3.3)/(sensor1(j)))-0.05;
    %cap_val_1(j,:) = ((volt_val_1(j,:)-volt_val_1(1))/0.0031);
    cap_val_1(j,:) = ((volt_val_1(j,:)-2.5325)/0.0031);
    delta_cap_1(j,:) = abs(cap_val_1(j,:)-
cap_val_1(1,:))*100/abs(cap_val_1(1,:));
end

total_cap_val_1=cap_val_1;
total_delta_cap_val_1=delta_cap_1;

% _____ Setting up time _____ %

N= length(sensor1);
Total_time = (end_date - start_date) * 24 * 60 * 60 + (end_hour -
start_hour)* 60 * 60 + (end_min - start_min) * 60; % Calculate
total time in seconds
Time_step = Total_time/(N-1); % average step time in seconds between
two consecutive runs
Time_s = 0: Time_step: Total_time; % create an array called time
Time_m = Time_s/(60); % row array of time in hours
m=1;

[filepath,name1,ext] = fileparts(filename1);
set(handles.text6, 'String', name1);
set(gcf, 'PaperPositionMode', 'auto')
print([num2str(name1)], '-dtiffn', '-r0')

% _____ group plot stuff _____ %
filter = handles.filter;
axes(handles.axes4);
handles.h4=plot(handles.axes4,Time_m(m:length(total_delta_cap_val_1)
),smooth(total_delta_cap_val_1(1:length(total_delta_cap_val_1)),filt
er), 'k--
', 'MarkerSize', 5, 'MarkerIndices', 1:75:length(total_delta_cap_val_1))
;
hold on
xlabel('Time (min)', 'FontSize', 12, 'FontWeight', 'bold')
ylabel('\DeltaC (%)', 'FontSize', 12, 'FontWeight', 'bold')
%ylim([0 100])
%xlim([0 60])
set(gca, 'fontsize', 12, 'FontWeight', 'bold', 'box', 'off')
ax = gca;
% _____ END Additional Data _____ %

function edit10_Callback(hObject, eventdata, handles)

% --- Executes during object creation, after setting all properties.
function edit10_CreateFcn(hObject, eventdata, handles)

```

```

if ispc && isequal(get(hObject,'BackgroundColor'),
get(0,'defaultUiControlBackgroundColor'))
    set(hObject,'BackgroundColor','white');
end

% --- Executes on button press in pushbutton18.
function pushbutton18_Callback(hObject, eventdata, handles)
handles = guidata(hObject);

l1 = get(handles.edit2,'String');
l2 = get(handles.edit3,'String');
l3 = get(handles.edit4,'String');
l4 = get(handles.edit10,'String');
guidata(hObject, handles);

axes(handles.axes4);
legend(l1,l2, l3, l4,'Location','northwest')
legend boxoff

% --- Executes on button press in pushbutton19.
function pushbutton19_Callback(hObject, eventdata, handles)
handles = guidata(hObject);
guidata(hObject, handles);
h1 = get(handles.h1);
h2 = get(handles.h2);
h3 = get(handles.h3);
h4 = get(handles.h4);
refreshdata(h1);
refreshdata(h2);
refreshdata(h3);
refreshdata(h4);

```

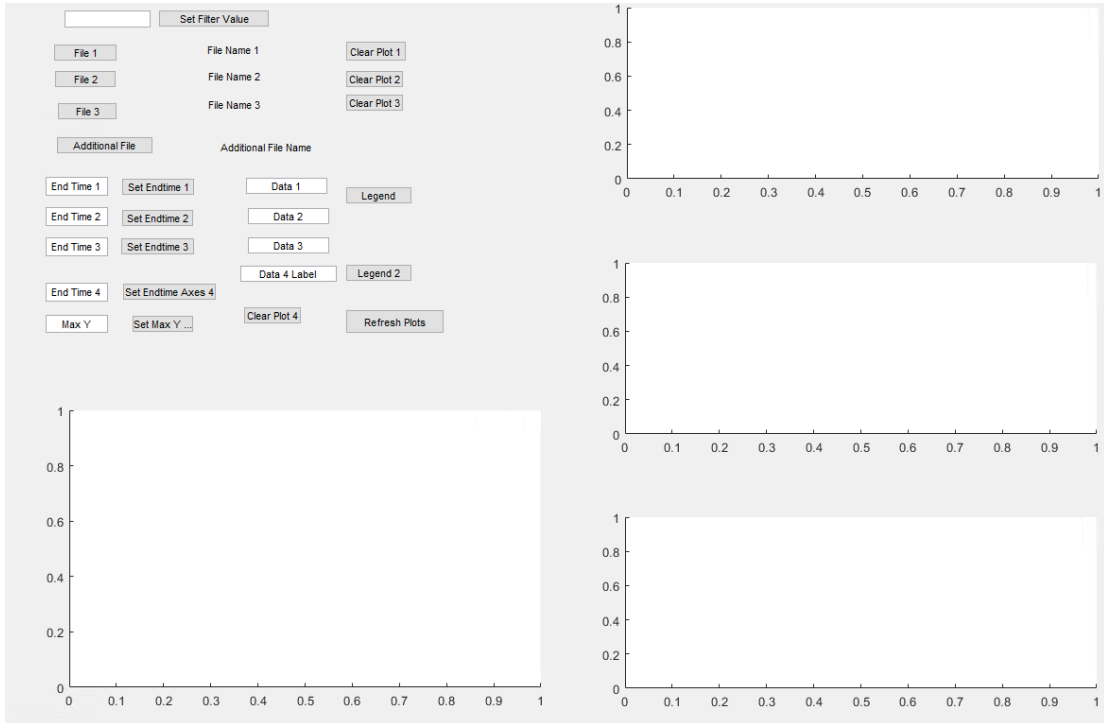


Figure 6-5 MATLAB GUI. Up to four data sequences can be plotted, three of which can be plotted individually on the right while all are overlaid in the plot on the bottom left. Features that can be modified directly in the GUI are smoothing filters, axes limits, and legend labels.

	Recorded Time	Sensor 1 Data	Sensor 2-4 Data (if used)		
	A	B	C	D	E
1	09:42:20-0400	3411	—	—	—.
2	09:42:21-0400	3408	—	—	—.
3	09:42:22-0400	3418	—	—	—.
4	09:42:23-0400	3416	—	—	—.
5	09:42:24-0400	3407	—	—	—.
6	09:42:25-0400	3408	—	—	—.
7	09:42:26-0400	3407	—	—	—.
8	09:42:27-0400	3408	—	—	—.

Figure 6-6 Depiction of data format in .csv file. This format is currently programmed into the app, while the algorithms to process the capacitance data are embedded in the MATLAB code above.

## 7. Bibliography

- [1] D. M. Goldberg and K. G. Wormsley, “The interrelationships of pancreatic enzymes in human duodenal aspirate,” *Gut*, vol. 11, no. 10, pp. 859–866, 1970.
- [2] R. C. Hartley, E. E. Gambill, G. W. Engstrom, and W. H. J. Summerskill, “Pancreatic exocrine function,” *Am. J. Dig. Dis.*, vol. 11, no. 1, pp. 27–39, 1966.
- [3] M. E. Haupt, M. J. Kwasny, M. S. Schechter, and S. A. McColley, “Pancreatic Enzyme Replacement Therapy Dosing and Nutritional Outcomes in Children with Cystic Fibrosis,” *J. Pediatr.*, vol. 164, no. 5, pp. 1110-1115.e1, 2014.
- [4] J. G. L. II and P. V Draganov, “Pancreatic function testing: Here to stay for the 21st century,” *World J. Gastroenterol.*, vol. 14, no. 20, pp. 3149–3158, 2008.
- [5] K. Strimbu and J. A. Tavel, “What are biomarkers?,” *Curr. Opin. HIV AIDS*, vol. 5, no. 6, pp. 463–6, Nov. 2010.
- [6] S.-L. Liang and D. W. Chan, “Enzymes and related proteins as cancer biomarkers: a proteomic approach,” *Clin. Chim. Acta.*, vol. 381, no. 1, pp. 93–7, May 2007.
- [7] S. J. Pandol, “The Exocrine Pancreas,” *Morgan Claypool Life Sci.*, 2010.
- [8] J. Wang *et al.*, “Circulating microRNAs in Pancreatic Juice as Candidate Biomarkers of Pancreatic Cancer,” *J. Cancer*, vol. 5, no. 8, pp. 696–705, 2014.
- [9] Z. Altintas, S. S. Kallempudi, and Y. Gurbuz, “Gold nanoparticle modified capacitive sensor platform for multiple marker detection,” *Talanta*, vol. 118, no. Supplement C, pp. 270–276, 2014.
- [10] D. Friedel, R. Modayil, and S. Stavropoulos, “Colon Capsule Endoscopy:

- Review and Perspectives,” *Gastroenterol. Res. Pract.*, vol. 2016, p. 9643162, 2016.
- [11] S. Yim, E. Gultepe, D. H. Gracias, and M. Sitti, “Biopsy using a Magnetic Capsule Endoscope Carrying, Releasing, and Retrieving Untethered Microgrippers,” *IEEE Trans. Biomed. Eng.*, vol. 61, no. 2, pp. 513–521, 2014.
- [12] J. Z. Ou, C. K. Yao, A. Rotbart, J. G. Muir, P. R. Gibson, and K. Kalantar-zadeh, “Human intestinal gas measurement systems: in vitro fermentation and gas capsules,” *Trends Biotechnol.*, vol. 33, no. 4, pp. 208–213, 2015.
- [13] J. Z. Ou *et al.*, “Potential of in vivo real-time gastric gas profiling: a pilot evaluation of heat-stress and modulating dietary cinnamon effect in an animal model,” *Sci. Rep.*, vol. 6, p. 33387, 2016.
- [14] S. E. Thompson and S. Parthasarathy, “Moore’s law: the future of Si microelectronics,” *Mater. Today*, vol. 9, no. 6, pp. 20–25, Jun. 2006.
- [15] C. Cordon, *System Theories: An Overview of Various System Theories and Its Application in Healthcare*, vol. 2. 2013.
- [16] “Effects of pH (Introduction to Enzymes).” [Online]. Available: <http://www.worthington-biochem.com/introbiochem/effectspH.html>. [Accessed: 16-Apr-2019].
- [17] N. (Neil) Hopkinson, R. J. M. Hague, and P. M. Dickens, *Rapid manufacturing : an industrial revolution for the digital age*. John Wiley, 2006.
- [18] M. Muskovich and C. J. Bettinger, “Biomaterials-Based Electronics: Polymers and Interfaces for Biology and Medicine,” *Adv. Healthc. Mater.*, vol. 1, no. 3, pp. 248–266, 2012.

- [19] C. J. Bettinger and Z. Bao, “Biomaterials-based organic electronic devices,” *Polym. Int.*, vol. 59, no. 5, p. n/a-n/a, May 2010.
- [20] G. Voskerician *et al.*, “Biocompatibility and biofouling of MEMS drug delivery devices,” *Biomaterials*, vol. 24, no. 11, pp. 1959–1967, Jul. 2003.
- [21] M. J. Madou, *From MEMS to Bio-MEMS and Bio-NEMS: Manufacturing Techniques and Applications*. CRC Press, 2011.
- [22] L. H. Nielsen *et al.*, “pH-triggered drug release from biodegradable microwells for oral drug delivery,” *Biomed. Microdevices*, vol. 17, no. 3, p. 55, 2015.
- [23] E. T. Cole *et al.*, “Enteric coated HPMC capsules designed to achieve intestinal targeting,” *Int. J. Pharm.*, vol. 231, no. 1, pp. 83–95, 2002.
- [24] A. Telefoncu, E. Dlnckaya, and K. D. Vorlop, “Preparation and characterization of pancreatic lipase immobilized in Eudragit-matrix,” *Appl. Biochem. Biotechnol.*, vol. 26, no. 3, pp. 311–317, Dec. 1990.
- [25] A. Touhami, “Biosensors and Nanobiosensors: Design and Applications,” 2014, pp. 374–403.
- [26] N. Bhalla, P. Jolly, N. Formisano, and P. Estrela, “Introduction to biosensors,” *Essays Biochem.*, vol. 60, no. 1, p. 1, 2016.
- [27] S. P. Mohanty and E. Kougiannos, “Biosensors: a tutorial review,” *IEEE Potentials*, vol. 25, no. 2, pp. 35–40, Mar. 2006.
- [28] D. R. Thévenot, K. Toth, R. A. Durst, and G. S. Wilson, “Electrochemical biosensors: recommended definitions and classification,” *Biosens. Bioelectron.*, vol. 16, no. 1–2, pp. 121–131, Jan. 2001.
- [29] S. Patel, R. Nanda, S. Sahoo, and E. Mohapatra, “Biosensors in Health Care:

- The Milestones Achieved in Their Development towards Lab-on-Chip-Analysis,” *Biochem. Res. Int.*, vol. 2016, pp. 1–12, Mar. 2016.
- [30] M. Chakraborty and M. Saleem J Hashmi, “An Overview of Biosensors and Devices,” in *Reference Module in Materials Science and Materials Engineering*, 2017.
- [31] D. Grieshaber, R. MacKenzie, J. Vörös, and E. Reimhult, “Electrochemical Biosensors - Sensor Principles and Architectures,” *Sensors (Basel)*, vol. 8, no. 3, p. 1400, 2008.
- [32] N. Elgrishi, K. J. Rountree, B. D. McCarthy, E. S. Rountree, T. T. Eisenhart, and J. L. Dempsey, “A Practical Beginner’s Guide to Cyclic Voltammetry,” *J. Chem. Educ.*, vol. 95, no. 2, pp. 197–206, Feb. 2018.
- [33] J. Wang, *Analytical electrochemistry*. Wiley-VCH, 2006.
- [34] R. van den Hurk and S. Evoy, “A Review of Membrane-Based Biosensors for Pathogen Detection,” *Sensors (Basel)*, vol. 15, no. 6, pp. 14045–78, Jun. 2015.
- [35] N. T. Thet, “Modified tethered bilayer lipid membranes for detection of pathogenic bacterial toxins and characterization of ion channels.” 2010.
- [36] K. Nakamura, T. Tanaka, and K. Takeo, “Characterization of protein binding to a nitrocellulose membrane,” *SEIBUTSU BUTSURI KAGAKU*, vol. 33, no. 6, pp. 293–303, Dec. 1989.
- [37] X. Luo and J. J. Davis, “Electrical biosensors and the label free detection of protein disease biomarkers,” *Chem. Soc. Rev.*, vol. 42, no. 13, p. 5944, Jun. 2013.

- [38] R. A. Dorledo de Faria, L. G. Dias Heneine, T. Matencio, and Y. Messaddeq, “Faradaic and non-faradaic electrochemical impedance spectroscopy as transduction techniques for sensing applications,” *Int. J. Biosens. Bioelectron.*, vol. 5, no. 1, Feb. 2019.
- [39] E. Katz and I. Willner, “Probing Biomolecular Interactions at Conductive and Semiconductive Surfaces by Impedance Spectroscopy: Routes to Impedimetric Immunosensors, DNA-Sensors, and Enzyme Biosensors,” *Electroanalysis*, vol. 15, no. 11, pp. 913–947, 2003.
- [40] S.-M. Park and J.-S. Yoo, “Peer Reviewed: Electrochemical Impedance Spectroscopy for Better Electrochemical Measurements,” *Anal. Chem.*, vol. 75, no. 21, pp. 455 A-461 A, Nov. 2003.
- [41] H. Ertuğrul and Z. O. Uygun, “Impedimetric Biosensors for Label-Free and Enzymless Detection,” 2012, p. 17.
- [42] F. Lisdat and D. Schäfer, “The use of electrochemical impedance spectroscopy for biosensing,” *Anal. Bioanal. Chem.*, vol. 391, no. 5, p. 1555, 2008.
- [43] “Cystic Fibrosis Foundation Annual Patient Registry Report,” 2013.
- [44] P. Díte *et al.*, “Differentiating autoimmune pancreatitis from pancreatic cancer,” *Minerva Gastroenterol. Dietol.*, vol. 60, no. 4, pp. 247–253, 2014.
- [45] X. Kong, T. Sun, F. Kong, Y. Du, and Z. Li, “Chronic Pancreatitis and Pancreatic Cancer,” *Gastrointest. Tumors*, vol. 1, no. 3, pp. 123–134, 2014.
- [46] R. Restrepo, H. E. Hagerott, S. Kulkarni, M. Yasrebi, and E. Y. Lee, “Acute Pancreatitis in Pediatric Patients: Demographics, Etiology, and Diagnostic Imaging,” *Am. J. Roentgenol.*, vol. 206, no. 3, pp. 632–644, 2016.

- [47] K. Hanada *et al.*, “Effective screening for early diagnosis of pancreatic cancer,” *Cancer Screen. Prev. Asia*, vol. 29, no. 6, pp. 929–939, 2015.
- [48] P. D. Kamin, M. E. Bernardino, S. Wallace, and B.-S. Jing, “Comparison of ultrasound and computed tomography in the detection of pancreatic malignancy,” *Cancer*, vol. 46, no. 11, pp. 2410–2412, Feb. 1980.
- [49] M. I. Canto *et al.*, “International Cancer of the Pancreas Screening (CAPS) Consortium summit on the management of patients with increased risk for familial pancreatic cancer,” *Gut*, vol. 62, no. 3, pp. 339–347, 2013.
- [50] T. Rustagi and P. A. Jamidar, “Endoscopic Retrograde Cholangiopancreatography–Related Adverse Events: General Overview,” *Minimizing, Recognizing, Manag. Endosc. Advers. Events*, vol. 25, no. 1, pp. 97–106, 2015.
- [51] M. Ozkan *et al.*, “Age-based computer-aided diagnosis approach for pancreatic cancer on endoscopic ultrasound images,” *Endosc. Ultrasound*, vol. 5, no. 2, pp. 101–107, 2016.
- [52] P. DK, B. HJ, J. Gyves, E. Allen, A. McLean, and P. DK, “EValuation of a serologic marker, ca19-9, in the diagnosis of pancreatic cancer,” *Ann. Intern. Med.*, vol. 110, no. 9, pp. 704–709, 1989.
- [53] A. Malesci *et al.*, “Determination of CA 19-9 antigen in serum and pancreatic juice for differential diagnosis of pancreatic adenocarcinoma from chronic pancreatitis,” *Gastroenterology*, vol. 92, no. 1, pp. 60–67, 1987.
- [54] M. Herreros-Villanueva and L. Bujanda, “Non-invasive biomarkers in pancreatic cancer diagnosis: what we need versus what we have,” *Ann. Transl.*

- Med.*, vol. 4, no. 7, p. 134, 2016.
- [55] H. Harada *et al.*, “Studies on Human Pure Pancreatic Juice Collected by Endoscopic Retrograde Catheterization of the Papilla,” *Gastroenterologia Jpn.*, vol. 13, no. 5, pp. 383–389, 1978.
- [56] M. Tian *et al.*, “Proteomic analysis identifies MMP-9, DJ-1 and A1BG as overexpressed proteins in pancreatic juice from pancreatic ductal adenocarcinoma patients,” *BMC Cancer*, vol. 8, p. 241, 2008.
- [57] K. Matsumoto *et al.*, “Role of the preoperative usefulness of the pathological diagnosis of pancreatic diseases,” *World J. Gastrointest. Oncol.*, vol. 8, no. 9, pp. 656–662, 2016.
- [58] S. Fleige and M. W. Pfaffl, “RNA integrity and the effect on the real-time qRT-PCR performance,” *Real-time Polym. Chain React.*, vol. 27, no. 2–3, pp. 126–139, 2006.
- [59] L. Raeymaekers, “Quantitative PCR: Theoretical Considerations with Practical Implications,” *Anal. Biochem.*, vol. 214, no. 2, pp. 582–585, 1993.
- [60] S. Dastgheib, C. Irajie, R. Assaei, F. Koohpeima, and P. Mokarram, “Optimization of RNA Extraction from Rat Pancreatic Tissue,” *Iran. J. Med. Sci.*, vol. 39, no. 3, pp. 282–288, 2014.
- [61] Z.-F. Quan, Z.-M. Wang, W.-Q. Li, and J.-S. Li, “Use of endoscopic naso-pancreatic drainage in the treatment of severe acute pancreatitis,” *World J. Gastroenterol.*, vol. 9, no. 4, pp. 868–870, 2003.
- [62] G.-Y. Liou and P. Storz, “Protein kinase D enzymes: novel kinase targets in pancreatic cancer,” *Expert Rev. Gastroenterol. Hepatol.*, vol. 9, no. 9, pp.

1143–1146, 2015.

- [63] I. J. Zeitlin and W. Sircus, “Factors influencing duodenal trypsin levels following a standard test meal as a test of pancreatic function,” *Gut*, vol. 15, no. 3, pp. 173–179, 1974.
- [64] M. E. Denyer and P. B. Cotton, “Pure pancreatic juice studies in normal subjects and patients with chronic pancreatitis,” *Gut*, vol. 20, no. 2, pp. 89–97, 1979.
- [65] R. Chen *et al.*, “Comparison of Pancreas Juice Proteins from Cancer Versus Pancreatitis Using Quantitative Proteomic Analysis,” *Pancreas*, vol. 34, no. 1, pp. 70–79, 2007.
- [66] J. V Olsen, S.-E. Ong, and M. Mann, “Trypsin Cleaves Exclusively C-terminal to Arginine and Lysine Residues,” *Mol. Cell. Proteomics*, vol. 3, no. 6, pp. 608–614, 2004.
- [67] J. Rodriguez, N. Gupta, R. D. Smith, and P. A. Pevzner, “Does Trypsin Cut Before Proline?,” *J. Proteome Res.*, vol. 7, no. 1, pp. 300–305, 2008.
- [68] H. U. Bermeyer, K. Gawehn, and M. Grassl, *Methods of Enzymatic Analysis*, 2nd ed., vol. 1. New York, NY: Academic Press, Inc., 1974.
- [69] W. B. Corporation, *Wothington Enzyme Manual*, 1st ed. Lakewood, NJ, 1993.
- [70] C. Duan, M. A. Alibakhshi, D.-K. Kim, C. M. Brown, C. S. Craik, and A. Majumdar, “Label-Free Electrical Detection of Enzymatic Reactions in Nanochannels,” *ACS Nano*, vol. 10, no. 8, pp. 7476–7484, 2016.
- [71] P. A. Neff, A. Serr, B. K. Wunderlich, and A. R. Bausch, “Label-Free Electrical Determination of Trypsin Activity by a Silicon-on-Insulator Based

- Thin Film Resistor,” *ChemPhysChem*, vol. 8, no. 14, pp. 2133–2137, 2007.
- [72] M. Stoytcheva, R. Zlatev, S. Cosnier, M. Arredondo, and B. Valdez, “High sensitive trypsin activity evaluation applying a nanostructured QCM-sensor,” *Biosens. Bioelectron.*, vol. 41, pp. 862–866, 2013.
- [73] L. Zhang, H. Qin, W. Cui, Y. Zhou, and J. Du, “Label-free, turn-on fluorescent sensor for trypsin activity assay and inhibitor screening,” *Talanta*, vol. 161, pp. 535–540, 2016.
- [74] E. J. Herrera-López, “Lipase and Phospholipase Biosensors: A Review,” in *Lipases and Phospholipases: Methods and Protocols*, G. Sandoval, Ed. Totowa, NJ: Humana Press, 2012, pp. 525–543.
- [75] M. Kanimozhi, M. Johny, N. Gayathri, and R. Subashkumar, “Optimization and Production of  $\alpha$ -Amylase from Halophilic Bacillus Species Isolated from Mangrove Soil Sources,” *J. Appl. Environ. Microbiol.*, vol. 2, no. 3, pp. 70–73, 2014.
- [76] M. J. Gibbs, A. Biela, and S. Krause, “ $\alpha$ -Amylase sensor based on the degradation of oligosaccharide hydrogel films monitored with a quartz crystal sensor,” *Spec. Issue Biosens. 2014*, vol. 67, pp. 540–545, 2015.
- [77] J. Fortin, “Transduction Principles,” in *Functional Thin Films and Nanostructures for Sensors: Synthesis, Physics and Applications*, A. Zribi and J. Fortin, Eds. Boston, MA: Springer US, 2009, pp. 17–29.
- [78] M. Stoytcheva, R. Zlatev, Z. Velkova, and G. Montero, “Nanoparticle modified QCM-based sensor for lipase activity determination,” *Anal. Methods*, vol. 5, no. 16, pp. 3811–3815, 2013.

- [79] N. F. Sheppard, M. J. Lesho, P. McNally, and A. Shaun Francomacaro, "Microfabricated conductimetric pH sensor," *Sensors Actuators B Chem.*, vol. 28, no. 2, pp. 95–102, 1995.
- [80] "Dielectric Behavior of Biomaterials at Different Frequencies on Room Temperature," *J. Phys. Conf. Ser.*, vol. 534, no. 1, p. 012063, 2014.
- [81] C. R. Mullins and C. A. Flood, "A STUDY OF GASTRIC PEPSIN IN VARIOUS DISEASES.," *J. Clin. Invest.*, vol. 14, no. 6, pp. 793–7, Nov. 1935.
- [82] J. Mayerle, A. Stier, M. M. Lerch, and C.-D. Heidecke, "Chronic Pancreatitis: Diagnostics and Therapy," *Surg.*, vol. 75, no. 7, pp. 731–748, Jul. 2004.
- [83] M. Kashiwagi *et al.*, "Group II and IV phospholipase A(2) are produced in human pancreatic cancer cells and influence prognosis.," *Gut*, vol. 45, no. 4, pp. 605–12, Oct. 1999.
- [84] R. Rabanal, D. Fondevila, A. Vargas, A. Ramis, J. Badiola, and L. Ferrer, "Immunocytochemical detection of amylase, carboxypeptidase A, carcinoembryonic antigen and  $\alpha$ 1-antitrypsin in carcinomas of the exocrine pancreas of the dog," *Res. Vet. Sci.*, vol. 52, no. 2, pp. 217–223, Mar. 1992.
- [85] I. L. Vovchuk and S. A. Petrov, "The role of carboxypeptidases in carcinogenesis," *Biochem. Suppl. Ser. B Biomed. Chem.*, vol. 2, no. 3, pp. 267–274, Sep. 2008.
- [86] J. Hermon-Taylor, J. Perrin, D. A. Grant, A. Appleyard, M. Bubel, and A. I. Magee, "Immunofluorescent localisation of enterokinase in human small intestine.," *Gut*, vol. 18, no. 4, pp. 259–65, Apr. 1977.
- [87] E. Lebenthal, I. Antonowicz, and H. Shwachman, "Enterokinase and Trypsin

- Activities in Pancreatic Insufficiency and Diseases of the Small Intestine,”  
*Gastroenterology*, vol. 70, no. 4, pp. 508–512, Apr. 1976.
- [88] T. Šuligoj, P. J. Ciclitira, and B. Božič, “Diagnostic and Research Aspects of Small Intestinal Disaccharidases in Coeliac Disease.,” *J. Immunol. Res.*, vol. 2017, p. 1042606, 2017.
- [89] “Lactose intolerance - Symptoms and causes - Mayo Clinic.” [Online]. Available: <https://www.mayoclinic.org/diseases-conditions/lactose-intolerance/symptoms-causes/syc-20374232>. [Accessed: 10-Apr-2019].
- [90] S. R. Owens and J. K. Greenson, “The pathology of malabsorption: current concepts,” *Histopathology*, vol. 50, no. 1, pp. 64–82, Jan. 2007.
- [91] R. Santini, J. Aviles, and T. W. Sheehy, “Sucrase activity in the intestinal mucosa of patients with sprue and normal subjects,” *Am. J. Dig. Dis.*, vol. 5, no. 12, pp. 1059–1062, Dec. 1960.
- [92] R. P. Verma and C. Hansch, “Matrix metalloproteinases (MMPs): Chemical–biological functions and (Q)SARs,” *Bioorg. Med. Chem.*, vol. 15, no. 6, pp. 2223–2268, Mar. 2007.
- [93] A. M. Knapinska, C.-A. Estrada, and G. B. Fields, “The Roles of Matrix Metalloproteinases in Pancreatic Cancer,” *Prog. Mol. Biol. Transl. Sci.*, vol. 148, pp. 339–354, Jan. 2017.
- [94] H. Huang, Huang, and Hao, “Matrix Metalloproteinase-9 (MMP-9) as a Cancer Biomarker and MMP-9 Biosensors: Recent Advances,” *Sensors*, vol. 18, no. 10, p. 3249, Sep. 2018.
- [95] A. Biela *et al.*, “Disposable MMP-9 sensor based on the degradation of peptide

- cross-linked hydrogel films using electrochemical impedance spectroscopy,” *Biosens. Bioelectron.*, vol. 68, pp. 660–667, Jun. 2015.
- [96] C. Chen and X. Yang, “The Diagnostic Effect of Capsule Endoscopy in 31 Cases with Subacute Small Bowel Obstruction,” *Gastrointest. Endosc.*, vol. 69, no. 5, p. AB216, Apr. 2009.
- [97] D. Friedel, R. Modayil, and S. Stavropoulos, “Colon Capsule Endoscopy: Review and Perspectives,” *Gastroenterol. Res. Pract.*, vol. 2016, p. 9643162, 2016.
- [98] K. Kalantar-Zadeh *et al.*, “A human pilot trial of ingestible electronic capsules capable of sensing different gases in the gut,” *Nat. Electron.*, vol. 1, no. 1, pp. 79–87, Jan. 2018.
- [99] A. Nemiroski, M. Ryou, C. C. Thompson, and R. M. Westervelt, “Swallowable fluorometric capsule for wireless triage of gastrointestinal bleeding,” *Lab Chip*, vol. 15, no. 23, pp. 4479–4487, 2015.
- [100] K. Kalantar-zadeh *et al.*, “Intestinal Gas Capsules: A Proof-of-Concept Demonstration,” *Gastroenterology*, vol. 150, no. 1, pp. 37–39, 2015.
- [101] N. OPTIZ and D. W. LÜBBERS, “Theory and Development of Fluorescence-Based Optochemical Oxygen Sensors: Oxygen Optodes.,” *Int. Anesthesiol. Clin.*, vol. 25, no. 3, 1987.
- [102] M. Mimeo *et al.*, “An ingestible bacterial-electronic system to monitor gastrointestinal health.,” *Science*, vol. 360, no. 6391, pp. 915–918, May 2018.
- [103] C. M. Caffrey, K. Twomey, and V. I. Ogurtsov, “Development of a wireless swallowable capsule with potentiostatic electrochemical sensor for

- gastrointestinal track investigation,” *Sensors Actuators B Chem.*, vol. 218, pp. 8–15, 2015.
- [104] M. S. Arefin, J. M. Redoute, and M. R. Yuce, “Integration of Low-Power ASIC and MEMS Sensors for Monitoring Gastrointestinal Tract Using a Wireless Capsule System,” *IEEE J. Biomed. Heal. Informatics*, vol. 22, no. 1, pp. 87–97, 2018.
- [105] C. Römmele, J. Brueckner, H. Messmann, and S. Gölder, “Clinical Experience with the PillCam Patency Capsule prior to Video Capsule Endoscopy: A Real-World Experience,” *Gastroenterol. Res. Pract.*, vol. 2016, pp. 1–6, Jan. 2016.
- [106] J. M. Park *et al.*, “Low-Power, High Data-Rate Digital Capsule Endoscopy Using Human Body Communication,” *Applied Sciences*, vol. 8, no. 9, 2018.
- [107] A. Kiourti, K. A. Psathas, and K. S. Nikita, “Implantable and ingestible medical devices with wireless telemetry functionalities: A review of current status and challenges,” *Bioelectromagnetics*, vol. 35, no. 1, pp. 1–15.
- [108] A. Kiourti and K. S. Nikita, “A Review of In-Body Biotelemetry Devices: Implantables, Ingestibles, and Injectables,” *IEEE Trans. Biomed. Eng.*, vol. 64, no. 7, pp. 1422–1430, 2017.
- [109] V. Sayeed, “Size, Shape, and Other Physical Attributes of Generic Tablets and Capsules Guidance for Industry,” 2015.
- [110] N.-K. Baek, I.-H. Sung, and D.-E. Kim, “Frictional resistance characteristics of a capsule inside the intestine for microendoscope design,” *Proc. Inst. Mech. Eng. Part H J. Eng. Med.*, vol. 218, no. 3, pp. 193–201, Mar. 2004.
- [111] “Engineering surfaces to enhance cell adhesion: Surface engineering,” *Mater.*

- Today*, vol. 6, no. 11, p. 19, Nov. 2003.
- [112] H. W. Lu, Q. H. Lu, W. T. Chen, H. J. Xu, and J. Yin, “Cell culturing on nanogrooved polystyrene petri dish induced by ultraviolet laser irradiation,” *Mater. Lett.*, vol. 58, no. 1–2, pp. 29–32, Jan. 2004.
- [113] E. Biazar, M. Heidari, A. Asefnejad, A. Asefnezhad, and N. Montazeri, “The relationship between cellular adhesion and surface roughness in polystyrene modified by microwave plasma radiation,” *Int. J. Nanomedicine*, vol. 6, pp. 631–9, 2011.
- [114] P. Ambe, S. A. Weber, M. Schauer, and W. T. Knoefel, “Swallowed foreign bodies in adults.,” *Dtsch. Arztebl. Int.*, vol. 109, no. 50, pp. 869–75, Dec. 2012.
- [115] CDRH, “Use of International Standard ISO 10993-1, ‘Biological evaluation of medical devices-Part 1: Evaluation and testing within a risk management process’; Guidance for Industry and Food and Drug Administration Staff Preface Public Comment,” 2016.
- [116] E. Trowers and M. E. Tischler, *Gastrointestinal physiology : a clinical approach*. .
- [117] P. R. Slawinski, D. Oleynikov, and B. S. Terry, “Intestinal biomechanics simulator for robotic capsule endoscope validation,” *J. Med. Eng. Technol.*, vol. 39, no. 1, pp. 54–59, Jan. 2015.
- [118] N. K. Ahluwalia, D. G. Thompson, J. Barlow, and L. Heggie, “Human small intestinal contractions and aboral traction forces during fasting and after feeding,” *Gut*, vol. 35, no. 5, pp. 625–30, May 1994.
- [119] C. Roman, Ed., *Gastrointestinal Motility*. Dordrecht: Springer Netherlands,

1983.

- [120] B. Laulicht, A. Tripathi, V. Schlageter, P. Kucera, and E. Mathiowitz, “Understanding gastric forces calculated from high-resolution pill tracking,” *Proc. Natl. Acad. Sci. U. S. A.*, vol. 107, no. 18, pp. 8201–6, May 2010.
- [121] M. S. Arefin, J.-M. Redoute, and M. R. Yuce, “Integration of Low-Power ASIC and MEMS Sensors for Monitoring Gastrointestinal Tract Using a Wireless Capsule System,” *IEEE J. Biomed. Heal. Informatics*, vol. 22, no. 1, pp. 87–97, Jan. 2016.
- [122] S. P. Woods and T. G. Constandinou, “Wireless Capsule Endoscope for Targeted Drug Delivery: Mechanics and Design Considerations,” *IEEE Trans. Biomed. Eng.*, vol. 60, no. 4, pp. 945–953, Apr. 2013.
- [123] A. D. Farmer, S. M. Scott, and A. R. Hobson, “Gastrointestinal motility revisited: The wireless motility capsule,” *United Eur. Gastroenterol. J.*, vol. 1, no. 6, pp. 413–21, Dec. 2013.
- [124] G. Bhattacharya, A. Mathur, S. Pal, J. McLaughlin, and S. Roy, “Equivalent Circuit Models and Analysis of Electrochemical Impedance Spectra of Caffeine Solutions and Beverages,” *Int. J. Electrochem. Sci.*, vol. 11, pp. 6370–6386, Jun. 2016.
- [125] M. Raimondo, M. Imoto, and E. P. Dimagno, “Rapid endoscopic secretin stimulation test and discrimination of chronic pancreatitis and pancreatic cancer from disease controls,” *Clin. Gastroenterol. Hepatol.*, vol. 1, no. 5, pp. 397–403, 2003.
- [126] O. James, “The Lundh test,” *Gut*, vol. 14, no. 7, pp. 582–591, 1973.

- [127] S. Pina, J. M. Oliveira, and R. L. Reis, “Natural-Based Nanocomposites for Bone Tissue Engineering and Regenerative Medicine: A Review,” *Adv. Mater.*, vol. 27, no. 7, pp. 1143–1169, Feb. 2015.
- [128] C.-H. Chuang *et al.*, “Detecting trypsin at liquid crystal/aqueous interface by using surface-immobilized bovine serum albumin,” *Biosens. Bioelectron.*, vol. 78, pp. 213–220, 2016.
- [129] C. Duan, M. A. Alibakhshi, D.-K. Kim, C. M. Brown, C. S. Craik, and A. Majumdar, “Label-Free Electrical Detection of Enzymatic Reactions in Nanochannels,” *ACS Nano*, vol. 10, no. 8, pp. 7476–7484, 2016.
- [130] M. Stoytcheva, R. Zlatev, S. Cosnier, M. Arredondo, and B. Valdez, “High sensitive trypsin activity evaluation applying a nanostructured QCM-sensor,” *Biosens. Bioelectron.*, vol. 41, no. 1, pp. 862–866, 2013.
- [131] L.-Q. Wu, W. E. Bentley, and G. F. Payne, “Biofabrication with biopolymers and enzymes: potential for constructing scaffolds from soft matter.,” *Int. J. Artif. Organs*, vol. 34, no. 2, pp. 215–24, Feb. 2011.
- [132] F. Teixeira Silva, B. Sorli, V. Calado, C. Guillaume, and N. Gontard, “Feasibility of a Gelatin Temperature Sensor Based on Electrical Capacitance.,” *Sensors (Basel)*, vol. 16, no. 12, Dec. 2016.
- [133] J. E. Eastoe, “The amino acid composition of mammalian collagen and gelatin,” *Biochem. J.*, vol. 61, no. 4, p. 589, 1955.
- [134] M. Li, “Thin films of stimuli-responsive hydrogels.,” *Polymers (Basel)*, 2015.
- [135] Y. Yeo, W. Geng, T. Ito, D. S. Kohane, J. A. Burdick, and M. Radisic, “Photocrosslinkable hydrogel for myocyte cell culture and injection,” *J.*

- Biomed. Mater. Res. Part B Appl. Biomater.*, vol. 81B, no. 2, pp. 312–322, 2007.
- [136] B. Schyrr, S. Boder-Pasche, R. Ischer, R. Smajda, and G. Voirin, “Fiber-optic protease sensor based on the degradation of thin gelatin films,” *Sens. Bio-Sensing Res.*, vol. 3, pp. 65–73, 2015.
- [137] A. Bigi, G. Cojazzi, S. Panzavolta, K. Rubini, and N. Roveri, “Mechanical and thermal properties of gelatin films at different degrees of glutaraldehyde crosslinking,” *Biomaterials*, vol. 22, no. 8, pp. 763–768, 2001.
- [138] A. A. Justiz Vaillant and A. Jan, *Physiology, Immune Response*. 2019.
- [139] J. Li and D. J. Mooney, “Designing hydrogels for controlled drug delivery,” *Nat. Rev. Mater.*, vol. 1, no. 12, p. 16071, Dec. 2016.
- [140] F. Zang, K. Gerasopoulos, X. Z. Fan, A. D. Brown, J. N. Culver, and R. Ghodssi, “Real-time monitoring of macromolecular biosensing probe self-assembly and on-chip ELISA using impedimetric microsensors,” *Biosens. Bioelectron.*, vol. 81, pp. 401–407, 2016.
- [141] Y. W. Kim *et al.*, “A surface acoustic wave biofilm sensor integrated with a treatment method based on the bioelectric effect,” *Sensors Actuators A Phys.*, vol. 238, pp. 140–149, 2016.
- [142] Y. W. Kim *et al.*, “An ALD aluminum oxide passivated Surface Acoustic Wave sensor for early biofilm detection,” *Sensors Actuators B Chem.*, vol. 163, no. 1, pp. 136–145, 2012.
- [143] S. Subramanian, “Integrated Threshold-Activated Feedback Microsystem for Real-Time Characterization, Sensing, and Treatment of Bacterial Biofilms.”

University of Maryland, College Park., 2016.

- [144] G. Banis, A. L. Beardslee, and R. Ghodssi, “Gelatin-Enabled Microsensor for Pancreatic Trypsin Sensing,” *Appl. Sci.*, vol. 8, no. 2, 2018.
- [145] N. Jaiswal, O. Prakash, M. Talat, S. H. Hasan, and R. K. Pandey, “ $\alpha$ -Amylase immobilization on gelatin: Optimization of process variables,” *J. Genet. Eng. Biotechnol.*, vol. 10, no. 1, pp. 161–167, 2012.
- [146] E. De Alteriis, P. Parascandola, S. Salvatore, and V. Scardi, “Enzyme immobilisation within insolubilised gelatin,” *J. Chem. Technol. Biotechnol. Biotechnol.*, vol. 35, no. 1, pp. 60–64, 1985.
- [147] N. W. Fadnavis, G. Sheelu, B. M. Kumar, M. U. Bhalerao, and A. A. Deshpande, “Gelatin Blends with Alginate: Gels for Lipase Immobilization and Purification,” *Biotechnol. Prog.*, vol. 19, no. 2, pp. 557–564, 2003.
- [148] N. Jaiswal and O. Prakash, “Immobilization of Soybean  $\alpha$ -amylase on Gelatin and its Application as a Detergent Additive.,” *Asian J. Biochem.*, vol. 6, pp. 337–346, 2011.
- [149] M. L. Caldwell, E. S. Dickey, V. M. Hanrahan, H. C. Kung, J. T. Kung, and M. Misko, “Amino Acid Composition of Crystalline Pancreatic Amylase from Swine<sup>1</sup>,” *J. Am. Chem. Soc.*, vol. 76, no. 1, pp. 143–147, 1954.
- [150] J. D. BIANCHETTA, J. BIDAUD, A. A. GUIDONI, J. J. BONICEL, and M. ROVERY, “Porcine Pancreatic Lipase,” *Eur. J. Biochem.*, vol. 97, no. 2, pp. 395–405, 1979.
- [151] K. V Thimann, “THE EFFECT OF SALTS ON THE IONISATION OF GELATIN,” *J. Gen. Physiol.*, vol. 14, no. 2, pp. 215–222, 1930.

- [152] E. Barsoukov and R. Macdonald, *Impedance Spectroscopy: Theory, Experiment, and Applications*, 2nd ed. Wiley, 2005.
- [153] J. S. Daniels and N. Pourmand, “Label-Free Impedance Biosensors: Opportunities and Challenges,” *Electroanalysis*, vol. 19, no. 12, pp. 1239–1257, 2007.
- [154] Y. Erwanto *et al.*, “Microbial Transglutaminase Modifies Gel Properties of Porcine Collagen,” *Asian-Australas J Anim Sci*, vol. 16, no. 2, pp. 269–276, 2003.
- [155] K. Franson and S. Rössner, “Fat intake and food choices during weight reduction with diet, behavioural modification and a lipase inhibitor,” *J. Intern. Med.*, vol. 247, no. 5, pp. 607–614, 2000.
- [156] V. König, L. Vertesy, and T. R. Schneider, “Structure of the alpha-amylase inhibitor tendamistat at 0.93 Å,” *Acta Crystallogr.*, vol. D, no. 59, pp. 1737–1743, 2003.
- [157] C. Berggren, B. Bjarnason, and G. Johansson, “Capacitive Biosensors,” *Electroanalysis*, vol. 13, no. 3, pp. 173–180, 2001.
- [158] T. L. Riss *et al.*, *Cell Viability Assays*. Eli Lilly & Company and the National Center for Advancing Translational Sciences, 2004.
- [159] J. R. Crowther, *The ELISA guidebook*. Humana Press, 2010.
- [160] H. B. Brooks *et al.*, *Basics of Enzymatic Assays for HTS*. Eli Lilly & Company and the National Center for Advancing Translational Sciences, 2004.
- [161] K. L. Cox, V. Devanarayan, A. Kriauciunas, J. Manetta, C. Montrose, and S. Sittampalam, *Immunoassay Methods*. Eli Lilly & Company and the National

Center for Advancing Translational Sciences, 2004.

- [162] E. K. Ulleberg, I. Comi, H. Holm, E. B. Herud, M. Jacobsen, and G. E. Vegarud, “Human Gastrointestinal Juices Intended for Use in In Vitro Digestion Models.”
- [163] T. Ghosh, D. I. Lewis, A. T. R. Axon, and S. M. Everett, “Review article: methods of measuring gastric acid secretion,” *Aliment. Pharmacol. Ther.*, vol. 33, no. 7, pp. 768–781, Apr. 2011.
- [164] W. H. Crosby, “Small intestinal studies: Methods for obtaining intraluminal contents and intestinal mucosa,” *Am. J. Dig. Dis.*, vol. 8, no. 1, pp. 2–11, Jan. 1963.
- [165] Y. Amoako-Tuffour, M. L. Jones, N. Shalabi, A. Labbe, S. Vengallatore, and S. Prakash, “Ingestible Gastrointestinal Sampling Devices: State-of-the-Art and Future Directions,” *Crit. Rev. Biomed. Eng.*, vol. 42, no. 1, pp. 1–15, 2014.
- [166] I. Skala and J. Simacek, “Device for obtaining samples of intestinal contents for microbiological and biochemical examinations,” *Gut*, vol. 9, pp. 246–248, 1968.
- [167] G. E. Banis, L. A. Beardslee, J. M. Stine, and R. Ghodssi, “Enteric & 3D-Printed Hybrid Package for Sampling in Digestive Regions,” in *A Solid-State Sensors, Actuators and Microsystems Workshop*, 2018, pp. 96–97.
- [168] J. L. Gonzalez-Guillaumin, D. C. Sadowski, K. V. I. S. Kaler, and M. P. Mintchev, “Ingestible Capsule for Impedance and pH Monitoring in the Esophagus,” *IEEE Trans. Biomed. Eng.*, vol. 54, no. 12, pp. 2231–2236, 2007.
- [169] P. Demosthenous and J. Georgiou, “An ingestible, NIR-fluorometric, cancer-

- screening capsule,” in *2015 37th Annual International Conference of the IEEE Engineering in Medicine and Biology Society (EMBC)*, 2015, pp. 2143–2146.
- [170] W. Yu, R. Rahimi, M. Ochoa, R. Pinal, and B. Ziaie, “A Smart Capsule With GI-Tract-Location-Specific Payload Release,” *IEEE Trans. Biomed. Eng.*, vol. 62, no. 9, pp. 2289–2295, 2015.
- [171] S. S. Mapara and V. B. Patravale, “Medical capsule robots: A renaissance for diagnostics, drug delivery and surgical treatment,” *J. Control. Release*, vol. 261, pp. 337–351, 2017.
- [172] C. M. Caffrey, O. Chevalerias, C. O’Mathuna, and K. Twomey, “Swallowable-Capsule Technology,” *IEEE Pervasive Comput.*, vol. 7, no. 1, pp. 23–29, 2008.
- [173] K. Kalantar-zadeh, N. Ha, J. Z. Ou, and K. J. Berean, “Ingestible Sensors,” *ACS Sensors*, vol. 2, no. 4, pp. 468–483, 2017.
- [174] S. N. Adler and Y. C. Metzger, “PillCam COLON capsule endoscopy: recent advances and new insights,” *Therap. Adv. Gastroenterol.*, vol. 4, no. 4, pp. 265–268, 2011.
- [175] M. Rasouli *et al.*, “Therapeutic Capsule Endoscopy: Opportunities and Challenges,” *J. Healthc. Eng.*, vol. 2, no. 4, 2011.
- [176] G. Pan and L. Wang, “Swallowable Wireless Capsule Endoscopy: Progress and Technical Challenges,” *Gastroenterol. Res. Pract.*, vol. 2012, pp. 1–9, 2012.
- [177] C. Van de Bruaene, D. De Looze, and P. Hindryckx, “Small bowel capsule endoscopy: Where are we after almost 15 years of use?,” *World J. Gastrointest. Endosc.*, vol. 7, no. 1, pp. 13–36, Jan. 2015.

- [178] J. Worsøe *et al.*, “Gastric transit and small intestinal transit time and motility assessed by a magnet tracking system,” *BMC Gastroenterol.*, vol. 11, no. 1, p. 145, Dec. 2011.
- [179] N. Mehmood and S. M. Aziz, “Magnetic sensing technology for in vivo tracking,” in *2012 International Conference on Emerging Technologies*, 2012, pp. 1–4.
- [180] I. Umay, B. Fidan, and B. Barshan, “Localization and Tracking of Implantable Biomedical Sensors,” *Sensors (Basel)*, vol. 17, no. 3, 2017.
- [181] E. A. Johannessen, L. Wang, S. W. J. Reid, D. R. S. Cumming, and J. M. Cooper, “Implementation of radiotelemetry in a lab-in-a-pill format,” *Lab Chip*, vol. 6, no. 1, pp. 39–45, Dec. 2006.
- [182] M. Yu, “M2A capsule endoscopy. A breakthrough diagnostic tool for small intestine imaging,” *Gastroenterol. Nurs.*, vol. 25, no. 1, pp. 24–7.
- [183] Y. Ye *et al.*, “Bounds on Rf Cooperative Localization for Video Capsule Endoscopy.” 2013.
- [184] V. V. Khutoryanskiy, “Longer and safer gastric residence,” *Nat. Mater.*, vol. 14, no. 10, pp. 963–964, Oct. 2015.
- [185] D. F. Evans, G. Pye, R. Bramley, A. G. Clark, T. J. Dyson, and J. D. Hardcastle, “Measurement of gastrointestinal pH profiles in normal ambulant human subjects,” *Gut*, vol. 29, no. 8, pp. 1035–41, Aug. 1988.
- [186] J. L. Seifter and H.-Y. Chang, “Extracellular Acid-Base Balance and Ion Transport Between Body Fluid Compartments,” *Physiology*, vol. 32, no. 5, pp. 367–379, Sep. 2017.

- [187] J. R. Taylor, C. A. Cooper, and T. P. Mommsen, "Implications of GI function for gas exchange, acid–base balance and nitrogen metabolism," *Fish Physiol.*, vol. 30, pp. 213–259, Jan. 2010.
- [188] S. G. NUGENT, D. KUMAR, D. S. RAMPTON, and D. F. EVANS, "Intestinal luminal pH in inflammatory bowel disease: possible determinants and implications for therapy with aminosalicylates and other drugs," *Gut*, vol. 48, no. 4, pp. 571–577, Apr. 2001.
- [189] D. Lalezari, "Gastrointestinal pH profile in subjects with irritable bowel syndrome," *Ann. Gastroenterol.*, vol. 25, no. 4, p. 333, 2012.
- [190] T. P. Bennett, *Modern topics in biochemistry : structure and function of biological molecules*. New York : The Macmillan Company ;, 1969.
- [191] L. R. Marek, "Elements of General and Biological Chemistry (Holum, John R.)," *J. Chem. Educ.*, vol. 60, no. 7, p. 613, Jul. 1983.
- [192] M. Puccetti, S. Giovagnoli, T. Zelante, L. Romani, and M. Ricci, "Development of novel indole-3-aldehyde loaded gastro-resistant spray-dried microparticles for post-biotic small intestine local delivery," *J. Pharm. Sci.*, 2018.
- [193] E. T. Cole *et al.*, "Enteric coated HPMC capsules designed to achieve intestinal targeting," *Int. J. Pharm.*, vol. 231, no. 1, pp. 83–95, 2002.
- [194] K. Whitehead, Z. Shen, and S. Mitragotri, "Oral delivery of macromolecules using intestinal patches: applications for insulin delivery," *J. Control. Release*, vol. 98, no. 1, pp. 37–45, 2004.
- [195] G. E. Banis, S. Member, L. A. Beardslee, J. M. Stine, R. M. Sathyam, and R.

- Ghodssi, “Gastrointestinal Targeted Sampling and Sensing via Embedded Packaging of Integrated Capsule System,” *J. Microelectromechanical Syst.*, vol. PP, pp. 1–7, 2019.
- [196] L. P. Degen and S. F. Phillips, “Variability of gastrointestinal transit in healthy women and men.,” *Gut*, vol. 39, no. 2, pp. 299–305, Aug. 1996.
- [197] L. R. Johnson, *Physiology of the gastrointestinal tract*. Academic Press, 2012.
- [198] M. Camilleri and C. M. Prather, “Axial Forces During Gastric Emptying in Health and Models of Disease,” 1994.
- [199] D. M. Mudie, G. L. Amidon, and G. E. Amidon, “Physiological Parameters for Oral Delivery and *in Vitro* Testing,” *Mol. Pharm.*, vol. 7, no. 5, pp. 1388–1405, Oct. 2010.
- [200] C. P. Gayer and M. D. Basson, “The effects of mechanical forces on intestinal physiology and pathology.,” *Cell. Signal.*, vol. 21, no. 8, pp. 1237–44, Aug. 2009.
- [201] B. Laulicht, A. Tripathi, V. Schlageter, P. Kucera, and E. Mathiowitz, “Understanding gastric forces calculated from high-resolution pill tracking.,” *Proc. Natl. Acad. Sci. U. S. A.*, vol. 107, no. 18, pp. 8201–6, May 2010.
- [202] K. J. Berean *et al.*, “Enhanced Gas Permeation through Graphene Nanocomposites,” *J. Phys. Chem. C*, vol. 119, no. 24, pp. 13700–13712, Jun. 2015.
- [203] M. E. Haupt, M. J. Kwasny, M. S. Schechter, and S. A. McColley, “Pancreatic Enzyme Replacement Therapy Dosing and Nutritional Outcomes in Children with Cystic Fibrosis,” *J. Pediatr.*, vol. 164, no. 5, pp. 1110-1115.e1, 2014.

- [204] R. Muench and R. Ammann, “Fecal Immunoreactive Lipase: A New Tubeless Pancreatic Function Test,” *Scand. J. Gastroenterol.*, vol. 27, no. 4, pp. 289–294, Jan. 1992.
- [205] P. T. Regan and E. P. DiMagno, “Exocrine pancreatic insufficiency in celiac sprue: A cause of treatment failure,” *Gastroenterology*, vol. 78, no. 3, pp. 484–487, Mar. 1980.
- [206] C. Basnayake and D. Ratnam, “Blood tests for acute pancreatitis.,” *Aust. Prescr.*, vol. 38, no. 4, pp. 128–30, Aug. 2015.
- [207] J. Walkowiak *et al.*, “[Comparison of faecal lipase test and faecal elastase-1 test in the assessment of exocrine pancreatic function in cystic fibrosis].,” *Med. Wieku Rozwoj.*, vol. 7, no. 2, pp. 149–55.
- [208] C. Forsmark and P. C. Adams, “Pancreatic function testing--valuable but underused.,” *Can. J. Gastroenterol.*, vol. 23, no. 8, pp. 529–30, Aug. 2009.
- [209] P. A. Hart *et al.*, “Endoscopic Pancreas Fluid Collection: Methods and Relevance for Clinical Care and Translational Science.,” *Am. J. Gastroenterol.*, vol. 111, no. 9, pp. 1258–66, 2016.
- [210] M. Vujasinovic, R. Valente, M. Del Chiaro, J. Permert, and J.-M. Löhr, “Pancreatic Exocrine Insufficiency in Pancreatic Cancer.,” *Nutrients*, vol. 9, no. 3, Feb. 2017.
- [211] J. E. Domínguez-Muñoz, L. Nieto-Garcia, J. López-Díaz, J. Lariño-Noia, I. Abdulkader, and J. Iglesias-Garcia, “Impact of the treatment of pancreatic exocrine insufficiency on survival of patients with unresectable pancreatic cancer: a retrospective analysis.,” *BMC Cancer*, vol. 18, no. 1, p. 534, May

2018.

- [212] “A Beginners Guide to Ion-Selective Electrodes. All you need to know about theory and practice of ISE measurements, with comprehensive Electrochemical Glossary.” [Online]. Available: <http://www.nico2000.net/Book/Guide1.html>. [Accessed: 22-Apr-2019].
- [213] Z. Xiao, R. Lopez, M. A. Parsi, M. Dodig, and T. Stevens, “Comparison of autoanalyzer and back titration for measurement of bicarbonate concentration in endoscopically collected pancreatic fluid.,” *Pancreas*, vol. 40, no. 2, pp. 237–41, Mar. 2011.
- [214] E. J. Herrera-López, “Lipase and Phospholipase Biosensors: A Review,” Humana Press, 2012, pp. 525–543.
- [215] K. Ge, D. H. Liu, K. Chen, L. H. Nie, and S. Z. Yao, “Assay of Pancreatic Lipase with the Surface Acoustic Wave Sensor System,” *Anal. Biochem.*, vol. 226, no. 2, pp. 207–211, Apr. 1995.
- [216] I. Ben Rejeb, F. Arduini, A. Amine, M. Gargouri, and G. Palleschi, “Amperometric biosensor based on Prussian Blue-modified screen-printed electrode for lipase activity and triacylglycerol determination,” *Anal. Chim. Acta*, vol. 594, no. 1, pp. 1–8, Jun. 2007.
- [217] M. S Bhutani, V. Gupta, S. Guha, D. Gheonea, and A. Saftoiu, *Pancreatic cyst fluid analysis—A review*, vol. 20. 2011.
- [218] P. Vijayvargiya, M. Camilleri, A. Shin, and A. Saenger, “Methods for diagnosis of bile acid malabsorption in clinical practice.,” *Clin. Gastroenterol. Hepatol.*, vol. 11, no. 10, pp. 1232–9, Oct. 2013.

- [219] C. Degirolamo, S. Modica, G. Palasciano, and A. Moschetta, “Bile acids and colon cancer: Solving the puzzle with nuclear receptors,” *Trends Mol. Med.*, vol. 17, no. 10, pp. 564–572, Oct. 2011.
- [220] K. Cheng and J.-P. Raufman, “Bile acid-induced proliferation of a human colon cancer cell line is mediated by transactivation of epidermal growth factor receptors,” *Biochem. Pharmacol.*, vol. 70, no. 7, pp. 1035–1047, Oct. 2005.
- [221] L. WEDLAKE, R. A’HERN, D. RUSSELL, K. THOMAS, J. R. F. WALTERS, and H. J. N. ANDREYEV, “Systematic review: the prevalence of idiopathic bile acid malabsorption as diagnosed by SeHCAT scanning in patients with diarrhoea-predominant irritable bowel syndrome,” *Aliment. Pharmacol. Ther.*, vol. 30, no. 7, pp. 707–717, Oct. 2009.
- [222] G. Lake-Bakaar, S. McKavanagh, C. E. Rubio, O. Epstein, and J. A. Summerfield, “Measurement of trypsin in duodenal juice by radioimmunoassay,” *Gut*, vol. 21, no. 5, pp. 402–7, May 1980.
- [223] American Chemical Society., *Reagent chemicals : American Chemical Society specifications, official from April 1, 1993*. The Society, 1993.
- [224] American Society of Biological Chemists., Rockefeller Institute for Medical Research., and American Society for Biochemistry and Molecular Biology., *The Journal of biological chemistry*. American Society for Biochemistry and Molecular Biology.
- [225] A. Robles Medina, L. Esteban Cerdán, A. Giménez Giménez, B. Camacho Páez, M. J. Ibáñez González, and E. Molina Grima, “Lipase-catalyzed esterification of glycerol and polyunsaturated fatty acids from fish and

- microalgae oils,” *J. Biotechnol.*, vol. 70, no. 1–3, pp. 379–391, Apr. 1999.
- [226] P. Speranza, A. P. B. Ribeiro, and G. A. Macedo, “Lipase catalyzed interesterification of Amazonian patauá oil and palm stearin for preparation of specific-structured oils,” *J. Food Sci. Technol.*, vol. 52, no. 12, pp. 8268–75, Dec. 2015.
- [227] Y. K. Lee *et al.*, “Kinetics and Chemistry of Hydrolysis of Ultrathin, Thermally Grown Layers of Silicon Oxide as Biofluid Barriers in Flexible Electronic Systems,” *ACS Appl. Mater. Interfaces*, vol. 9, no. 49, pp. 42633–42638, Dec. 2017.
- [228] D. Bonn, “Wetting transitions,” *Curr. Opin. Colloid Interface Sci.*, vol. 6, no. 1, pp. 22–27, Feb. 2001.
- [229] M.-C. Michalski and B. J. V. Saramago, “Static and Dynamic Wetting Behavior of Triglycerides on Solid Surfaces,” *J. Colloid Interface Sci.*, vol. 227, no. 2, pp. 380–389, Jul. 2000.
- [230] L. D. A. Chumpitaz, L. F. Coutinho, and A. J. A. Meirelles, “Surface tension of fatty acids and triglycerides,” *J. Am. Oil Chem. Soc.*, vol. 76, no. 3, pp. 379–382, Mar. 1999.
- [231] W. Xie *et al.*, “Design and Validation of a Biosensor Implantation Capsule Robot,” *J. Biomech. Eng.*, vol. 139, no. 8, p. 081003, Jun. 2017.
- [232] J. Carrère, C. Galabert, J. P. Thouvenot, and C. Figarella, “Assay of human pancreatic lipase in biological fluids using a non-competitive enzyme immunoassay,” *Clin. Chim. Acta.*, vol. 161, no. 2, pp. 209–19, Dec. 1986.
- [233] K. E. Barrett and W. F. Ganong, *Ganong’s review of medical physiology. LK -*

<https://umaryland.on.worldcat.org/oclc/779244271>, 24th ed. /. New York: McGraw-Hill Medical ;, 2012.

- [234] M. Camilleri *et al.*, “Human gastric emptying and colonic filling of solids characterized by a new method,” *Am. J. Physiol. - Gastrointest. Liver Physiol.*, vol. 257, no. 2, 1989.
- [235] Z. Huang *et al.*, “Effects of triglycerides levels in human whole blood on the extraction of 19 commonly used drugs using liquid-liquid extraction and gas chromatography-mass spectrometry.,” *Toxicol. reports*, vol. 2, pp. 785–791, 2015.
- [236] Y. K. Lee *et al.*, “Kinetics and Chemistry of Hydrolysis of Ultrathin, Thermally Grown Layers of Silicon Oxide as Biofluid Barriers in Flexible Electronic Systems,” *ACS Appl. Mater. Interfaces*, vol. 9, no. 49, pp. 42633–42638, Dec. 2017.
- [237] A. Ziegler, L. Gonzalez, and A. Blikslager, “Large Animal Models: The Key to Translational Discovery in Digestive Disease Research,” *CMGH*, vol. 2, no. 6. Elsevier Inc, pp. 716–724, 01-Nov-2016.
- [238] J. Flemming and S. Cameron, “Small bowel capsule endoscopy: Indications, results, and clinical benefit in a University environment,” *Medicine (Baltimore)*, vol. 97, no. 14, pp. e0148–e0148, Apr. 2018.
- [239] P. R. Slawinski, D. Oleynikov, and B. S. Terry, “Intestinal biomechanics simulator for robotic capsule endoscope validation,” *J. Med. Eng. Technol.*, vol. 39, no. 1, pp. 54–59, Jan. 2015.
- [240] R. Miftahof and N. Akhmadeev, “Dynamics of intestinal propulsion,” *J. Theor.*

- Biol.*, vol. 246, no. 2, pp. 377–393, May 2007.
- [241] W. L. Hasler, “The use of SmartPill for gastric monitoring,” *Expert Rev. Gastroenterol. Hepatol.*, vol. 8, no. 6, pp. 587–600, Aug. 2014.
- [242] H. Y. Shi, S. C. Ng, K. K. Tsoi, J. C. Wu, J. J. Sung, and F. K. Chan, “The role of capsule endoscopy in assessing mucosal inflammation in ulcerative colitis,” *Expert Rev. Gastroenterol. Hepatol.*, vol. 9, no. 1, pp. 47–54, Jan. 2015.
- [243] S. H. Itzkowitz, D. H. Present, and Crohn’s and Colitis Foundation of America Colon Cancer in IBD Study Group, “Consensus conference: Colorectal cancer screening and surveillance in inflammatory bowel disease.,” *Inflamm. Bowel Dis.*, vol. 11, no. 3, pp. 314–21, Mar. 2005.
- [244] J. K. Limdi and F. A. Farraye, “An Update on Surveillance in Ulcerative Colitis.”
- [245] Y. L. Kong *et al.*, “3D-Printed Gastric Resident Electronics,” *Adv. Mater. Technol.*, vol. 4, no. 3, p. 1800490, Dec. 2018.
- [246] P. G. Toner, K. E. Carr, A. Ferguson, and C. Mackay, “Scanning and transmission electron microscopic studies of human intestinal mucosa.,” *Gut*, vol. 11, no. 6, pp. 471–81, Jun. 1970.
- [247] T. Skrzypek *et al.*, “Light and scanning electron microscopy evaluation of the postnatal small intestinal mucosa development in pigs.,” *J. Physiol. Pharmacol.*, vol. 56 Suppl 3, pp. 71–87, Jun. 2005.
- [248] A. Menciassi and P. Dario, “Bio-inspired solutions for locomotion in the gastrointestinal tract: background and perspectives,” *Philos. Trans. R. Soc. London. Ser. A Math. Phys. Eng. Sci.*, vol. 361, no. 1811, pp. 2287–2298, Oct.

2003.

- [249] W. Xie *et al.*, “Design and Validation of a Biosensor Implantation Capsule Robot,” *J. Biomech. Eng.*, vol. 139, pp. 081003–1, 2017.
- [250] M. D. Breton *et al.*, “Continuous Glucose Monitoring and Insulin Informed Advisory System with Automated Titration and Dosing of Insulin Reduces Glucose Variability in Type 1 Diabetes Mellitus,” *Diabetes Technol. Ther.*, vol. 20, no. 8, pp. 531–540, Aug. 2018.
- [251] C. Steiger, A. Abramson, P. Nadeau, A. P. Chandrakasan, R. Langer, and G. Traverso, “Ingestible electronics for diagnostics and therapy,” *Nat. Rev. Mater.*, vol. 4, no. 2, pp. 83–98, Feb. 2019.
- [252] I. Bilican, M. T. Guler, N. Gulener, M. Yuksel, and S. Agan, “Capacitive solvent sensing with interdigitated microelectrodes,” *Microsyst. Technol.*, vol. 22, no. 3, pp. 659–668, 2016.